WARSAW UNIVERSITY OF TECHNOLOGY

Faculty of Physics

Ph.D. THESIS

Daniel Kikoła, M.Sc. Eng.

Hidden charm production in the relativistic heavy ion collisions registered in the STAR experiment

Supervisors

Professor Jan Pluta, Ph.D., D.Sc.

Grażyna Odyniec, Ph.D.

Warsaw 2010

Streszczenie

Produkcja cząstek o ukrytym powabie w zderzeniach relatywistycznych ciężkich jonów rejestrowanych w eksperymencie STAR

Analiza produkcji mezonów J/ψ jest jednym z najważniejszych narzędzi do badania właściwości materii jądrowej w warunkach olbrzymich temperatur i gęstości energii, które powstają w zderzeniach relatywistycznych ciężkich jonów. Początkowo zainteresowanie produkcją mezonów J/ψ (cząstek o ukrytym powabie) wiązało się z przewidywaniami, że tłumienie produkcji tych cząstek będzie sygnałem utworzenia nowego stanu materii - plazmy kwarkowo-gluonowej (Quark-Gluon Plasma, QGP). Tłumienie miało być skutkiem ekranowania w plazmie oddziaływania silnego między kwarkami budującymi mezon J/ψ. Tłumienie jest związane z energią wiązania kwark-antykwark powabny oraz gęstością energii w QGP, a sam proces jest analogią ekranowania Debye'a w klasycznej fizyce plazmy. Gęstość energii jest bezpośrednio związana z temperaturą QGP, dlatego też pomiary produkcji mezonów J/ψ mogą dostarczyć informacji na temat termodynamicznych właściwości materii jądrowej w ekstremalnych warunkach. Modyfikacja produkcji mezonów J/ψ może być również spowodowana innymi efektami. Mogą to być procesy nie związane z powstaniem QGP, jak np. modyfikacja rozkładów partonów w zderzanych jądrach atomowych (tzw. przesłanianie, ang. shadowing) lub absorpcja przez materię jądrową oraz w wyniku nieelastycznego rozpraszania na hadronach wyprodukowanych w reakcji. Mezony J/ψ mogę też zostać utworzone w wyniku statystycznej rekombinację kwarków powabnych obecnych w QGP.

Produkcja cząstek o ukrytym powabie jest bardzo skomplikowanym procesem i niezbędne są jej systematyczne pomiary dla różnych zderzanych systemów (p+p, d+Au oraz A+A). Choć oddziaływanie mezonów J/ψ z materią jądrową było intensywnie badane na przestrzeni ostat-

nich 20 lat, to nie udało się uzyskać spójnego opisu interakcji tych cząstek z silnie oddziałującą materią wytworzoną w zderzeniach relatywistycznych ciężkich jonów.

Wobec braku ugruntowanej teorii oraz licznych przykładów modeli opisujących wyniki doświadczalne, wychodząc z diametralnie różnych założeń fizycznych, tylko nowe dane eksperymentalne mogą pomóc w zrozumieniu oddziaływań mezonów J/ψ z materią jądrową. Wyniki zamieszczone w tej pracy są częścią takiego programu badawczego, realizowanego przez eksperyment STAR przy zderzaczu RHIC.

W niniejszej pracy przedstawiamy wyniki badań nad produkcją mezonów J/ψ w reakcjach Cu+Cu oraz Au+Au przy energii 200 GeV na nukleon w układzie środka masy. Po raz pierwszy w eksperymencie STAR został zmierzony czynnik modyfikacji jądrowej R_{AA} dla cząstek J/ψ w reakcjach Au+Au. Również po raz pierwszy zostały wykonane pomiary tego czynnika dla J/ψ z małym pędem poprzecznym w reakcjach Cu+Cu. Została zmierzona produkcja mezonów J/ψ oraz czynnik R_{AA} w funkcji pędu poprzecznego, jak również centralności reakcji. Wyniki wskazują, że produkcja J/ψ w reakcjach Au+Au, zarówno w centralnych (0-20% przekroju czynnego) jak i pół-peryferycznych (20-80%), jest silnie tłumiona w porównaniu do zderzeń proton+proton. Takie wyniki sugerują, że została wytworzona materia jądrowa o bardzo dużej gęstości, potencjalnie powyżej progu na utworzenie plazmy kwarkowo-gluonowej. Co więcej, dane doświadczalne są dobrze opisywane przez modele teoretyczne zakładające powstanie QGP. Analizowany był również przepływ eliptyczny mezonów J/ψ, który może dostarczyć dodatkowych informacji na temat mechanizmu produkcji tych cząstek w QGP oraz tego, czy układ znajduje się w stanie równowagi termodynamicznej. Sprawdziliśmy także możliwość zastosowania wyzwalacza dedykowanego analizie produkcji J/ψ, który mógłby zwiększyć ilość dostępnych danych, a tym samym poprawić precyzję pomiarów. Obecny układ eksperymentalny nie pozwala na zastosowanie efektywnego wyzwalacza dla mezonów J/ψ dla reakcji Au+Au. Niemniej jednak dane zebrane w 2010 r. umożliwią analizę produkcji oraz przepływu eliptycznego z dokładności pozwalającą na weryfikację hipotezy zakładającej produkcji J/ψ w wyniku statystycznej rekombinację kwarków powabnych.

Abstract

Charmonium production is considered to be one of the key observables in studies of the properties of the hot and dense nuclear matter created in relativistic heavy ion collisions. Originally, the J/ψ suppression effect was proposed as a possible signal of the formation of Quark-Gluon Plasma (QGP). This suppression was expected to result from the color screening of the binding potential in QGP, a process similar to the Debye screening in a classic electromagnetic plasma. The magnitude of the suppression depends on the charmonium binding potential and the energy density in the medium, which can be related to the temperature. Therefore, the studies of J/ψ production, especially J/ψ with low transverse momentum, may allow us to examine the thermodynamical properties of the medium. However, other effects, like a gluon shadowing, an absorption by nuclear matter or hadronic co-movers, or even J/ψ production via statistical coalescence of charm and anti-charm quarks in QGP, may modify the J/ψ production rates.

In view of such complicated processes, systematic studies of J/ψ production in various systems ($p + p$, d+Au and A+A collisions) are needed. Indeed, the J/ψ in-medium interactions have been intensely studied over last years, although a coherent description of J/ψ interactions with the hot and dense strongly interacting matter did not emerge. In light of ambiguous model predictions and a lack of solid theory calculations, the experimental input is required to understand these interactions. The results contained in this thesis (for Cu+Cu and Au+Au collisions) are part of the experimental effort being carried out by the STAR experiment at RHIC.

In this work, we report the first measurements of the J/ψ nuclear modification factor in Au+Au collisions at STAR, as well as the first study of low-p_T J/ψ in Cu+Cu collisions at STAR. The J/ψ meson invariant yields, both integrated and p_T spectra, were measured in Au+Au and Cu+Cu collisions at $\sqrt{s_{NN}} = 200$ GeV. The nuclear modification factor R_{AA} as a function of transverse momentum and event centrality has been extracted. The R_{AA} shows that J/ψ production, both in central (0–20%) and semi-peripheral (20–80%) Au+Au collision, scaled by the corresponding number of binary collisions, is strongly suppressed compared to

$p + p$. This suggest that a very high energy density is created in these collisions. Moreover, models which assume that the energy density is above the threshold for the QGP formation, describe the data well.

Furthermore, we attempted to measure the J/ψ elliptic flow in Au+Au collisions, which can demonstrate a degree of thermalization of the created system, and shed light on the J/ψ production mechanism. Finally, we examined the experimental prospects for low-p_T J/ψ measurements via the di-electron channel in Au+Au collisions at STAR. A sufficiently effective low-p_T J/ψ trigger could not be implemented with the currently available detector setup, and therefore the analysis can be only carried out with minimum-bias data. With the number of minimum-bias Au+Au events collected in 2010, J/ψ production and elliptic flow are expected to be measured with a statistical precision better than 5%. This will allow us to test the hypothesis of J/ψ production in QGP via the statistical coalescence of c and $\bar{c}$ quarks.

Acknowledgements

A great many people have contributed to make this work possible.

First, I would like to thank my lovely wife Agata for the years of love, support, and understanding. I would have never finished this dissertation without you. I thank my parents, Krystyna and Zbigniew Kikoła, and in-laws, Krystyna and Andrzej Bedarczyk, for their constant support.

I would like to thank Grażna Odyniec, my supervisor at the Lawrence Berkeley National Laboratory, for all of her amazing support over the years, especially at the beginning of my stay at Berkley. I am grateful for sharing her knowledge and her valuable guidance in the course of my project, and for helping me to refine my dissertation. I am also grateful to the head of the Relativistic Nuclear Collisions group, Hans-Georg Ritter, for all his support during my stay at LBNL.

I'd like to thank my advisor, Jan Pluta, for his guidance and support throughout my graduate studies. Thanks to all the members of the Heavy Ion Reaction Group at Warsaw University of Technology, especially Wiktor Peryt and Tomasz Pawlak, for their support and effort in providing me with many scientific opportunities, and Barbara Trzeciak for her help with many tasks in Warsaw when I was abroad.

I am grateful to all members of the Relativistic Nuclear Collisions group at LBNL, with whom I have had the pleasure to work. Special thanks to Nu Xu, Hans-Georg Ritter, Xin Dong, Andrew Rose, Art Poskanzer, Mateusz Ploskon, Christopher Powell, Vi Nham Tram, Sevil Salur, Hiroshi Masui, Shusu Shi, Yifei Zhang and Ernst Sichtermann for their help and inspiring discussions.

Special thanks to my fellow graduate students and postdocs at LBNL, especially my office mates Michał, Vi Nham, Gabriel and Bo, for providing a great atmosphere in work and also fun outside of work. Also I'd like to thank Leo Greiner for his tremendous help at the beginning of my stay at Berkley.

Thanks to all members of the STAR collaboration who provided so much support and feedback over the years. Throughout my analysis, the STAR Heavy Flavor Working Group has provided excellent feedback, as well as constructive criticism. I'd like to thank all the people I was working with for strengthening this analysis.

Finally, thanks to Grazyna and Chris for editing this dissertation. They have offered numerous improvements while saving me from countless embarrassing errors.

Contents

List of Figures

List of Tables

Chapter 1

Introduction

Relativistic heavy ion physics addresses possibly the most compelling and challenging area of our field, namely the nature of the strong force which is responsible for interactions between the fundamental constituents of matter, quarks and gluons.

If heavy ions collide with a sufficiently high energy, and a high enough energy density is attained in the interaction volume, then quarks and gluons are expected to be liberated from hadrons and form a new state of matter called Quark-Gluon Plasma (QGP). Quarks and gluons in QGP can freely propagate over the nuclear volume, and this provides a unique opportunity to study the interaction between the nuclear constituents and to explore new phenomena. The general aim of the work contained in this thesis was to understand the dynamics of the Quark-Gluon Plasma phase.

This chapter will proceed to briefly review what is known about the constituents of nuclear matter, the theory of the strong interaction, quantum chromodynamics, and will describe the properties of the hypothetical Quark-Gluon Plasma. The outline of the work reported here is shown at the and of the chapter.

1.1 Standard model and quantum chromodynamics

1.1.1 Standard model

The Standard Model [1, 2] is the only model that successfully describes the fundamental particles and their interactions, including the strong interactions, which is due to the color charges of quarks and gluons, and a combined theory of weak and electromagnetic interaction, known as electroweak theory. Electroweak theory introduces W and Z bosons as the carrier particles of

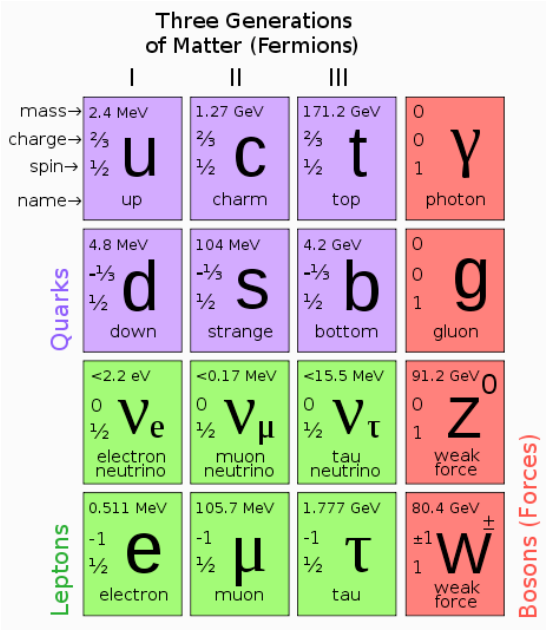

Figure 1.1: Elementary particle in the Standard Model and their properties.

weak processes, and photons of electromagnetic interactions. In case of the strong interactions, gluons are the gauge bosons for the color force.

The elementary particles in the Standard Model are shown in Fig. 1.1. The Standard Model does not include gravitational interactions.

1.1.2 Quantum chromodynamics

Quantum chromodynamics (QCD) [1, 2] is a theory of the strong force. It describes a fundamental interactions between the quarks and gluons, constituents of hadrons. QCD is a non-abelian gauge quantum field theory, an extension of quantum electrodynamics (QED), which describes the interaction of electric charges with the electromagnetic field represented by photons. In QCD, the massive quarks (carrying specific charge called color) interact exchanging massless gluons. In contrast to photons, gluons carry color charges and therefore can interact with each other.

The quark-antiquark potential is describe by the formula [2]:

$$V_{strong} = -\frac{4}{3}\frac{\alpha_s}{r} + kr \tag{1.1}$$

where: r is the distance between quarks, α_s is the coupling constant and $k \sim 1$ GeV/fm. There are two remarkable features of the strong interaction revealed by Eq. 1.1: **confinement**

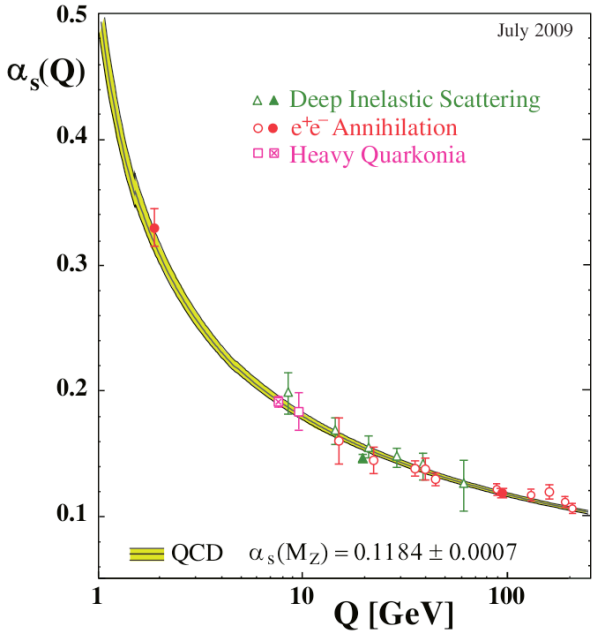

Figure 1.2: Summary of measurements of α_s as a function of the energy scale Q. The curves are QCD predictions for the combined world average value of $\alpha_s(M_Z)$, where M_Z is mass of the Z^0 boson. Figure taken from [3].

and **asymptotic freedom**.

At large distances the linear term kr begins to dominate and the potential V_{strong} becomes proportional to the distance. With increasing r, the energy of the color-force field between quarks also increases. In order to separate a pair of quarks, $q\overline{q}$, the additional energy has to be applied. At some point, it is energetically favorable to create an additional pair quark-antiquark. Then, the original pair of quarks becomes two $q\overline{q}$ pairs. Therefore free quarks are never seen in nature – they are always confined inside hadrons.

On the other hand, the interaction for small r is dominated by Coulomb-like term $-\frac{4}{3}\frac{\alpha_s}{r}$. The coupling constant, α_s, depends on the four momentum Q transferred in the interaction, and is shown in Fig. 1.2. The value of α_s decreases with increasing momentum transfer, and the interaction becomes arbitrarily weak for large Q^2(for large Q^2, $\alpha_s(Q) \rightarrow 0$). At a results, at large energies or at small distances, quarks behave like free particles. In addition, if $\alpha_s(Q)$ is small then perturbative methods can be used to calculate physical observables such as cross-sections. Perturbative QCD (pQCD) [4, 5] successfully describes hard processes (proceeding with high Q), such as jet production in high energy proton-antiproton collisions [4, 5, 6, 7]. The applicability of pQCD is defined by the QCD scale parameter Λ_{QCD} ($\Lambda_{QCD} \cong 200$ MeV) – if

$Q >> \Lambda_{QCD}$ then the process is in a perturbative domain and can be described by pQCD [5].

On the other hand, the description of soft processes (proceeding with small momentum transfer), such as hadronisation, remains a problem in QCD. Perturbative theory breaks down at $Q \simeq 1\ GeV$ (scale comparable with masses of light hadrons) and other methods, like Lattice QCD, have to be used to describe soft processes.

Lattice QCD (LQCD) [5] is a well establish non-perturbative implementation of field theory in which the QCD quantities are numerically calculated on a discrete space-time grid. Lattice QCD allows us to obtain the properties of matter in equilibrium, but there are some limitations. First of all, LQCD calculations require fine lattice spacing to obtain precise results (LQCD approximation approaches continuum QCD as the lattice spacing approaches zero) and therefore large computational resources are needed. With the growth of computing power, this problem will become less important. Secondly, lattice simulations are possible only for baryon density $\mu_B = 0$. At finite μ_B, LQCD breaks down because of the sign problem [8]. A few techniques were proposed to overcome this difficulty, although there is no satisfactory solution yet [8, 9, 10, 11].

1.1.3 Quark-gluon plasma and phase-space diagram

Asymptotic freedom implies that if sufficiently high energies are provided, then one can create a new state of matter in which quarks and gluons are no longer confined in hadrons and can propagate freely in the volume of the created system. Such a medium is called a Quark-Gluon Plasma (QGP) [12, 13] and it was present at the very first moments in the Universe after the Big Bang [13, 14].

Theoretical model calculations ([8, 15] and references there) predict a phase space diagram of strongly interacting matter which is schematically shown in Fig. 1.4. At moderate temperature and density, quarks are confined in hadrons and such a phase is called hadronic matter. At very high temperatures, hadrons "melt" and their constituents form a quark-gluon plasma. QGP can be created in a laboratory by colliding heavy ions with ultra-relativistic energies. It is also expected that QGP can exist at low temperature but in a highly compressed nuclear matter (at high baryon potential), and therefore QGP may exist inside neutron stars - in this case, baryons dissolve into quarks and gluons due to the enormous pressure. It is also anticipated that at extremely high densities and low temperatures, quarks and gluons become correlated in Cooper pairs and form yet another phase - a color superconductor [13].

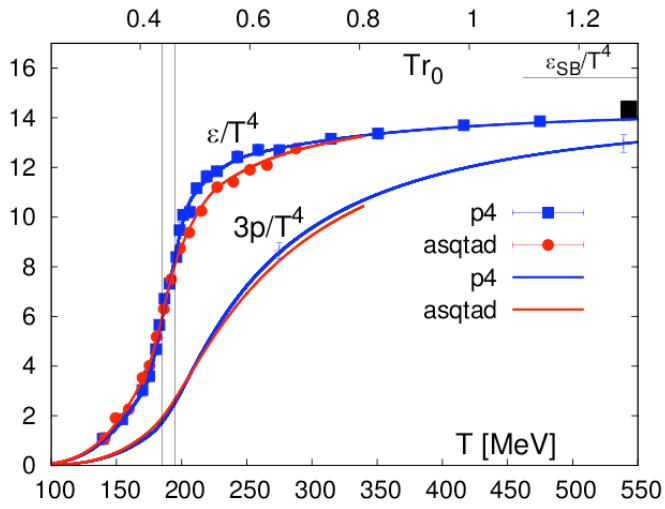

Figure 1.3: Energy density and pressure calculated in 2+1 flavor lattice QCD. Blue and red lines correspond to different methods used in the calculations (different fermion actions). The band indicates the transition region $185 < T < 195$ MeV. Results were obtained for physical strange quark mass and almost physical light quark masses ($m_u = m_d = 0.1 \times m_s$). Figure taken from [16].

QCD predicts a phase transition between hadronic matter and QGP above a specific critical temperature T_c. Lattice calculations indicates that at $\mu_B = 0$ there is a smooth transition between hadronic and QGP phases (so called *cross-over*) where the energy density increases rapidly with temperature. Results from recent calculations for energy density ϵ and pressure are shown in Fig. 1.3 [16] and the sharp transition is clearly visible. The critical temperature T_c is estimated to be $150 - 190$ MeV, and the results depend on technical details of the lattice simulations and the method used to extract T_c [8]. It is also postulated that at higher μ_B there is a first order phase transition and therefore a critical point should exist at which the deconfinement phase transition changes its character from cross-over to a first-order phase transition [17, 18, 19]. Lattice QCD calculations indicate that the critical point is expected to exists in the μ_B range of $250 - 450$ MeV [18, 19, 20].

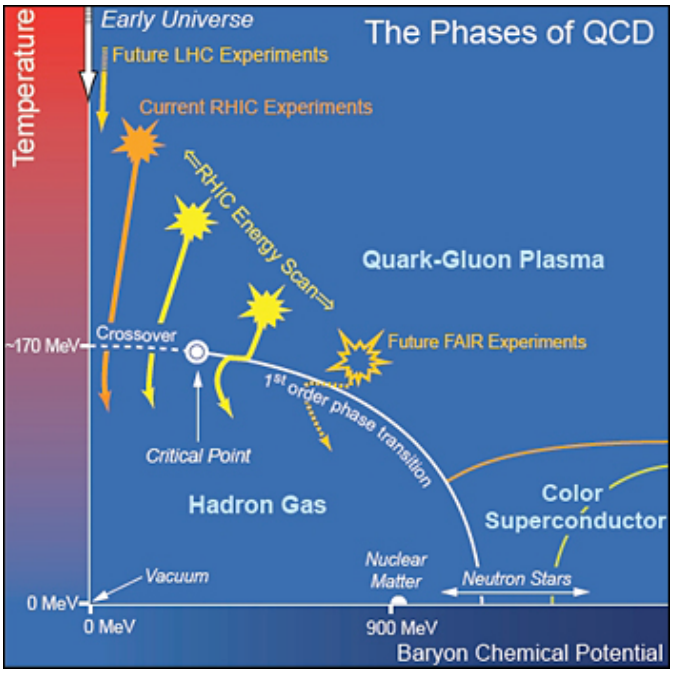

Figure 1.4: Schematic QCD phase diagram of nuclear matter. The lines show the phase boundaries and the solid circle represents the critical point. Possible trajectories for systems created at different accelerator facilities are also shown. Figure taken from [21].

1.2 Relativistic Heavy Ions Collisions - experimental exploration of QCD phase diagram

Ultra-relativistic heavy ion collisions allow us to explore the QCD phase space diagram in a laboratory by creating dense nuclear matter at high temperatures. If the energy density is high enough (greater than 1 GeV/fm^3 [15]) then Quark-Gluon Plasma can be created. When the system expands and cools down, quarks from the deconfined phase are converted into hadrons (this process is called hadronization or chemical freeze-out). The system continues its expansion and at some point its density is low enough that hadrons any longer interact with each other. The moment, when the hadronic interactions stop and particles start to stream freely to a particle detector, is called a kinetic freeze-out.

At high energy collisions provided by Relativistic Heavy Ion Collider (RHIC) and Large Hadron Collider (LHC) accelerators, we can study nuclear matter at high temperatures and $\mu_B \simeq 0$. Collisions with lower energies provide an opportunity to investigate properties of nuclear matter at lower temperatures and higher μ_B and to uncover evidence of a critical point and the first-order phase transition associated with it. The search for the critical point and the

onset of deconfinement is a subject of the ongoing Beam Energy Scan program being carried out by the STAR collaboration [20], and of the future of NA61 experiment [22].

So far, the highest energy nucleus-nucleus collisions have been provided by RHIC, with $\sqrt{s_{NN}} = 200$ GeV. There is strong experimental evidence that QGP is created in Au-Au collisions at $\sqrt{s_{NN}} = 200$ GeV and that the plasma is strongly coupled. In the next paragraphs I will briefly describe the most striking examples:

- high-p_T inclusive hadron production quenching
- di-jet production in Au+Au collisions
- elliptic flow
- heavy flavor production quenching and elliptic flow.

High-p_T inclusive hadron production quenching

An important tool in studying properties of a matter is a tomography technique in which a probe with well know properties is propagated through the medium and the properties of the medium are deducted based on the modification of the properties of the probe. In heavy ions collisions the studied medium is Quark-Gluon Plasma and the best probe would be a fast parton. A fast parton is not directly observable, but its interaction with the medium is reflected in a hadron cluster created in the parton fragmentation (jet), particularly in the leading high p_T hadrons [13]. Jet production is a hard process and is very well described by pQCD, therefore jets and its leading hadrons are good probes of the QGP.

At RHIC energies, the modification of particle production in the medium is quantified by a nuclear modification factor R_{AA}:

$$R_{AA}(p_T) = \frac{\mathrm{d}^2N/\mathrm{d}y\mathrm{d}p_T^{A+A}}{\langle N_{coll}\rangle\ \mathrm{d}^2N/\mathrm{d}y\mathrm{d}p_T^{p+p}} \tag{1.2}$$

which is a ratio of the particle production in nucleus-nucleus collisions $\mathrm{d}^2N/\mathrm{d}y\mathrm{d}p_T^{A+A}$ to the production rate in elementary (proton-proton) collisions $\mathrm{d}^2N/\mathrm{d}y\mathrm{d}p_T^{p+p}$, scaled by the average number of binary collisions in the reaction, N_{coll}. If there is no modification in the medium, then the production in A+A is a simple superposition of the nucleon-nucleon interactions and $R_{AA} = 1$. Hard processes are expected to follow such scaling. If the production is suppressed in Au+Au compared to $p + p$ then such phenomena is called *quenching*. At lower p_T we expect

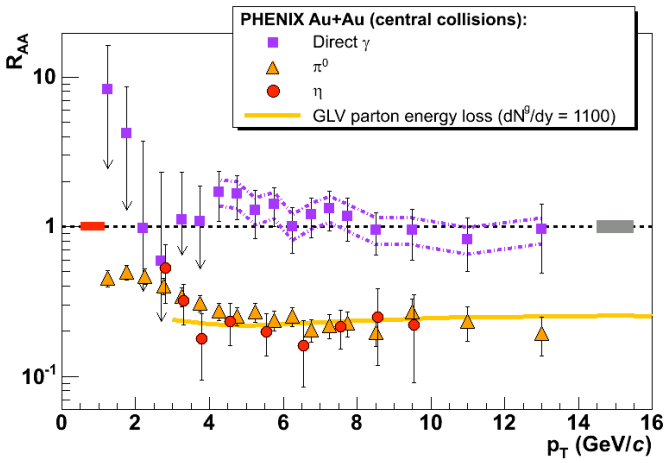

Figure 1.5: The nuclear modification factors for photons, η and π^0 in central Au+Au collision at $\sqrt{s_{NN}} = 200$ GeV at RHIC. Figure taken from [24].

a reduced production rate due to stronger interactions, while at high-p_T it is expected that the R_{AA} should approach unity because fast particles interact weakly with the medium.

At RHIC, quenching at high p_T was observed in A+A collisions for all hadrons except J/ψ [23]. What is striking at RHIC is that π^0 and η, which are leading particles of jets, are suppressed by factor 5 at p_T >5 GeV/c (Fig. 1.5 [24]). This is interpreted as a medium-induced energy-loss of partons traversing a very dense medium, which takes place before a parton fragments into a given hadron. The parton deposits its energy into the medium by collisions with soft particles (the collisional energy loss) or radiating gluons (QCD Bremsstrahlung or radiative energy loss) which leads to the production of many soft particles, instead of fragmentation into high-p_T leading particles [24, 25, 26]. The medium is so dense that is rather built up by quarks and gluons than hadrons, with large parton density (for example, the result of theoretical model calculations shown in Fig. 1.5 were obtained assuming the gluon density $dNG/dy = 1100$).

Quenching is not observed in d+Au and therefore cannot be attributed to "normal" nuclear matter. In addition, the R_{AA} for photons, which do not interact strongly, is ~ 1 as expected.

Di-jet production in Au+Au collisions

Jets are produced through the fragmentation of a hard-scattered parton into a cluster of hadrons in a cone around the direction of the original parton. The leading hadron is usually closely aligned with the original parton direction [27]. Consequently, jet–like correlations can be measured on a statistical basis by selecting a high-p_T trigger particle and measuring the az-

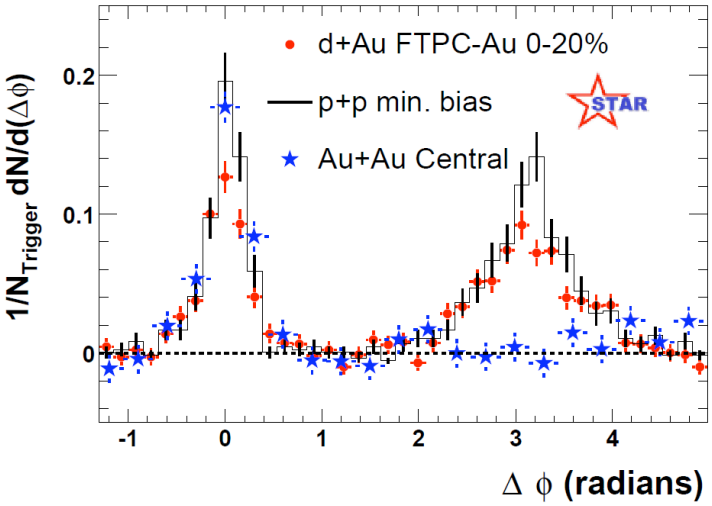

Figure 1.6: The di-hadron azimuthal correlation in $p+p$, d+Au and Au+Au central collisions measured by STAR. Figure taken from [28].

imuthal correlation of its associated hadrons, where $p_T^{Assoc} < p_T^{Trigger}$ [27]. The correlation function is given by $dN/d\Delta\phi$ where $\Delta\phi = \phi^{Assoc} - \phi^{Trigger}$, $\phi^{Trigger}$ is the azimuthal angle of the trigger particle, and ϕ^{Assoc} the azimuthal angle of the associated hadron. Figure 1.6 [28] shows the di-hadron azimuthal correlation for $2 < p_T^{Assoc} < 4$ GeV/c measured by STAR at $\sqrt{s_{NN}} = 200$ GeV. In $p+p$ and d+Au collisions, the di–jet signal is clearly visible, with two distinct back-to-back peaks seen at the same-($\Delta\phi \approx 0$) and opposite-side ($\Delta\phi \approx \pi$). However, in central Au+Au collisions the opposite side jet disappears, which is interpreted as an absorption of one of the jets by the very dense matter produced in Au+Au collisions know as jet quenching. When the di-jet is produced near the surface of QGP fireball, then one of the jets travels only a short distance in the matter, and leaves the system without any significant modification. On the other hand, the second jet spends much more time traversing the medium, and experiences a large medium-induced energy loss (as described in the previous section), which leads to the production of many soft particles with p_T below the p_T threshold for associated hadrons. This cause a suppression of the opposite-side peak.

Elliptic flow

In non-central collisions, the high energy density collision zone has an almond shape in the transverse plane, which can be approximately describe by an ellipse (Fig. 1.7). The initial pressure gradients are larger along the minor axis than along the major one. The pressure gradients

and parton or particle interactions translate the initial spacial anisotropy into the momentum anisotropy of hadrons in the final state. The final state momentum anisotropy is called*flow* and it can be measure experimentally.

A convenient way to quantify the flow phenomena is to use a Fourier expansion to describe the momentum distribution of final state particles [29]:

$$E\frac{d^3N}{d^3p} = \frac{1}{2\pi}\frac{d^2N}{p_T dp_T dy}\left(1 + \sum_{i=1}^{\infty} 2v_n cos\left(n\left(\phi - \Phi^{RP}\right)\right)\right) \tag{1.3}$$

where Φ^{RP} is the reaction plane angle in the laboratory frame, shown in Fig. 1.7. The reaction plane is defined by the velocity vectors of two colliding nuclei. The coefficient v_1 is called *direct flow*, since it corresponds to an overall shift of the distribution in the transverse plane. The coefficient v_2 is called *elliptic flow* and it is used to quantify the eccentricity (a difference between the major and the minor axis) of an ellipse-like distribution [29].

Since the flow originates from the initial spatial anisotropy, it is expected to provide valuable information about the matter in the early stages of the collisions.

Figure 1.8 [30] shows v_2 per constituent quark for selected mesons (composed of 2 constituent quarks) and baryons (composed of 3 constituent quarks) vs. p_T. The results agree very well for all presented particles at intermediate p_T ($2 < p_T < 5$ GeV/c). This phenomenon can be explained on the basis of the quark coalescence models [31, 32, 33, 34]. These models assume that hadrons are formed by recombining constituent quarks which can carry their own elliptic flow before hadronization, and hadron elliptic flow is created from the quarks' v_2. Therefore the elliptic flow is developed on the partonic stage, indicating that the system was in a deconfined stage before hadronization. An additional validation of a pre-hadronic development of the elliptic flow is provided by the v_2 of the ϕ meson. ϕ, which is a bound state of s and $\overline{s}$ quarks, has a small cross-section for hadronic interactions with non-strange hadrons [35]. If the elliptic flow is developed in a hadronic phase, then one expects the v_2 of ϕ to be significantly smaller than v_2 for other hadrons. The experimental results show that elliptic flow of ϕ meson is similar to v_2 of light mesons (π and *K*), despite the large ϕ mass [36]. The v_2 of ϕ is consistent with number-of-quark scaling for mesons, which indicates the development of collectivity on the partonic stage, and not in the hadronic phase.

The mass dependence of v_2 at low p_T (up to 2 GeV/c) is fairly well described by ideal hydrodynamical models [30, 15] which assume a fast equilibration time ($0.6 - 1$ fm/c), the QGP equation of state and a high energy density (~ 20 GeV/fm^3). Such an agreement suggests

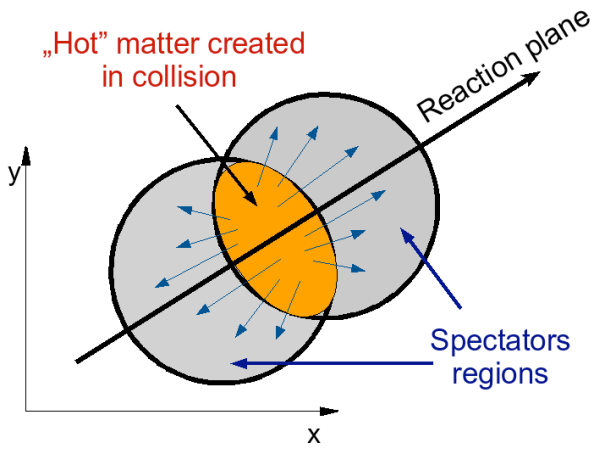

Figure 1.7: An illustration of a non-central collision geometry in a transverse plane. The orange ellipse-shape area represents hot nuclear matter created in the collision.

that QGP behaves like a nearly ideal fluid. In addition, the short equilibration time as compared to a partonic system lifetime (the hadronization time is $\tau_H \simeq$ 3 fm/c [15]) implies that QGP is a strongly interacting matter [15].

Elliptic flow and the quenching of heavy flavor production

Figure 1.9 [37] shows the nuclear modification factor and the elliptic flow for electrons from heavy flavor (B and D mesons) decays, so called non-photonic electrons, which serve as a proxy for heavy flavor production (details of selecting these electrons are described in [37]). At high-p_T, heavy flavor production is strongly suppressed (by factor 5), with a similar suppression level as light flavor. In addition, the non-photonic electrons exhibit a significant flow of 0.1 at $p_T \simeq 1.5$ GeV/c. These are surprising results, since charm and beauty quarks are much heavier than light quarks and therefore are expected to need a longer time to thermalize, resulting in a smaller flow. It was also expected that the heavy flavor interactions with the medium are smaller than the light flavor, and therefore the light quark jets should be quenched more than the heavy quarks ones. Despite various theoretical attempts to describe the data, it is fair to say that the impact of the matter created at RHIC on heavy quarks is not well understood yet. However, heavy flavor jet quenching and flow indicate that the matter is extremely dense and strongly interacting.

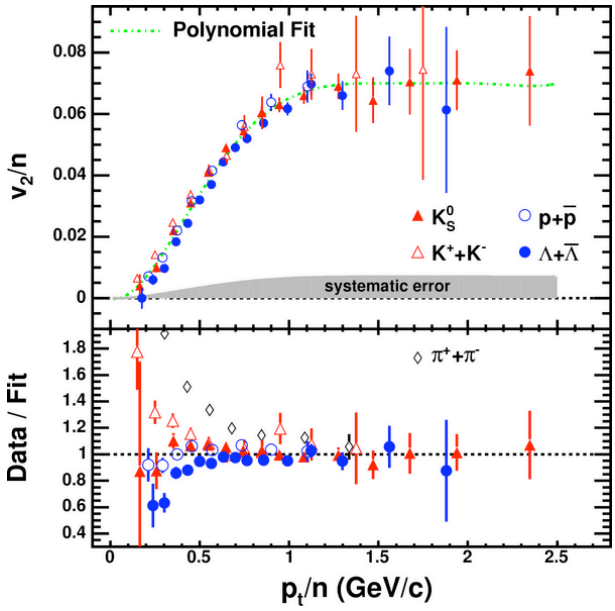

Figure 1.8: The elliptic flow per constituent quark vs. p_T for various particles in min-bias Au+Au collisions at $\sqrt{s_{NN}} = 200$ GeV collisions at RHIC. Figure taken from [30].

1.3 Quarkonia as a probe of Quark-Gluon Plasma

The formation time for heavy quarks can be estimated by $t^{prod} \approx 1/2m$, where m is mass of a quark. For charm this leads to $t_c^{prod} = 1/2m_c \leq 0.1$ fm/c. On the other hand, the nuclei interpenetration time (time needed for colliding nuclei to cross each other) can be estimated using $t \approx 2R/\gamma$ where R is a radius of the nucleus and γ is a Lorentz factor. For SPS, RHIC and LHC energies the interpenetration time is [45]:

- SPS: $t \geq 1$ fm
- RHIC: $t \leq 0.2$ fm
- LHC: $t \leq 5 \times 10^{-3}$ fm

At SPS and RHIC, charm quarks are produced at the very early stage of the collisions and they are present during the whole evolution of the created matter. Also, since $m_c \gg \Lambda_{QCD}$, charm production can be calculated in a framework of perturbative QCD [38], and therefore is very useful probe to study the properties of a hot and dense matter created in heavy ions collisions.

From a historic perspective, J/ψ gained a lot of attention since Matsui and Satz predicted that the suppression of J/ψ production in nucleus-nucleus collision would serve as an unam-

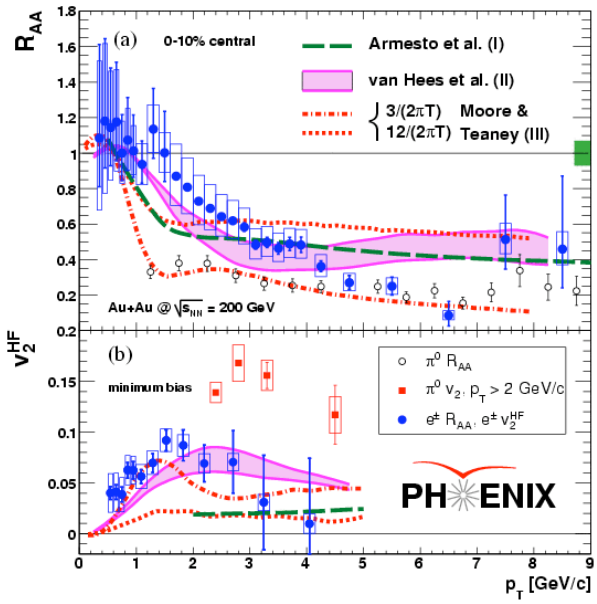

Figure 1.9: The modification of heavy flavor electrons production in medium (upper panel) and the elliptic flow vs. transverse momentum (lower panel) at Au+Au collisions at RHIC. Figure taken from [37].

biguous signature of QGP formation [39]. The suppression was expected to occur due to color screening of the binding potential in QGP, a process similar to the Debye screening in a classic electromagnetic plasma. The early quantitative calculations used the screening in the form obtained in one-dimentional Quantum Electrodynamics [40]. The Cornell potential was used to describe the confining potential for a $c\bar{c}$ pair at the separation distance r:

$$V(r) = \sigma r - \alpha/r \tag{1.4}$$

where σ is the string tension and α is the gauge coupling. In QGP, the potential is modified in the presence of color charges and the Debye-screening leads to:

$$V(r,T) = \frac{\sigma}{\mu}\left(1 - e^{-\mu r}\right) - \frac{\alpha}{r}e^{-\mu r} \tag{1.5}$$

for the screened Cornell potential, where $\mu(T)$ is screening mass (inverse Debye radius) for the medium at temperature T [40]. The first calculations showed that χ_c and ψ' dissociate at $T \simeq T_c$, while J/ψ would survive up to about 1.2 T_c.

Later on this concept was extended to other members of the quarkonia family and was extensively studied using potential models as well as lattice QCD [41]. These studies led to the concept of quarkonia as a QGP "thermometer": the suppression of different states is defined

by their binding energy and the medium temperature, and therefore the quarkonia suppression pattern would set a model-depended upper limit of the QGP temperature, although the predicted melting temperatures vary in different calculations [42, 43, 44, 41].

However, there are complications to this simple picture. First of all, J/ψ production rates can be reduced by so-called cold nuclear matter effects (processes not connected to QGP, described in section 1.4.2) and other effects in QGP, like the recombination of c and $\overline{c}$ [45, 46, 47] or gluon dissociation (by collisions with energetic gluons) [41].

In light of the discussion on J/ψ interactions with the medium, the important feature is the time required for J/ψ formation $t_{c\overline{c}}$ i.e. the time needed to form a mesonic wave function. There is no consensus as to what this value is and if it is smaller than the QGP formation time. For example, in [40] the formation time is estimated to be 0.25 fm, while in [45] $t_{c\overline{c}} = 1$ fm/c. This time scale has an important consequence: in the classic approach of Matsui and Satz, J/ψ (or at least pre-resonance $c\overline{c}$ state) is created early, before QGP formation, and then it is destroyed due to the color screening in the QGP. While in the second approach ,all J/ψ are formed late via statistical coalescence at the QGP phase boundary (chemical freeze-out). In such case the concept of QGP "thermometer" is no longer valid.

The aforementioned models represent only a small fraction of the theoretical approaches to describe J/ψ interactions with nuclear matter. A comprehensive review of them can be found in [41].

1.4 Quarkonia interaction with the medium – experimental aspects

Quarkonia interaction with a medium created in nucleus-nucleus collisions is a complicated process. The strategy used to disentangle at least cold nuclear matter effects from the suppression in QGP involves a factorization of the problem. The typical experimental procedure includes:

- reference measurements: quarkonia production in $p + p$ collisions
- studies of cold matter effects in p+A or d+Au collisions
- measurement of the suppression in nucleus - nucleus collisions

- the suppression due to QGP effects is studied in nucleus - nucleus collisions after subtraction of the cold nuclear matter effects

Each stage brings its own difficulties in the interpretation of J/ψ suppression in QGP. The most important aspects are described in next paragraphs.

1.4.1 Quarkonia production mechanism

The J/ψ interaction with nuclear matter may include the J/ψ production via statistical coalescence. Consequently, the understanding of the charmonium production is necessary to draw conclusions about the in-medium behavior of quarkonia. The production of $c\bar{c}$ is relativelly well understood and can be calculated in pQCD framework. In high energy collisions, proton structure is dominated by gluons (Fig. 1.10 [48]). Consequently in high energy $p+p$ collisions, the charmonium production is dominated by gluon fusion (96% of $c\bar{c}$ pairs are created in such process and contributions from $q\overline{q}$ fusion or gluon fragmentation are small). On the other hand, the J/ψ formation still lacks of an understanding. Over time, a few different models of quarkonia production have been proposed. In this section, we briefly discuss the major theoretical developments together with their successes and failures. A comprehensive review can be found in [49].

Color Singlet Model

Color Singlet Model (CSM) [50, 51, 49] is the first and the most straightforward implementation of QCD to the quarkonia production . The name comes from the assumption that color and spin of heavy quark-antiquark pair $Q\overline{Q}$ do not change during binding, and therefore $Q\overline{Q}$ is created in a color-singlet state. The first version of the CSM, with several kinematic assumptions, failed to described charmonia hadro– and photoproduction in high energy collisions. The predicted production rates falls far bellow the measured cross-sections and the discrepancy grows with p_T. Recently, CSM underwent a set of improvements [52, 53] and the new CMS calculations, with higher order corrections, describe the low-p_T J/ψ spectrum at RHIC and Υ production at Tevatron. Hoverer, there is still a discrepancy at RHIC at very high-p_T[23]. Moreover, the model qualitatively describes the Υ polarization at Tevatron energies, and quantitatively the J/ψ polarization at RHIC at mid-rapidity [54].

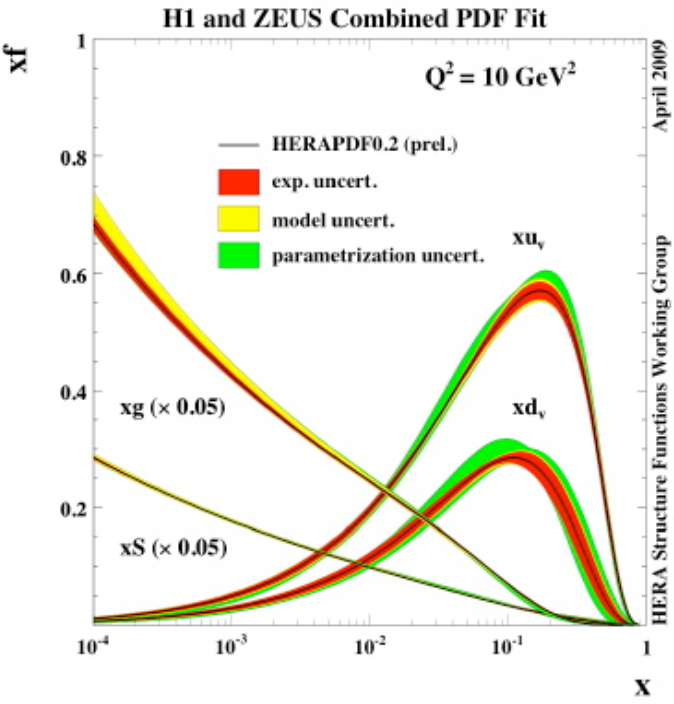

Figure 1.10: Parton distribution functions of the proton obtained by the HERA Structure Functions Working Group at the scale of $Q^2 = 10\ GeV^2$. The PDFs are shown separately for the gluon (xg), the sea quarks (xS), (both scaled down by a factor of 20), and the valence quarks up xu_v and down xd_v. Figure taken from [48].

Color Octet Model

Color Octet Model (COM) [55, 49] was developed within Non-Relativistic Quantum Chromodynamic (NRQCD) which is an effective field theory. Quarkonia in COM, besides a color singlet state, can be produced by coloured pairs, and then the color is neutralized by emission of one or a few soft glouns. The important consequence of color-octet channel is that the quarkonia can be produced by a single gluon, and therefore the production rates are larger. Color Octet Model describes correctly the quarkonia p_T spectrum at RHIC and Tevatron energies. However, it also predicts a strong transverse polarization at very high p_T, which disagrees with CDF measurement of J/ψ, ψ‘ and Υ polarization [49].

Color Evaporation Model

In Color Evaporation Model (CEM) [56, 57, 58, 49], the $Q\overline{Q}$ pairs are produced in a color octet state, and then numerous soft-gluon emissions are required to change their quantum state to a

color singlet state. Consequently, the final quantum state of $Q\overline{Q}$ pair is randomize, and it is not correlated with quantum numbers of the originally produced pair. Therefore CEM is unable to predict the J/ψ polarization, which is one of the major test of the quarkonium production models.

The charmonium cross-section in CEM is a fraction of all $Q\overline{Q}$ pairs within a mass range from the treshold of two charm quarks $2m_C$ up to a threshold for the production of two charmed mesons $2m_D$. CEM describes the quarkonium cross-section very well (because of introduction of an implicit color octet channel) and is a useful tool to study the charmonium production in p+A and A+A collisions

Summary

The description of quarkonium production even in $p + p$ collisions remains a challenging task. Despite a lot of new theoretical developments over last 20 years, there is no model which provides a satisfactory and consistent description of all available observables. Most probably the quarkonia production at very high-p_T is dominated by color-octet channel, although the interplay of a color-singlet and color-octet states at lower p_T is unclear.

1.4.2 Cold nuclear matter effects

The cold nuclear matter effects (CNM) are the effects which affect the charmonim production in nulceus-nucleus collisions, and cannot be attributed to the deconfined state. There are two main classes of CNM effects:

- initial state: these are the modifications of the gluon distribution functions, which affect the charmonium production prior to $c\bar{c}$ formation,
- final state, which include the inelastic interaction of the $c\bar{c}$ pre-resonance state and J/ψ with the nuclear medium

Initial state effects

The modification of parton densities in nucleus compared to those distributions in a free proton is the most important source of initial state effects. Such a modification is often called the shadowing, and as the quarkonia are mostly produced via gluon fusion, we will use this term to refer to the gluon shadowing.

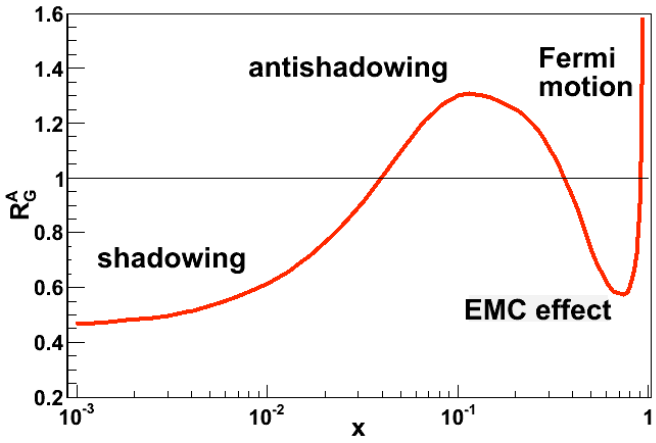

Figure 1.11: An illustration of the nuclear modifications function $R_A(x)$ for gluons with different effects presented.

Parton distribution function (PDF) describes the probability of finding a parton (quark or gluon) carrying a given fraction of proton momentum x for a given momentum transfer Q. The nuclear PDF can be characterized by ratio of PDFs in bound and free proton $R_A(x, Q^2)$:

$$R_A(x, Q^2) = f_A(x, Q^2)/f_p(x, Q^2) \tag{1.6}$$

The a typical structure of $R_A(x, Q^2)$ distribution is presented in Fig. 1.11. There are a few effects which can be identify:

- Shadowing – $R_A(x, Q^2) < 1$ at small x, it is a depletion of gluons in bound nucleon compared to free proton, the shadowing leads to reduction of J/ψ production at RHIC energies.
- Ant-shadowing – $R_A(x, Q^2) > 1$ at intermediate x
- EMC effect – $R_A(x, Q^2) < 1$
- Fermi motions at large x

Nuclear PDFs are not well know, and the result obtained using different approaches vary significantly [59].

Other important initial state effects includes:

- Cronin enhancement [60, 40] - initial parton multiple scattering on the incoming nucleus leads to a broadening of the transverse momentum spectrum

- Initial parton energy loss [61] - energy loss by the incoming parton as it traverses the nucleus

Final state effects

The final state effects are the effects due to inelastic interaction of J/ψ (or pre-resonance state $c\bar{c}$) with the nuclear medium, which consists of:

- nuclear absorption – an absorption by interactions with nucleons
- absorption by hadronic co-movers - an absorption by interaction with other produced particles

The final state effects are difficult to distinguish and usually are folded into one effective nuclear absorption cross-section σ_{abs}.

Cold nuclear matter effects - experimental approach

The suppression due to cold matter effects is an interplay of the initial and final state effects. Typically, only a shadowing and a nuclear absorption are taken into account in practical applications. The shadowing depends strongly on nPDF parametrization. Moreover, the small change of x may cause large change in the gluon density. Furthermore, the variable x for gluons participating in J/ψ production is unknown, and depends on kinematics of the process. It is different for color-octet ($g + g \to J/\psi + X$) and color-singlet channel ($g + g \to J/\psi + g$) [62]. In the simplest case, the x for gluons con be determined using $2 \to 2$ scattering kinetics and then x_1 and x_2 read [62]:

$$x_1 = \frac{m_T}{\sqrt{s_{NN}}} e^{y}, \; x_2 = \frac{m_T}{\sqrt{s_{NN}}} e^{-y} \tag{1.7}$$

where $m_T = \sqrt{M^2 + p_T^2}$, y is J/ψ rapidity and M is J/ψ mass.

To analyze the CNM effects, the shadowing parametrization and the nuclear density profiles for a target and a projectile has to be chosen. Then the nuclear absorption σ_{abs} can be parametrized using the Glauber model. Next the value of σ_{abs} is obtained from a fit to the pA data. At RHIC, the R_{dAu} or R_{CP} are used, where R_{dAu} is a nulcear modification factor for d and Au collisions, and R_{CP} is a ratio of the particle production in central collisions compared to peripheral ones, scaled by appropriate number of binary collisions. Examples of such fits to

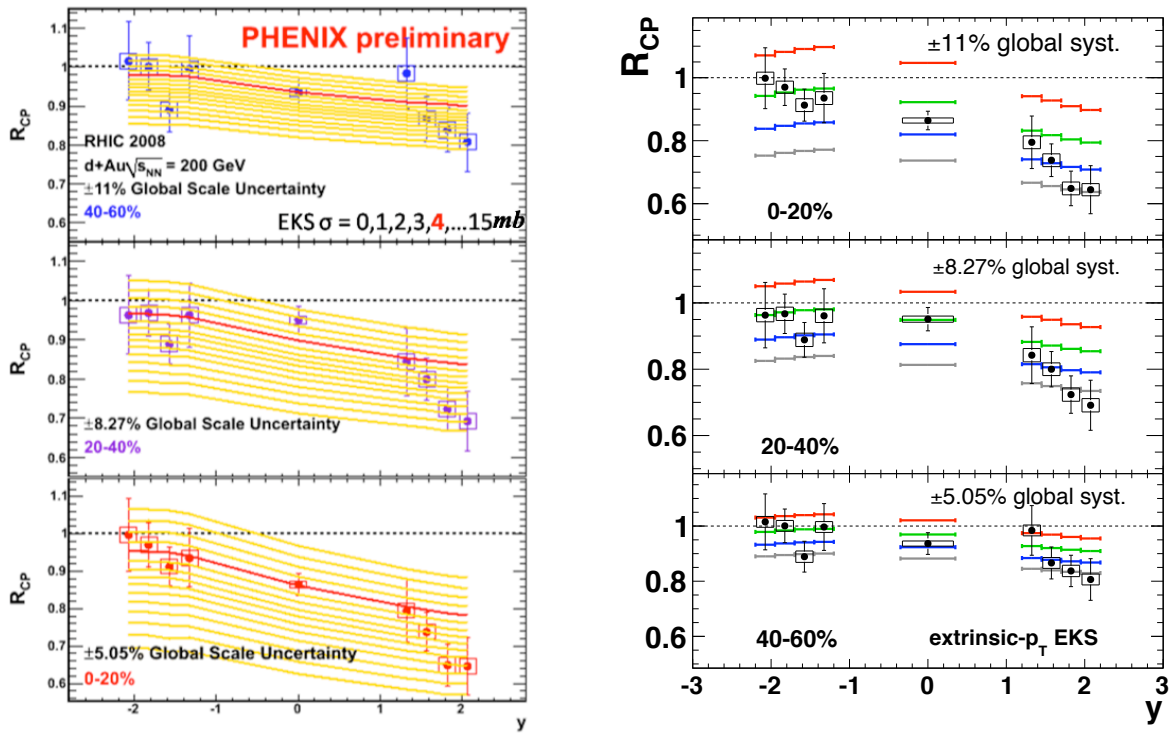

Figure 1.12: J/ψ R_{CP} vs rapidity with cold matter effects predictions for EKS98 shadowing with different nuclear absorption cross-sections using CEM (left) and CSM (right) models. In CSM studies, the values of the nuclear absorption are (from top to bottom): $\sigma_{abs} = 0, 2, 4$ and 6 mb. Figures taken from [63] and [62].

d+Au data are shown of Fig.1.12. Usually the p_T dependence of the shadowing is neglected although recent development takes it into account [62]

Due to uncertainties both on theory (shadowing parametrization) and experiment side, there is rather substantial uncertainty on σ_{abs} calculations. Moreover, the correction for CNM effects are applied by rather simple extrapolation of nuclear absorption from p+A to A+A with Glauber modeling of the shadowing effects. The picture in A+A collisions may be much more complicated, and probably more sophisticated theory of cold matter effects is needed. Nevertheless, an additional effort is required to obtain a good understanding of the cold nuclear matter effects on quarkonia production.

1.4.3 Quarkonia production in nucleus – nucleus collisions

The experimental study of J/ψ production as a signature of the QGP formation started at the CERN Super Proton Synchrotron (SPS) accelerator. The fixed-target experiments NA38 [64],

NA50 [65], NA51 [66] and NA60 [67] measured the charmonium production via di-muon decay channel $J/\psi \rightarrow \mu^+ + \mu^-$ in various systems p+A (proton beam on O, Al, Cu, Pb, Be, W, Pb and U targets) at different energies, and also in In+In and Pb+Pb collisions. The results of those experiments are usually reported as ratio of the J/ψ to the Drell–Yann cross-section, $B\sigma(J/\psi \rightarrow \mu^+ + \mu^-)/\sigma_{DY}$, where B is a Branching ratio for di-miuon decay channel. The Drell–Yan process was chosen because it is a good benchmark – it produces a lepton pair in the final state, it is not modified in QGP, and is well understood, both on the theoretical and experimental side. The interpretation of the data evolved over the years – here we shall focus on the current understanding while the comprehensive review of SPS results can be found in [40] and [41].

As it was mentioned above, the modification of J/ψ production can be separated into two regimes: cold matter effects (or normal nuclear absorption) and "hot matter effects" ("anomalus" suppresion). At SPS energies, the cold matter effects are usually described by the power low fit to the J/ψ production cross-section: $\sigma_{pA} = \sigma_0 \times A^{\alpha}$, or by calculating the absorption σ_{abs} in a framework of the Glauber model. In the latter, the σ_{abs} depends on the number of nucleons which can interact with $c\bar{c}$ pair. Both α and σ_{abs} describe the effective absorption – they describe the final reduction of the J/ψ yield, without differentiation between relative contributions of the shadowing and nuclear absorption.

Most of the p+A data were taken with different energy (200, 400 and 450 GeV) than nucleus-nucleus data (158 GeV) and only recently p+A data at 158A GeV became available. In the previous studies it was assumed that cold matter effects are energy independent and scale only with the mean length (L) of the path of $c\bar{c}$ during its travel in the nuclear matter (in other words, L is a mean thickness of the nuclear matter "seen" by $c\bar{c}$ piar). Then the results of the measurements at higher energies were extrapolated to 158A GeV, and the expected J/ψ yield was compared to the results in nucleus – nucleus collisions. The results obtained with such assumption have shown the anomalous suppression in mid-central and central Pb+Pb and In+In collisions [68]. However, the recent NA60 results (Fig. 1.13 [69]) show that σ_{abs} is energy dependent and the absorption is significantly higher for 158 GeV compared to 400 GeV. With new values of σ_{abs}, the anomalous suppression is significantly smaller in Pb+Pb collisions (it is still effect $\sim 25\%$ in the most central collisions) while the modification of J/ψ production in In+In can be described entirely by the cold matter effects.

The SPS results were initially interpreted as charmonium dissociation in QGP, although

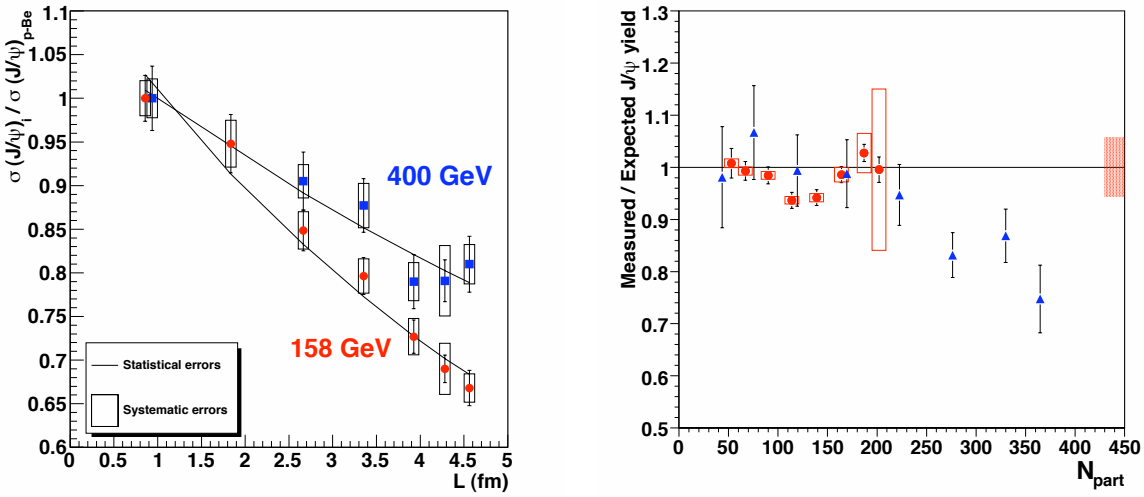

Figure 1.13: Left: Ratio of J/ψ to Drell-Yan cross-sectiosn for p+A collisions at 158 GeV and 400 GeV. Left: Anomalous suppression in Pb+Pb collisions at 158A GeV as a function of centrality. Bares represents statistical error, open boxes - systematic errors and the filled box is uncertainty on the absolute normalization of In+In points. Additional global error of 12% due to absolute normalization of the absorption cross-section at 158A GeV is not shown. Figures taken from [69].

it quickly turned out that they can be also reproduced by alternative approaches [41] and the clear interpretation is still missing. The RHIC data were expected to shed more light on the suppression mechanism as the energy density available at RHIC is much higher than at SPS (the top collision energy at RHIC is $\sqrt{s_{NN}} = 200$ GeV compared to $\sqrt{s_{NN}} = 17.4$ GeV at SPS) and the created system is expected to spend more time in the QGP phase.

When the RHIC data arrived, there was a big surprise because the suppression measured by the PHENIX collaboration at mid-rapidity ($|y| < 0.35$) was on the same level as at SPS, despite energy difference. Moreover, the suppression at forward rapidity $1.7 < |y| < 2.5$ is bigger than at mid-rapidity. Furthermore, models which described SPS data quite well, overestimated the suppression at RHIC[41]. It was taken as a hint that additional process plays role, like recombination c and $\overline{c}$ quarks or sequential suppression of charmonium states. In the latter, the higher excited states melt down both at SPS and RHIC energies, while ground state, J/ψ, survives, which leads to similar suppression pattern. Then the stronger suppression at forward rapidity is caused by another process (for example: nuclear absorption is stronger at forward than at mid-rapidity).

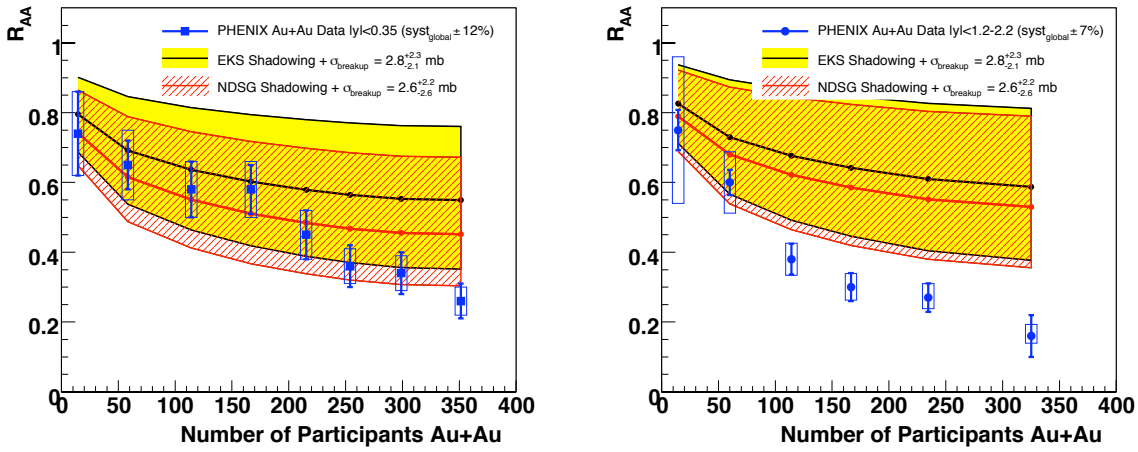

Figure 1.14: J/ψ R_{AuAu} for forward and mid-rapidity with estimates for cold matter effects for two shadowing parametrizsations: EKS and NDSG. Figure taken from [70].

The key problem with interpretation of the R_{AA} is lack of precise information about the cold matter effects. At RHIC, only limited statistics d+Au data (taken in 2003) were published, and only preliminary results of RHIC run 8 (2008) recently became available. The analysis of nuclear absorption in [70] provides a model-dependent information on expected normal J/ψ suppression for both mid- and forward rapidity regions. Within current uncertainties, the J/ψ suppression at mid-rapidity can be accounted for cold matter effects only, while at mid-rapidity the anomalous suppression is visible, which is showed in Fig. 1.14.

The other important quantity is J/ψ p_T spectra. At SPS energies, it was observed that the transverse momentum distribution in p+A and A+A is broadened compared to p+p collisions. It was interpreted as the Cronin effect: initial-state multiply scattering of parton which fuse later on to create a $c\bar{c}$ pair. At RHIC, the precision of the data does not allow to conclude if broadening takes place [71]. Transverse momentum distribution is also sensitive to the production mechanism. If J/ψ is created by statistical coalescence of c and $\bar{c}$ in QGP or at freeze-out, then the probability of the coalescence is higher at low-p_T and at mid-rapidity, where the charm quark density is the highest. Therefore, the p_T spectrum should be steeper at mid-rapidity compared to forward rapidity. At RHIC the $\langle p_T^2 \rangle$ at mid-rapidity and forward rapidity are compatible within error.

At the moment, the results of J/ψ suppression studies at RHIC do not allow us to distinguish between different suppression scenarios. Therefore a new observable was proposed, namely J/ψ elliptic flow, which is expected to shed some light on J/ψ production and in-medium

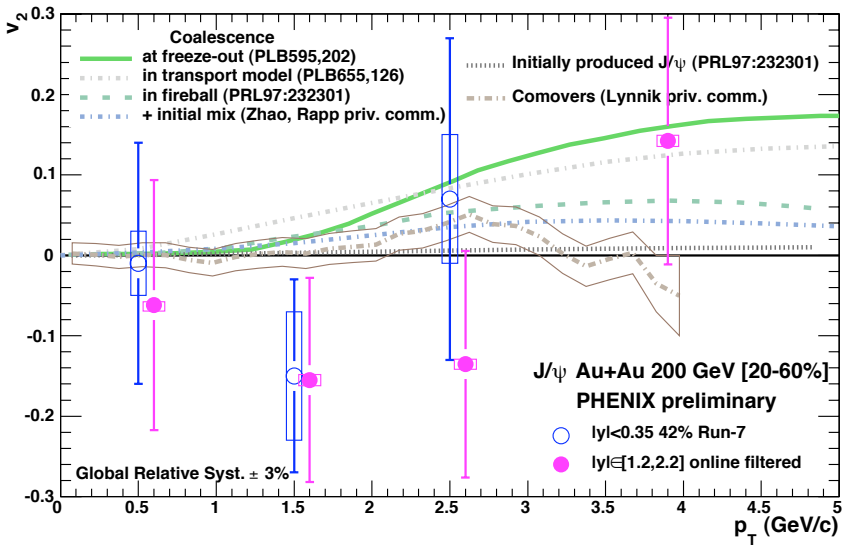

Figure 1.15: J/ψ elliptic flow measured by the PHENIX collaboration in Au+Au collisions at 200 GeV with set of theoretical predictions. Figure taken from [72].

interactions.

1.4.4 J/ψ elliptic flow

At RHIC, a strong positive elliptic flow of non-photonic electrons is observed (see Fig. 1.9) which suggests that charm and beauty quarks flow. If J/ψ is created via statistical coalescence, then should inherit the flow of charm quarks, and a positive J/ψ flow should be observed. Quantitative prediction (Fig. 1.15) show that magnitude of the effect depends on fraction of J/ψ from coalescence. If J/ψ is created before QGP, then a very weak flow is predicted while the coalescence at freeze-out gives a large v_2.

Moreover, if $c\bar{c}$ is in the local thermodynamical equilibrium with QGP, then J/ψ would have a similar flow as lighter hadrons [41]. Nevertheless, there is an open issue with the interpretation of charmonium flow. The positive flow of J/ψ was observed by the NA50 experiment (Fig. 1.16) at SPS energies although one does not expect thermalization there. Furthermore, the effects of charmonium production mechanism and feed-down on elliptic flow are unclear .

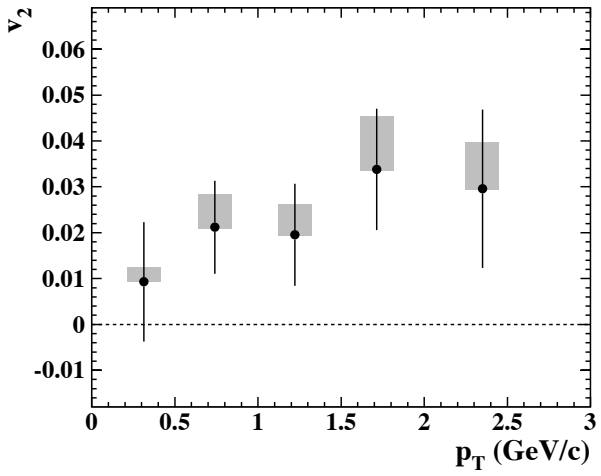

Figure 1.16: J/ψ elliptic flow measured by NA50 collaboration in Pb+Pb 158A GeV. Error bars represent statistical errors and the gray bands are systematic errors. Figure taken from [73].

1.5 Thesis scope

J/ψ is a very important probe to study the properties of the strongly interacting Quark-Gluon Plasma, although a coherent description of J/ψ interactions with the hot and dense medium is still missing. In light of ambiguous model predictions and a lack of solid theory calculations, the experimental input is required to understand this interaction. A systematic measurement is needed in various systems ($p + p$, d+Au and A+A collisions) and the results contained in this thesis are part of the experimental effort being carried out by the STAR collaboration.

In this work, the J/ψ production in Cu+Cu and Au+Au collisions was studied. The total energy accessible in Cu+Cu collisions is smaller than in Au+Au, and therefore allows us to explore J/ψ production for different energy densities and provide an additional handle on the J/ψ suppression mechanism. The results presented in this thesis are limited by available statistics, although they are a valuable cross-check to published results [74, 75]. In addition, we also studied the J/ψ elliptic flow in Au+Au collisions. At the moment this measurements is rather a proof-of-principle of such calculations at STAR, although it will become an important tool for the investigation of QGP thermalization and J/ψ production when the high statistics data are available.

Chapter 2

Experimental Setup

2.1 The Relativistic Heavy Ion Collider

The Relativistic Heavy Ion Collider (RHIC) is a part of accelerator complex located in Brookhaven National Laboratory (Upton, New York). RHIC is capable to accelerate and collide different ions (from deuteron do gold) and polarized protons beams in the wide range of energies. Protons can be accelerated up to 250 GeV while top energy for ions beams is 100 GeV per nucleon. The ability to provide lower energies is a groundwork for RHIC Beam Energy Scan which is being carrying on at the moment. The designed luminosity for Au+Au was $2 \times 10^{26}\, cm^{-2}s^{-2}$ and $1.4 \times 10^{31}\, cm^{-2}s^{-2}$ for p+p although ongoing upgrade (stochastic cooling) together with other improvements will allow to increase the luminosity. In addition a new electron beam ion source (EBIS [76]) will provide a broader range of ions to accelerate.

The overall complex for ions acceleration consist of Tandem Van de Graff, the Booster, the Alternating Gradient Synchrotron (AGS) and the Collider itself and it is shown in Fig. 2.1. The detailed overview of RHIC can be found in [77].

2.2 The STAR experiment

STAR (Solenoidal Tracker at RHIC) [78] is a large acceptance, multipurpose experiment composed of several subsystems designed to measure many different observable in the central rapidity region. While RHIC was arranged to produce Quark-Gluon Plasma in nucleus – nucleus collisions, STAR was designed to discover QGP and to study properties of the strongly interactive matter. STAR comprises with several subsystems, which are described in next section,

Figure 2.1: RHIC accelerator complex. Figure taken from [21].

while the heart of the detector is a large volume Time Projection Chamber (TPC). TPC was designed to provide precise measurements of hadron production and momentum analysis together with large acceptance (full azimuthal coverage, tracking capabilities in $|\eta| < 1.8$) which makes STAR well suited for correlation (including anisotropic flow) and fluctuation measurements.

The main subsystems in STAR Detector are:

- Time Projection Chamber (TPC)
- Magnet system
- Barrel Electromagnetic Calorimeter (BEMC)
- Central Trigger Barrel (CTB)
- Endcap Electromagnetic Calorimeter (EEMC)
- Silicon Vertex Tracker (SVT)
- Silicon Strip Detector (SSD)
- Vertex Position Detector (VPD)

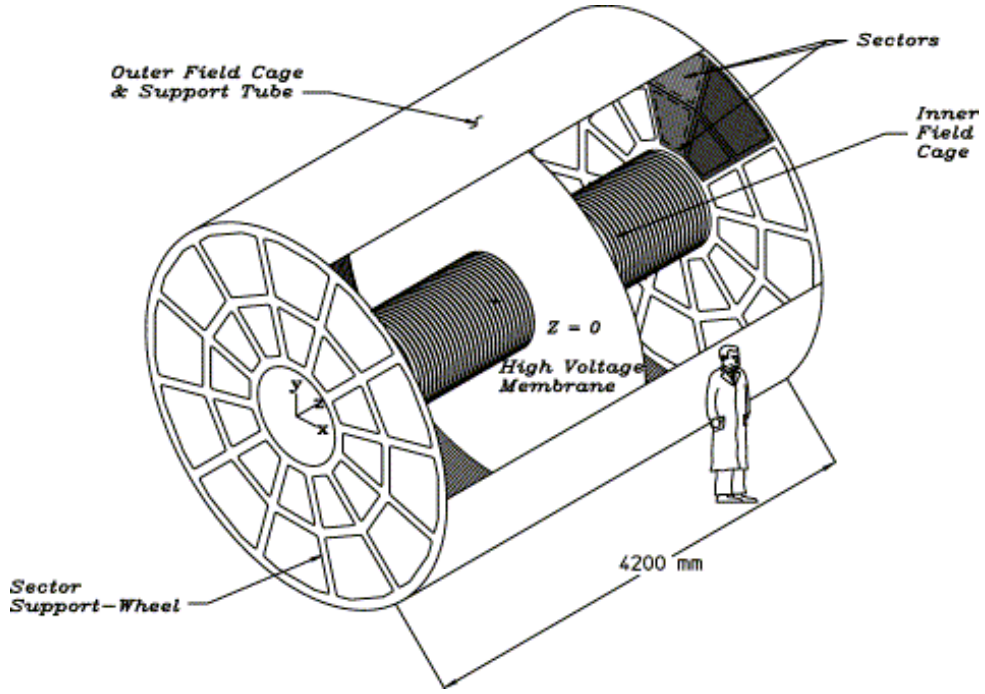

Figure 2.2: The STAR Projection Chamber. Figure taken from [79].

- Zero Degree Calorimeter (ZDC)
- Forward Time Projection Chamber (FTP)

In the analysis described here, the TPC and BEMC were used and will be briefly described in next paragraphs. We also present ZDC and VPD detectors which were part of the trigger system, and SSD and SVT detector which have been used in track reconstruction.

2.3 Time Projection Chamber

Design The Time Projection Chamber (TPC) [79] is the main STAR subsystem. It is designed to reconstruct tracks of charged particles, giving precise information about momentum and ionization energy loss (dE/dx). TPC provides tracking capabilities in $|\eta| < 1.8$ with good particle identification for $|\eta| < 1$ and full azimuthal coverage ($\Delta\phi = 2\pi$).

Schematic view of STAR TPC is shown in Fig. 2.2 [79]. TPC is 4.2 m long with the 4 m diameter and it is located inside STAR magnet, which provides magnetic field of 0.5 T. TPC is filled with P10 gas (10% methane and 90% argon). At the center of TPC there is a thin conductive Central Membrane which, together with concentric field-cage cylinders and readout end caps, defines a uniform electric field, required for precise track reconstruction.

Reconstruction of the particle track, momentum measurement and particle identification via ionizing energy loss is achieved by collecting secondary electrons released by particles passing through TPC gas. These electrons drift to the readout end-cups at the ends of the TPC.

The readout system is based on Multi-Wire Proportional Chambers (MWPC) with readout pads. The readout modules are arranged around circle and mounted to support wheels, 12 modules (sectors) per each end cup. Each MWPC consists of pad plane and three wires planes (anode plane, ground plane and gating grid). As the track density is higher in inner than in outer radius region, two different sectors designs were used. The outer sub-sectors are optimized for dE/dx resolution: they have a continuous pad coverage with no space between padrows. In this setup the full track ionization signal is collected and more ionization electrons improve statistics on dE/dx measurement. The inner sub-sectors are optimized for good two-hit resolution by using smaller pads and the main improvements is due to shorter pad length (12 mm for inner sectors compared to 20 mm for outer ones). The outer sub-sectors consist of 32 padrows while the inner ones include 13 padrows, therefore a particle track in TPC can be sampled 45 times if it crosses all 45 padrows.

Track reconstruction Tracks in TPC are reconstructed by finding ionization clusters along the track. Depending on particle momentum, track curvature, pseudorapidity and other details of trajectory, track of the particle can be sampled by 45 or less pad rows. Clusters are found separately in (*x,y*) and *z* direction where the local *x* axis is along the direction of pad row, *y* axis points from the beam line outwards and it is perpendicular to pad rows and *z* is determined by the beam axis. The *x,y* coordinates of the cluster are determined by the charge registered on adjacent pads in a single pad row. Local *x* is given by a fit to the charge distribution assuming Gaussian pad response function and assuming $y = 0$. Then it is translated to global coordinates using global pad position. The *z* coordinate is determined by measuring the secondary electrons drift time from the origin of the cluster to the anodes on the end cups and dividing by the average drift velocity. To obtained sufficient accuracy on *z* position, the drift velocity has to be known with a very high precision (0.1%).

The final stage of track reconstruction involves using a designated software to form tracks from reconstructed points and fitting points on the track with a track model. The last step allows to extract momentum and other information about a particle. The first order track model is a helix, second order effects include the energy loss in the TPC gas and cause a small deviation from the helix. Tracking [80] proceeds in two steps: a) candidate ("track seed") finding and

track extension, b) track model fitting. Tracking starts at the outer pad rows where the hit density is lowest and it is easier to find a reliable track pattern. The first step uses a Kalman filter approach[80, 81] to find track candidates (at least 3 hits close in space). Track seed is fitted with straight line and it is extrapolated inwards in order to find additional hits. If located, then a helix is associated with all hits and it forms a track segment. The helix is used by Kalman finder to begin the extension and look for additional hits in TPC. Since most of the seeds predominantly lie near the edge of the detector, Kalman search proceeds firstly inwards. Hit is added to a segment if it lies within radius determined by error parameters of the helix. Once hit is added, the track parameters (curvature, direction etc.) are refined using the track model. When the first inward track projection is completed, then the similar outward extension is performed. At the last stage, segments are merged if they are results of track splitting, and the global Kalman refit is performed. Track is required to have hits on at least 10 pad rows because shorter tracks are probably broken tracks fragments. When the track in TPC is constructed, tracking algorithm uses additional space points from inner track detectors SVT and SSD (if the information is available) to do final fit and construct a *global track*. The outliers hits (hits that lie too far from best fit) are discarded from fit in order to improve track momentum resolution.

Momentum resolution of the track can be improved when the primary event vertex is used in the track reconstruction. The primary vertex is found by extrapolating all reconstructed track in TPC back to the origin and then the global average gives the vertex position. Vertex resolution increases with number of tracks in TPC and $350\ \mu m$ is achieved when there are more then 1000 tracks [79]. Tracks with distance of closes approach less than 3 cm to vertex are next refitted with primary vertex position included in the fit. These tracks are called *primary tracks*.

Tracking efficiency and momentum resolution are estimated using Monte Carlo simulation described in section 3.6.1. Tracking efficiency depends on TPC acceptance, the electronics detection efficiency and to two-hit separation ability. Due to possible track merging, efficiency depends also on event multiplicity. Figure 2.4 presents results of the efficiency studies for Au+Au with different multiplicities. For low p_T tracks the efficiency drops because the particles spiral up and do not cross enough pad rows. For the higher p_T efficiency reaches plateau 75% - 90% (depending on event multiplicity). The momentum resolution for Au+Au events is shown in Fig. 2.5 for π^- and $\overline{p}$ in magnetic filed 0.25 T. For the lower momentum the $\Delta p_T/p_T$ is determined by Coulomb scattering while for higher momentum the $\Delta p_T/p_T$ is limited by strength of the magnetic field and TPC spatial resolution. The best relative resolution was

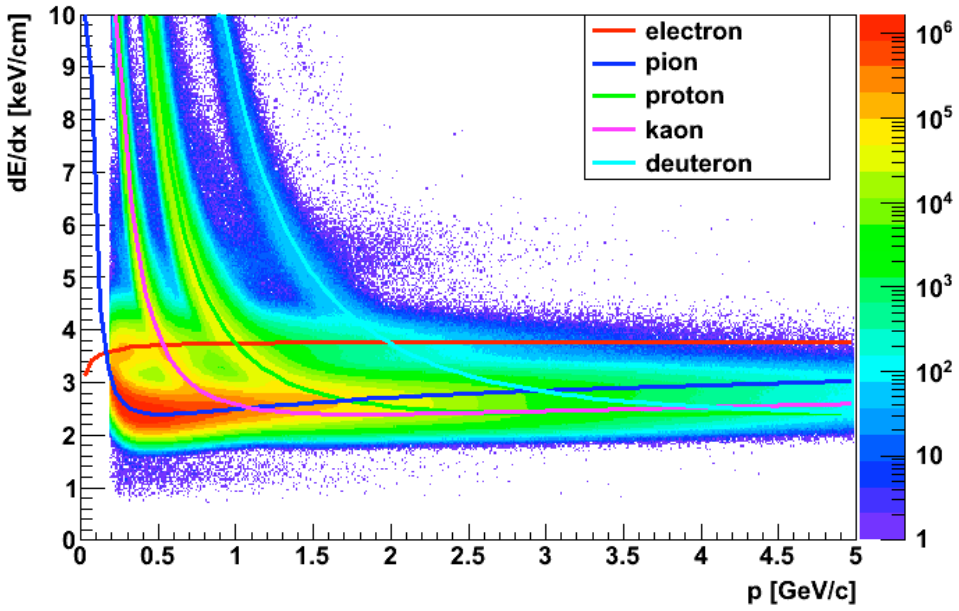

Figure 2.3: dE/dx spectrum measured in Cu+Cu collisisons at $\sqrt{s_{NN}} = 200$ GeV.

found between those two regimes (2% for pions and 3% for anti-protons). Figure 2.5 shows momentum resolution for electrons from J/ψ decays in Cu+Cu collisions with magnetic field of 0.5 T - improvement due to stronger magnetic field and lower hits density is visible.

Particle identification Particles in TPC can be identify using their ionization energy loss dE/dx. dE/dx is extracted using ionization measured up to 45 pad rows and the length over which energy loss is measured is too short to average out ionization fluctuations. Therefore one can not determined mean dE/dx [79] accurately and the most probable energy loss is measured instead. It is determined by calculating a truncated mean: a quantity where 30% of ionization clusters with the larges signal is removed [82].

An example of dE/dx distribution (plotted using 70% truncated mean) for Cu+Cu 200 GeV collisions is shown in Fig. 2.6. The data are compared to theoretical calculations for most probable energy loss in Argon – so called Bichsel functions [82, 83].

2.4 Barrel Electromagnetic Calorimeter

The STAR Barrel Electromagnetic Calorimeter [84] is a sampling calorimeter with full azimuthal coverage, surrounding the TPC. It covers $|\eta| < 1$ and full azimuthal angle. It is divided

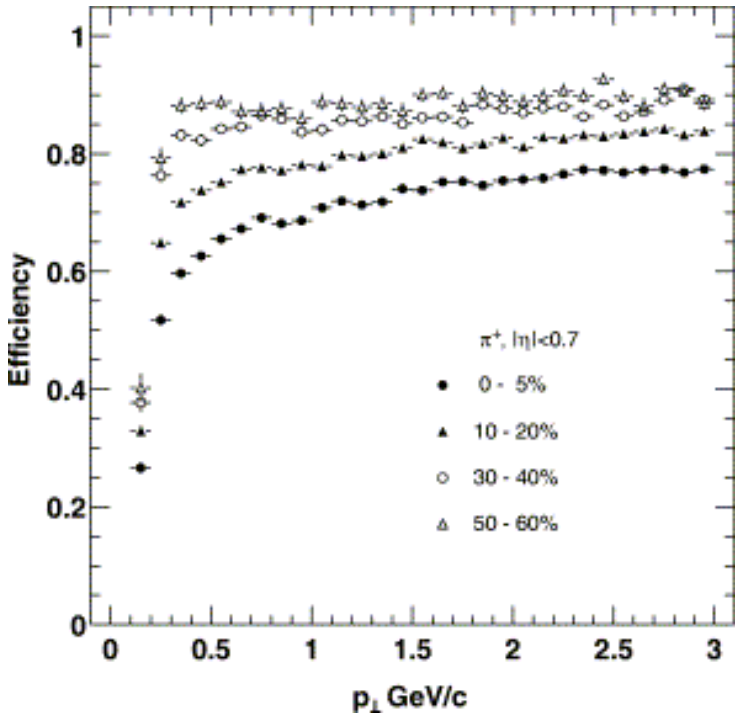

Figure 2.4: The pion tracking efficiency in STAR for Au+Au events with different centrality. Results were obtained for tracks with $|y| < 0.7$ with magnetic field set to 0.25 T. Figure taken from [79].

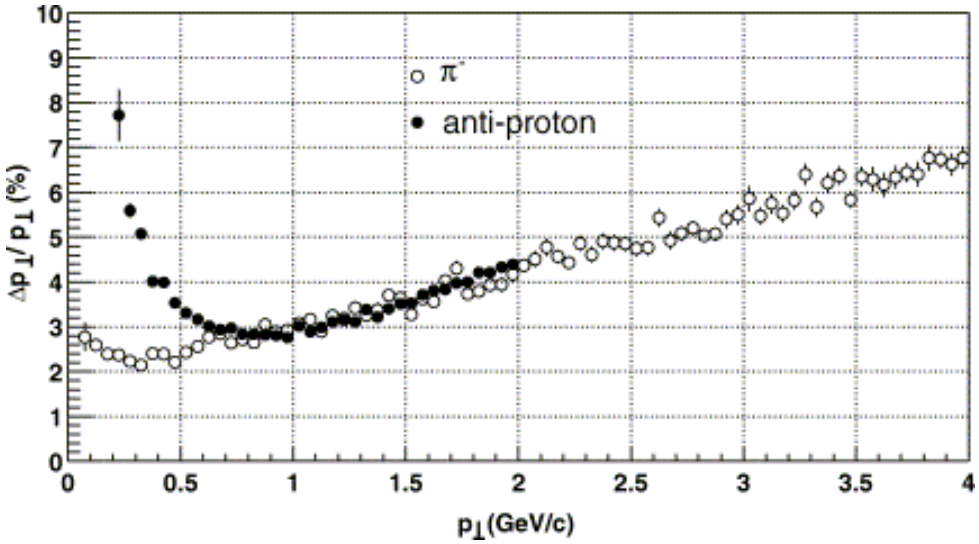

Figure 2.5: Transverse momentum relative resolution for π^- and $\overline{p}$ with at least 15 hits in TPC. Results were obtained for minimum-bias Au+Au events and with magnetic field set to 0.25 T. Figure taken from [79].

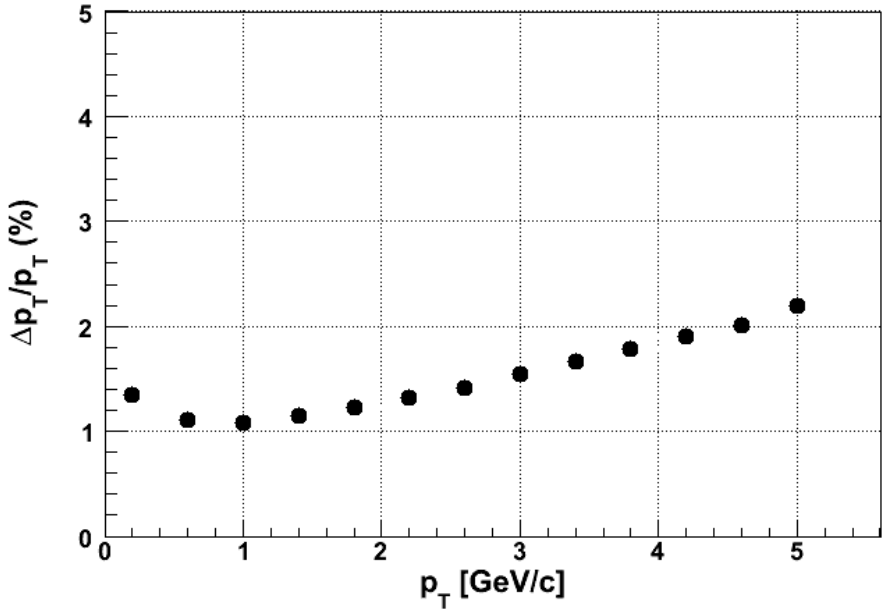

Figure 2.6: Transverse momentum relative resolution for electrons (J/ψ daughters) with at least 15 hits in TPC. Results were obtained for minimum-bias Cu+Cu events and with magnetic field 0.5 T.

in 120 modules of 40 towers each (20 in η, 2 in ϕ.). Each module covers one unit of η (0 to ± 1) and has azimuthal coverage of 2π/60. Each tower consists of 21 alternating layers of scintillator and lead absorber, corresponding to a total depth of approximately 20 radiation lengths ($20\ X_0$)[1].

The towers are projective in η, each of them is pointing back to the center of the interaction region. Each tower covers 0.05 in $\Delta\phi$ and 0.05 in $\Delta\eta$ which corresponds to tower size 10×10 cm at the radius of inner face. The energy resolution in the towers is $\frac{dE}{E} \sim \frac{16\%}{\sqrt{E}}$. The first 2 lead-scintillator layers compose the Pre Shower Detector (PSD). In order to provide a precise electromagnetic shower reconstruction, Shower Maximum Detector (SMD) is implemented at the position of $5X_0$ from the beamline. SMD is composed with two layers of gas wire pad chambers orthogonal in transverse dimension. This design allows to obtain two dimensional image (in η and ϕ direction) of the shower.

[1]High-energy electrons predominantly lose energy in matter by bremsstrahlung, and high-energy photons by e^+e^- pair production. Radiation length X_0 is the characteristic amount of matter traversed for these related interactions. It is both the mean distance over which a high-energy electron loses all but 1/e of its energy by bremsstrahlung, and 7/9 of the mean free path for pair production by a high-energy photon[1]

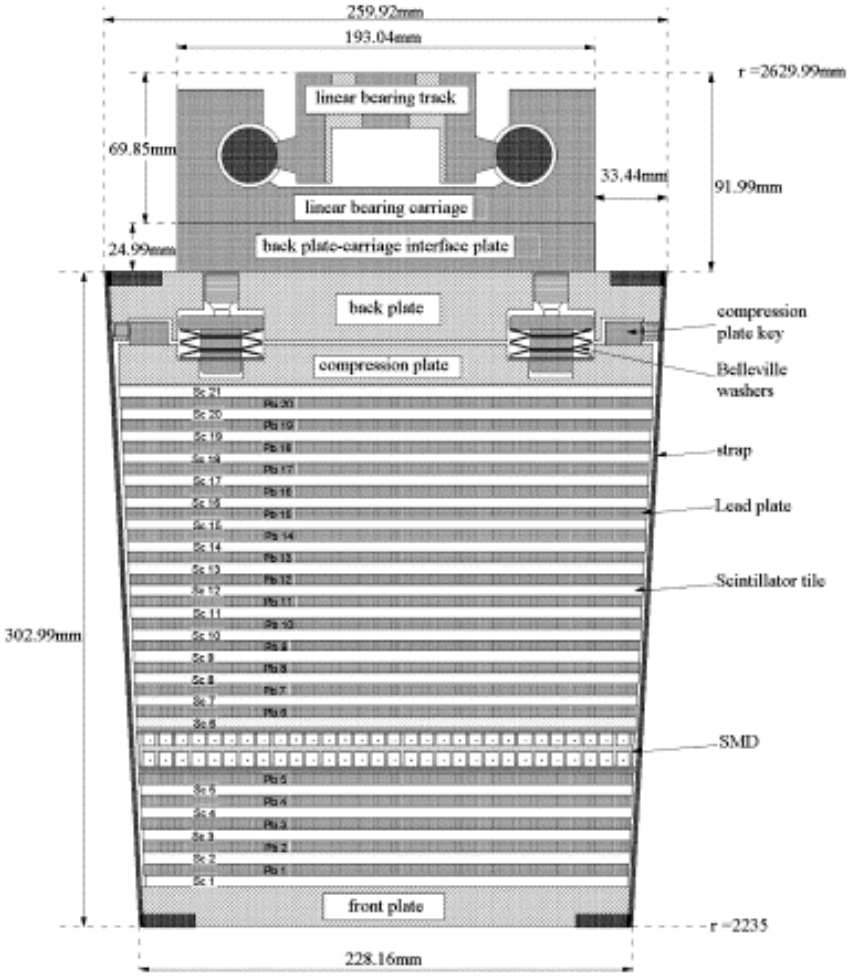

Figure 2.7: Side view of a STAR BEMC module. Figure taken from [84].

Figure 2.7 presents a BEMC module with shown location of Shower Maximum Detector.

2.4.1 Electron identification in BEMC

BEMC provides a few quantities which can be used in the electron selection [84]:

- Towers: p/E ratio
- Shower Maximum Detector: energy deposition, shower position and shape
- Pre-Shower Detector: energy deposition

For the typical p_T range of electrons from low-p_T J/ψ (1 to 1.7 GeV/c), the Shower Maximum Detector is not very effective as it introduces additional inefficiencies. The calibration of Pre-Shower Detector was not available when the studies were done. Therefore we used only

p/E information to identify electrons in our studies of J/ψ production, and the shower shape in SMD was used in auxiliary measurements for efficiency corrections presented in section 3.5.1. Both methods are briefly described in next section.

p/E

With the BEMC depth of 20 radiation lengths electrons are expected to deposit full energy in a tower. On the other hand, hadrons typically deposit far less than their total energy in a tower. Due to very small electron mass, its energy is approximately equal its momentum: $E \approx p$. Therefore a ratio of track momentum p measured in TPC and deposited energy E can be used to identify electrons and reject hadrons: for electrons $p/E \approx 1$ while for hadrons p/E on average is significantly grater than 1.

The effectiveness of p/E cut varies with momentum the resolution in TPC and the energy resolution in BEMC, therefore E/p improves with increasing energy until TPC resolution dominates at higher p_T. In the case of electrons which strike near edge of the tower, there is a high probability that energy leaks to adjacent tower. Such effect has to take into account by adjusting p/E cut or by using a clustering algorithm to recover missing energy. For the latter, one has to take into account that hadrons in high multiplicity events (like central Au+Au 200 GeV) may also contribute.

Shower Shape

At the depth of 5 radiation lengths where SMD is located, electromagnetic showers are excepted to be fully developed. Hadronic showers are typically incompletely developed at this depth. Therefore electromagnetic showers are broader than the hadronic ones and the number of SMD strips activated by hadrons is smaller than those activated by electrons. Consequently the number of hits in SMD can be used for hadron rejection.

2.5 Silicon Vertex Tracker and Silicon Strip Detector

The Silicon Strip Detector (SSD) [85] and Silicon Vertex Tracker (SVT) [86] are STAR silicon tracking detectors aimed at enhancement of the tracking capabilities by measuring accurately the two-dimensional hit position and energy loss of charged particles. Both detectors improves the primary vertexing, the two-track separation resolution and the energy-loss measurement for

particle identification.

The SVT consists of 216 Silicon Drift Detectors arranged in three layers around the beampipe at radii of approximately 6.9, 10.8, and 14.5 cm. The active silicon length in beam direction is 25 cm for the inner layer, 38 cm for the middle one and 44 cm for the outer layer. The total averaged radiation length of the SVT is a 2% of radiation length per layer.

The SSD provides the fourth layer of the inner tracking system. It is installed between the SVT and TPC and covers a pseudo-rapidity range of $|\eta| < 1.2$.

These detectors improves tracking in STAR, although they also introduced additional material close to the interaction point which leads to a higher electron background due to photon conversions and deteriorate mass resolution due to Bremsstrahlung.

2.6 Trigger detectors

Data analyses reported here used two different setups for minimum bias trigger. For Cu+Cu collisions, the trigger based on coincidence of signals in two Zero Degree Calorimeters (ZDC) while in Au+Au collisions additional information form two Vertex Position Detectors (VPD) were used. We also used Central Trigger Barrel (CTB) detector in studies of min-bias trigger efficiency in Au+Au. Main features of ZDC, VPD and CTB are briefly described below.

2.6.1 Vertex Position Detector

Two Vertex Position Detectors are located on both sides of the STAR detector, very close to the beam pipe, at the distance of 5.6 m from the center of STAR. Each of detectors consist of 19 Hamamatsu fine mesh dynode photomultiplier tubes [87]. VPD detectors provide the start time for time-of-flight measurement in new STAR Time-Of-Flight detector and also vertex position V_z. VPD were used together with minimum bias trigger to constrain V_z of collected events.

2.6.2 Zero Degree Calorimeter

The two Zero Degree Calorimeters[88] are located at the first bending magnets in the Collider line. These devices determine the number of spectator neutrons and they are used for beam monitoring, triggering (in minimum bias trigger), and locating interaction vertices. Each ZDC consists of 3 modules and each module consists of set of tungsten plates alternating with layers of wavelength shifting fibers routing cherenkov light to photomultiplier tubes.

2.6.3 Central Trigger Barrel

Central Trigger Barrel [88] is a detector made of 120 trays, each containing 2 scintillator slats. It is located between the TPC and the BEMC, with the same acceptance coverage as the latter. The CTB was originally developed to trigger events based on the detection of charged particles passing through it, although it was also used as a photon veto detector in J/ψ trigger for $p + p$ collisions [89].

Chapter 3

Data analysis

3.1 Data samples and trigger description

Studies presented here were performed using minimum-bias Cu+Cu and Au+Au collisions at $\sqrt{s_{NN}} = 200$ GeV. The Cu+Cu collisions were registered in 2005 while Au+Au data were collected in 2007.

The minimum-bias trigger in 2005 was based on a Zero Degree Calorimeters coincidence with on-line cut on vertex position from ZDCs: only events with the vertex Z position between $\pm$ 50 cm from the center of TPC were accepted. The V_z resolution from ZDC depends on event multiplicity and this leads to a multiplicity bias at the z values near the cut. An offline vertex z cut $|V_z| < 30$ cm was applied to remove the bias [90].

In the case of Au+Au data taken in 2007, the trigger was also built on ZDC coincidence, but with additional cut on event vertex V_z position from the Vertex Position Detectors, $|V_z| < 5$ cm. The online cut on V_z was in place to ensure that the vertex was well constrained into the acceptance of the Silicon Vertex Tracker and Silicon Strip Detector detectors, which were used in off-line track reconstruction. The online V_z cut introduced biases on the multiplicity distribution. The biases depend strongly on V_z of the event and therefore could not be easily removed by introducing an off-line V_z cut. The correction for the bias are described in section 3.2.2.

3.2 Event centrality selection

At STAR the centrality of the Cu+Cu and Au+Au collisions is determined using the uncorrected charge track multiplicity at mid-rapidity because it was possible to define multiplicity classes, corresponding to a fractions of the total inelastic hadronic cross–section, using Monte Carlo calculations [91, 92]. The number of participants N_{part} and number of binary collisions N_{bin} for a particular class can not be measured experimentally and they are obtained by mapping the measured multiplicity distribution to the corresponding distribution obtained from the Monte Carlo Glauber calculations for a given N_{bin} and N_{part} [91, 92, 90].

3.2.1 Cu+Cu collisions

The centrality classes for Cu+Cu were defined using the *reference multiplicity* (RefMult) - the uncorrected number of charged tracks in a pseudorapidity window of ± 0.5 and passing basic quality cuts (distance of closest approach to event vertex $<$ 3 cm, number of points in TPC $\geq$ 10). The centrality definition evolved over the years as the better understanding was obtained. The final set of selection criteria, corresponding to 0-60% of total hadronic cross–section, was established in 2008, while the previous cuts corresponded to 0-54% [90]. Some of our studies (like first approach to the cut optimization) were done using the old centrality definitions - such cases are explicitly marked.

3.2.2 Au+Au collisions

The tracks reconstruction for Au+Au data collected in 2007 was done using TPC together with inner tracker detectors: SSD and SVT. The inner trackers improved the momentum and pointing resolution although also introduced the bias of the V_z dependence of the tracking efficiency.

From practical point of view, a variable used to characterize the centrality of the collisions should be stable with the V_z and time. A set of tests was performed to establish the best quantity to define the centrality for this data set.

Three variables were studied:

1. reference multiplicity (**RefMult**)
2. global reference multiplicity (**gRefMult**) - the uncorrected number of global tracks within $|\eta| <$ 0.5 and number of TPC hits $\geq$ 10

3. Central Trigger Barrel (CTB) Multiplicity - sum of all hits on the CTB slats

It was shown in [93] that the minimum-bias distribution of the heavy ion collision multiplicity $Mult$ is well approximated by power-law form $Mult^{-3/4}$. Figure 3.1 shows an example of reference multiplicity distribution in minimum-bias Cu+Cu collisions. The power-law form describes the distribution over a broad range of event multiplicity and the low and high end points denote values at which the scaling breaks.

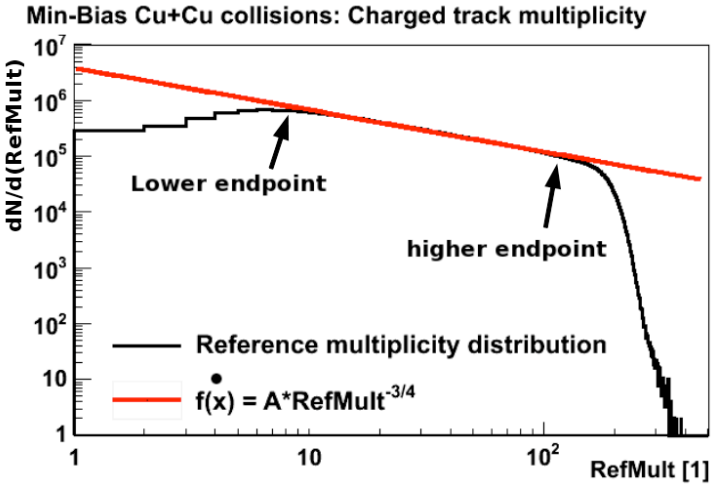

Figure 3.1: Reference multiplicity distribution in minimum-bias Cu+Cu collisions with power-law $A \times RefMult^{-3/4}$ fit (fit was done in $10 < RefMult < 110$). The power-law form describes the distribution over a broad range of event multiplicity, the low and high end points denote values at which power-law scaling breaks.

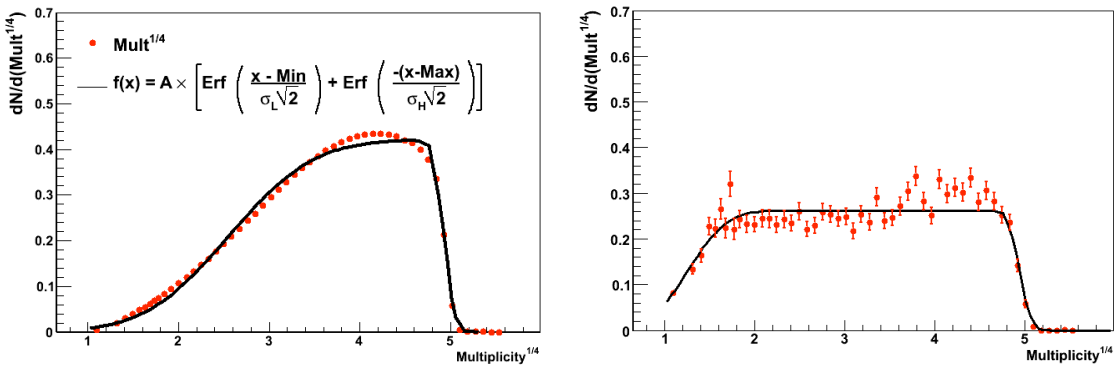

Figure 3.2: Example of a reference multiplicity distributions fitted by Fun. 3.2), used to examine the stability of the distribution, for $V_Z \simeq 0$ (left panel) and $V_Z \simeq -95$ cm (right panel).

There is a convenient consequence of the power-law scaling: if one converts charge track

multiplicity $Mult$ to $Mult^{1/4}$ then the distribution $dN/\left(Mult^{1/4}\right)$ versus $Mult^{1/4}$ is approximately constant for minimum bias collisions with two well defined end points [93, 94]. The examples of such distributions for Au+Au collisions are showed on Fig. 3.2. Due to simple form and well defined structure, $Mult^{1/4}$ is a convenient way to study trigger bias and efficiency as well as event centrality [93, 94].

Due to fluctuations of particle production in most central collisions, limited detector acceptance, finite resolution, inefficiencies and possible biases, the $dN/\left(Mult^{1/4}\right)$ distribution does not have a sharp drop at the end-points but the distribution is smeared. Assuming that the smearing at the endpoints is mostly due to Gaussian dispersion (due to detectors resolution), it can be described using the Gauss Error Function (Erf):

$$\text{Erf}(x) = \frac{2}{\pi}\int_{\infty}^{x} e^{-t^2}\text{d}t \tag{3.1}$$

In order to describe the $dN/\left(Mult^{1/4}\right)$ distribution, we constructed a function which is a sum of two ERFs (for lower and higher end points):

$$f(x) = A \times \left[\text{Erf}\left(\frac{x - Min}{\sigma_L\sqrt{2}}\right) + \text{Erf}\left(\frac{-(x - Max)}{\sigma_H\sqrt{2}}\right)\right] \tag{3.2}$$

where: x is $Mult^{1/4}$, A – amplitude, Min and Max – half max points of low and high multiplicity end points (points at which the value of f(x) is equal to half of its maximum value), σ_L and σ_H – describes the resolution of low and high ends of multiplicity distribution respectively.

Figure 3.2 shows examples of the global reference multiplicity distribution fitted by function 3.2. While $\sigma_L\sqrt{2}$ and $\sigma_H\sqrt{2}$ describe the turn-offs of the $dN/\left(Mult^{1/4}\right)$ distribution at the end points, the Min and Max describe the half-maximum of low and high end of measured RefMult and they are sensitive to the trigger inefficiency [94]. Consequently the half-max end points Min and Max can be used to study this effect.

The first step was to check if the trigger efficiency is stable vs time and V_z. The multiplicities (RefMult, gRefMult and CTB multiplicity) for a given variable (V_z, day, run number) were plotted in unity bins and then converted to Mult$^{1/4}$. The high-end half maximum points of RefMult show the dependence on the primary vertex position, e.i there is a V_z dependence of the reconstruction efficiency for RefMult. It is clearly visible for data with trigger without online V_z cut presented in Fig. 3.3. Such dependence is undesirable since it requires the centrality cuts to change as a function of V_z and it would make the analysis much more complicated. On the other hand the gRefMult is free of such effect therefore the centrality definition was constructed based on this quantity. All results of conducted tests can be found in [95].

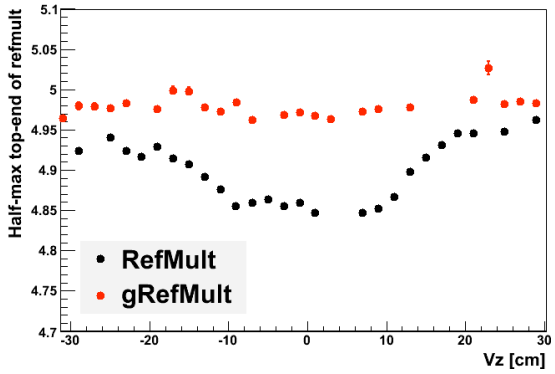

Figure 3.3: Track reconstruction efficiency (described by half–maximum top end point) vs V_z for RefMult and gRefMult for events with min-bias trigger without the on-line V_z cut (only results of successful fits are presented). The V_z dependence of track reconstruction efficiency for RefMult is clearly visible.

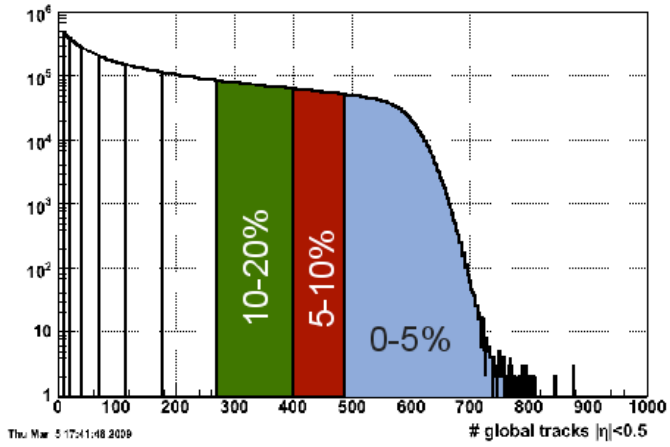

Figure 3.4: The gRefMult distribution for minimum-bias Au+Au events with centrality classes denoted.

Trigger bias correction

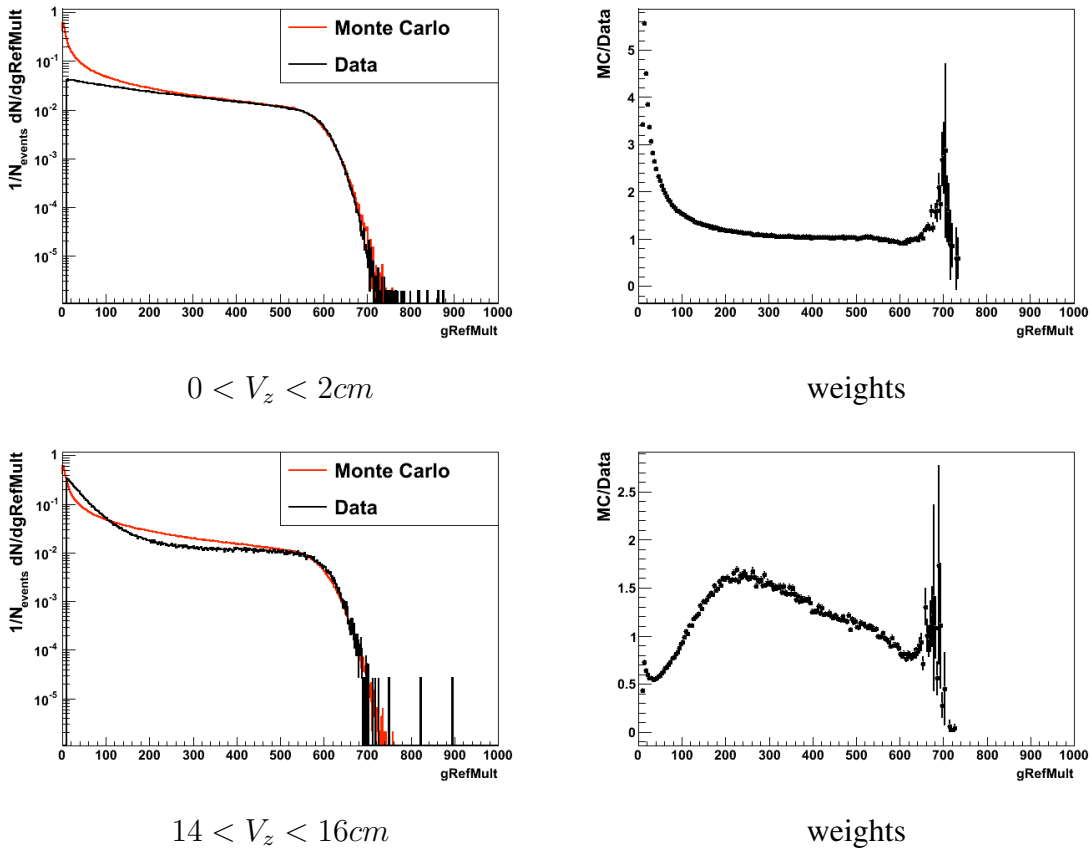

$0 < V_z < 2cm$ weights

$14 < V_z < 16cm$ weights

Figure 3.5: Left column: gRefMult distribution per event for the real data compared to Monte Carlo simulations for two V_z bins: 0–2 cm and 14–16 cm. For $0 < V_z < 2$ cm there is a deficit in peripheral events (low gRefMult) visible while in $14 < V_z < 16$ cm there is more peripheral events recorded than expected from simulations. Right: corresponding weights.

The second issue are biases on multiplicity distribution introduced by the on-line cut of $|V_z| < 5$ cm. There are two sources of this bias. Firstly, the VPD efficiency over full V_z range is higher for more central events compared to peripheral ones which leads to deficit in peripheral events for a given data sample. Secondly, the resolution of a V_z position from VPD is worse for peripheral events. Therefore at high $|Vz|$ there is larger population of the peripheral events while events at low V_z are more likely to be central. This effect is demonstrated on Fig. 3.5. The reference distribution was calculated in a framework of Monte Carlo Glauber calculation and provided by H. Masui [96].

The results were corrected for the aforementioned biases by event-wise weighing in 2 cm V_z bins. In each bin the real data and Monte Carlo gRefMult distributions were normalized in the

range of gRefMult > 500. Then weights were calculated as a ratio of Monte Carlo gRefMult to real data gRefMult. With the calculated weights, the unbiased distributions were restored by applying them to uncorrected data and the procedure is described in section 4.1.1.

3.2.3 Event selection and available statistics

For both Cu+Cu and Au+Au data sets, events with the primary vertex position z within ± 30 cm from the center of TPC were selected. In the case of Cu+Cu, events with RefMult corresponding to 0-60% most central events were selected. For Au+Au collisions, we studied 0-80% most central events chosen with the gRefMult cut.

After V_z and centrality selection, 26.7 million Cu+Cu and 64 million Au+Au minim-bias events were available for further analysis.

3.3 J/ψ reconstruction method

The main contributions to inclusive J/ψ production at RHIC are prompt J/ψ's (primordial J/ψ and feed-down from higher exited charmonium states ψ', χ_c, ..) and feed-down from B meson decays. J/ψ has a very short lifetime ($\tau = 7 \times 10^{-}21\ s$) [1] and prompt J/ψ's decay very close to the event vertex. B meson has much longer life time: $\tau = (0.46 \pm 0.07) \times 10^{-12}\ s$ [1] and in principle it can be reconstructed using displaced vertex if a very good track pointing resolution is achieved (for example, using a precise vertex detector). In analysis presented here it was not possible to separate prompt and B feed-down contribution therefore the inclusive J/ψ production is reported.

We studied J/ψ production via di-electron decay channel $J/\psi \to e^+e^-$ with the branching ratio $B_{e-e+} = (5.94 \pm 0.06)\%$. Di-muon decay channel has similar branching ratio $B_{\mu-\mu+} = (5.93 \pm 0.06)\%$, but for the analyzed data sets muons at STAR were not effectively separated from pions. The probability of J/ψ hadronic decays is very small [1] and the analysis of the charmonium production via hadronic channels is not feasible.

The analysis of leptonic channel has a significant advantage namely electrons do not interact strongly with hadronic matter, and therefore they are not distorted by hadronic re-scattering. Additionally, to a large extend, electrons can be separated from stable hadrons using the particle identification methods of TPC and BEMC. Therefore di-electron measurement is so far the best way to study J/ψ production at STAR.

J/ψ decays essentially at the primary event vertex and topological reconstruction is not possible. Consequently the statistical method has to be used. It includes pairing all selected electron candidates with selected positron candidates and calculating kinetic variables (invariant mass, p_T, rapidity) for all possible unlike sign combinations. In this approach it is not possible to distinguish electron-positron pairs from J/ψ decay from random combinations of electron and positron candidates produced in a given event. The random, uncorrelated e^+e^- pairs are called combinatorial background.

J/ψ signal is identified as a peak in di-electron mass spectrum, on the top of a large combinatorial background. To measure J/ψ cross-section, one has to evaluate and subtract the background:

$$S = N_{+-} - B \tag{3.3}$$

where: S – J/ψ signal, N_{+-} - number of all e^+e^- pairs and B is random combinatorial background.

It is extremely important to properly describe combinatorial background. There are a few commonly used methods to estimate this background:

1. Like-sign pairs[97] - the number of random combination N_{Bg} is estimated by a number of like-sign pairs (N_{++} and N_{--}) within each event. Either a sum ($N_{Bg} = N_{++} + N_{--}$) or a geometrical mean ($N_{Bg} = 2 \cdot \sqrt{N_{++} \cdot N_{--}}$) can be used. The geometrical mean is less sensitive to the fluctuations. The disadvantage of like-sign method is that the statistics is limited to the number of available events. On the other hand, it does not need additional normalization.

2. Event-mixing [98, 97] - the uncorrelated background is estimated by e^+e^- pairs in which electron and positron are taken from different events. This allows to increase the available statistics and to obtain a better statistical precision compared to the like-sign, since each event can be mixed with many others. Mixed events have to have similar properties (centrality, track multiplicity and primary vertex position) to avoid bias due to different efficiency and acceptance. The other issue is normalization of the invariant mass spectrum from event mixing. Experimentally it is obtained from the integration of the real data and event mixing spectra in the mass range where the signal is assumed to be negligible. However, if the shapes of real data and event mixing mass spectrum are different, then the systematic error due to choice of a normalization method occurs.

3. Rotation [99] - the momentum vector of one of the daughter particles is rotated to destroy any correlations. The disadvantage of this method is that it can introduce artificial correlations in studied events [99]. In our studies we use a single rotation by 180 degrees around the primary vertex.

After the combinatorial background subtraction, the invariant mass spectrum may still exhibit a correlated (or residual) background – in the case of J/ψ it is mostly $c\bar{c}$ continuum. If detected, it is usually estimated by polynomial functions fitted in the mass range where the signal is assumed to be negligible.

3.4 Signal significance

The strength of observed resonance signal in presence of a underlying background is quantified by signal *significance Sig*. It is defined as a ratio of measured signal yield S to statistical uncertainty of the signal ΔS:

$$Sig = \frac{S}{\Delta S} \tag{3.4}$$

The signal yield S is calculated by subtraction the background counts B from the total number of counts N:

$$S = N - B \tag{3.5}$$

Then assuming Gaussian error propagation, the statistical uncertainty ΔS is given by:

$$\Delta S = \sqrt{\left(\frac{\delta S}{\delta N}\Delta N\right)^2 + \left(\frac{\delta S}{\delta B}\Delta B\right)^2} = \sqrt{(\Delta N)^2 + (\Delta B)^2} \tag{3.6}$$

Since N = S+B then $\Delta N = \sqrt{S+B}$ and $\Delta B = \sqrt{B}$ for a bin counting statistics and

$$Sig = \frac{S}{\sqrt{S+2B}} \tag{3.7}$$

If the error on the background can be neglected, for example if a large sample of events from event-mixing is used to determine the background yield B, then Eq. 3.7 becomes

$$Sig = \frac{S}{\sqrt{S+B}} \tag{3.8}$$

Often the significance is referred to as a number of standard deviation σ.

3.4.1 Track selection

Track quality and kinematic cuts

J/ψ decays at the main event vertex therefore the primary tracks (tracks which have the position primary event vertex included as a first of the fit points) were used in the studies. We study a rear process, on top of a large combinatorial background and misidentified hadrons are large source of the background. Therefore we applied a set of track quality cuts to ensure sufficient momentum resolution and good particle identification.

Cu+Cu collisions

In 2005 only half of BEMC was installed and consequently only the TPC data were used in the particle identification. Therefore we required track to have at least 18 points in TPC at which the dE/dx was measured (so-called ***nDedxHits***). The dE/dx resolution is approximately proportional to $1/\sqrt{nDedxHits}$ and with $nDedxHits \geq 18$, the resolution on the level of 9% or better is achieved [100, 101]. We selected tracks within $|\eta| < 1$ and we applied the basic quality cut to ensure sufficient momentum resolution: long tracks (with number of hits in TPC $nHits \geq 25$ out of 45 possible) were selected. We required that track had more than 50% of possible points to avoid track splitting.

Au+Au collisions

In case of Au+Au data, the inner tracker detectors (SVT and SSD) were used in the tracking which improved resolution of the momentum and the DCA (Distance of Closes Approach to primary vertex). In addition, the BEMC was fully installed and provided an additional electron identification information. However, to use BEMC information, one has to extrapolate a track from TPC on BEMC to find a tower in which the electron deposited its energy. Therefore it became important that the track model (helix) describes a real particle trajectory very well. Consequently we required that a track has at least 25 points used in track fit (nFitPts) instead of simple hits in TPC. We also applied a cut to avoid track splitting: nFitPts had to be greater than 50% of possible points in TPC. We did not required minimum number of ***nDedxHits*** because BEMC provides additional handle on electron identification (p/E[1], see section 2.4), and without cut on ***nDedxHits*** better statistics was observed.

[1]For electron selection either p/E or E/p ratio can be used. E/p is sometimes preferred as it has a Gaussian distribution, although in our case a loose cut was used (p/E < 2, see Tab. 3.1) and both methods gave the same

Summary of used cuts

The cuts used in studies are shown in Tab. 3.1. The presented values of the kinematic cuts (p_T and DCA) were found to be optimal (based on signal and background behavior studies), and the cut evaluation is described section 3.7. The criteria used to identify and select electrons are described in the next section.

Table 3.1: List of cuts used in electron selection

Cu+Cu	**Au+Au**	**Comment**
primary tracks DCA < 1 cm	primary tracks DCA < 1 cm	Track originating in the vertex
$nHits \geq 25$ $nHits/nHitsMax > 0.55$ $nDedxHits \geq 18$ $\|\eta\| < 1$ $\|charge\| = 1$	$nFitPts \geq 25$ $nFitPts/nFitPtsMax > 0.55$ $\|\eta\| < 1$ $\|charge\| = 1$	Track quality assurance
$p_T >$ 1.1 GeV/c	$p_T >$ 1.2 GeV/c	Cut optimized to obtain the best signal significance
$\|n\sigma_e\| < 2$	$\|n\sigma_e\| < 2$ $p/E < 2$ 1/c E - single tower energy	Electron identification
$\|n\sigma_p\| > 2.5$ $\|n\sigma_K\| > 2$ ($n\sigma_\pi < -3$ or $n\sigma_\pi > 2.5$)	$\|n\sigma_p\| > 2$ $\|n\sigma_K\| > 2$ ($n\sigma_\pi < -3$ or $n\sigma_\pi > 2.5$)	Rejection of tracks likely to be hadrons

results.)

3.5 Particle identification

The ionization energy loss (dE/dx) measured in STAR TPC is expressed in $n\sigma_X$ units. $n\sigma_X$ describes the probability that a given track is identified as a expected particle X, i.e. electron or proton. For example, $n\sigma_e$ is defined as the ratio of dE/dx dE/dx and expected value of dE/dx for given particle type (electron) based on Bichsel function (B_e) and divided by the resolution of dE/dx, σ_e:

$$n\sigma_e = \frac{log[(dE/dx)/B_e]}{\sigma_e} \tag{3.9}$$

$n\sigma_p$, $n\sigma_\pi$ and $n\sigma_K$ are defined in similar way. Note, that in an ideal case $n\sigma_e$ for electrons (similarly $n\sigma_p$ for protons, $n\sigma_\pi$ for pions and $n\sigma_K$ for kaons) has a normal distribution (mean value is equal 0 and variance is 1).

In the case of low-p_T J/ψ's, most of the daughters have moderate p_T: 1–2 GeV/c. Figure 2.3 shows that the dE/dx bands for protons and electron cross each other at about $p_T = 1.2$ GeV/c. Consequently protons are the major source of contamination at moderate p_T. At high-p_T there is a relativistic rise and a pion dE/dx band overlaps partially with electrons. In order to reduce a combinatorial background due to hadron contamination, we had to remove pions and protons from the sample. Unfortunately dE/dx spectrum does not allow to separate electrons and hadrons in overlap regions and cuts to remove proton and pions cause also a significant loss in electron sample.

In our studies the cut on $n\sigma_e$ was used to accept electrons and cuts on $n\sigma_p$, $n\sigma_\pi$ and $n\sigma_K$ to reject dE/dx trajectories overlap between protons, pions, kaons and electrons. The particle identification (PID) cuts are summarized in Tab. 3.1. Rather stringent cuts on hadron (especially protons and pions) rejection in Cu+Cu collisions were found to be necessary because the hadron contamination increases significantly the combinatorial background. In the case of Au+Au, we used also information from BEMC. Each track passing TPC cuts were projected on BEMC and matched to a tower. We required that energy deposited in a given tower is $E > 0$ and the ratio of the energy and the electron momentum is $0 < p/E < 2$ 1/c. The distribution of p/E for minimum-bias data is shown in Fig. 3.6. Rather loose cut on p/E was used to take into account possible energy leaks to surrounding towers. The upper limit on p/E was derived from the assumption that electron should deposit at least half of its energy in a given tower (otherwise different tower would be better representation of its energy). With cut on p/E in place, the signal-to-background (S/B) ratio increased by factor 2 compared to the case when only TPC

was used in electron selection.

The additional p/E cut allowed us to use looser cut on the proton rejection in the TPC compare to Cu+Cu. However, we did not notice improvement in signal-to-background ratio when lest strict pion rejection criteria were applied together with p/E cut. It is caused by a large difference in the production rates: electron yield at high p_T is much smaller than pions: even with additional hadron suppression due to p/E cut, the number of pions is similar or even higher then with stringent cuts on $n\sigma_\pi$.

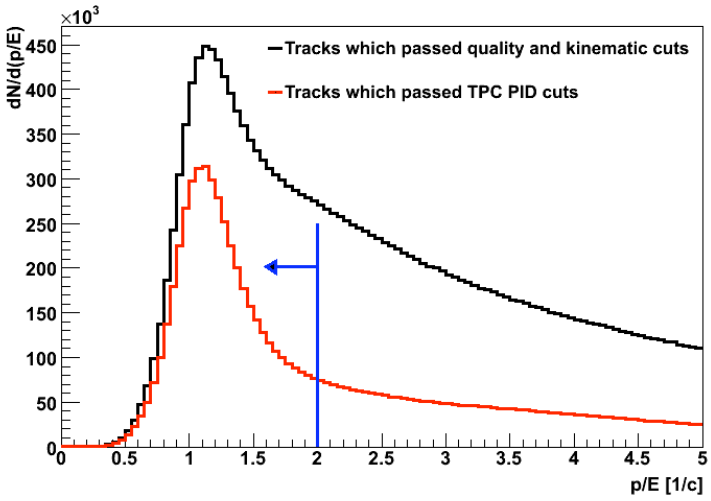

Figure 3.6: *p/E* distribution for all tracks passing quality and kinematic cuts (black histogram) and tracks passing TPC PID cuts for electron selection in Au+Au minimum-bias events. The blue line and the arrow denote the *p/E* cut used in the particle identification.

3.5.1 Electron identification efficiency

The ionization energy loss for tracks registered in STAR TPC is not well simulated (more details is presented in section 3.6.1), and therefore the real data have been used to estimate an electron identification efficiency.

It is important to note that tracks which passed PID cuts mostly consist of electron, although there is also some hadron contamination. Consequent, if N^{All} represents number of all tracks which passed PID cuts, N^{Sell_e} is number of electrons which passed PID cuts, and N^{Sell_H} is number of hadrons which were misidentified as electrons, then

$$N^{All} = N^{Sell_e} + N^{Sell_H} \tag{3.10}$$

The identification efficiency is calculated with respect to the number of all electrons which

passed the track quality and kinematic cuts, N^{All_e}. If N^{All_e} is known, then electron identification efficiency, $\epsilon_{PID}(p)$, for a particular momentum range $(p, p + \Delta p)$ is given by:

$$\epsilon_{PID}(p) = \frac{N^{Sell_e}(p)}{N^{All_e}(p)} \tag{3.11}$$

The purity of the electron sample can be quantify using following formula:

$$\text{Purity}(p) = \frac{N^{Sell_e}(p)}{N^{All}(p)} \tag{3.12}$$

If selected sample consists of electrons only, then Purity $= 1$, and if only hadrons passed PID cuts, then Purity $= 0$.

Both $N^{Sell_e}(p)$ and $N^{All_e}(p)$ are unknown, and are estimated using the real data and a procedure described in next section.

Electron yield estimation

The first step in the efficiency calculation is to establish the initial number of electron N^{All_e} in the sample, which passed track quality and kinematic cuts. It is convenient to use $n\sigma_e$ distribution for this purpose, because the $n\sigma_e$ distribution for electrons has a Gaussian shape, and $n\sigma_e$ for hadrons can be approximated by Gaussian distributions in a given, small momentum range [101]. Therefore, we can approximate the $n\sigma_e$ distribution for all tracks in a given small momentum bin by the sum of Gauss functions for different particle species. Each of them is characterized by three parameters: mean value μ, amplitude *A* and standard deviation σ:

$$f(n\sigma_e) = A_e \times e^{-\frac{(n\sigma_e-\mu_e)^2}{2\sigma_e^2}} + A_p \times e^{-\frac{(n\sigma_e-\mu_p)^2}{2\sigma_p^2}} + A_\pi \times e^{-\frac{(n\sigma_e-\mu_\pi)^2}{2\sigma_\pi^2}} + A_D \times e^{-\frac{(n\sigma_e-\mu_D)^2}{2\sigma_D^2}} \tag{3.13}$$

where: μ_e μ_p μ_π and μ_D are mean values of $n\sigma_e$ distribution for electrons, protons, pions and deuterons respectively, σ_e σ_p σ_π and σ_D are standard deviations of $n\sigma_e$ distribution for electrons, protons, pions and deuterons, and A_e A_p A_π and A_D are amplitudes of these distributions.

This function is fitted to $n\sigma_e$ distribution for all tracks which passed quality and kinematic cuts. Fit is done in a narrow momentum slice and integral of each Gaussian gives a total yield for a given particle type.

The multi-parameter fit (9 if electron, pion and proton are included, and 12 parameters in a range $1.5 < p < 2$ GeV/c where deuterons are also taken into account) is a technical challenge

in case when signals are not well separated. Such situation emerges for tracks with moderate and high momentum (see the overlap of proton and electron or pion and electron *dE/dx* bands in Fig. 2.3). To improve the results of the fit, one needs to use additional information to constrain the fits.

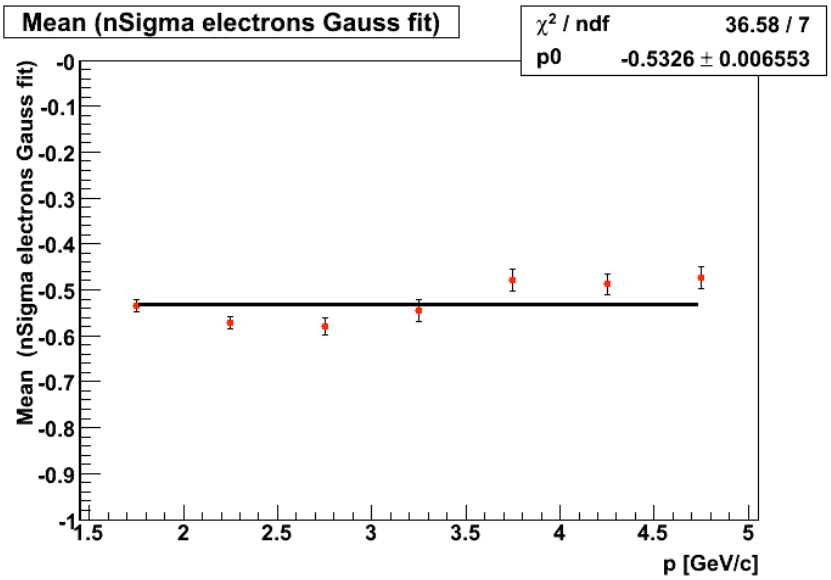

Figure 3.7: Mean of $n\sigma_e$ distribution for electrons as a function of track momentum for Cu+Cu min-bias events. The black line represents a linear fit.

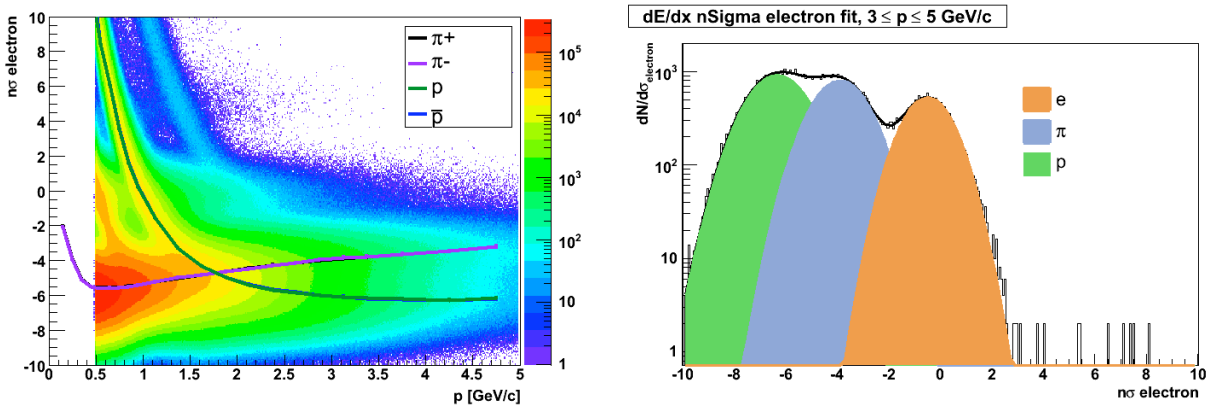

Figure 3.8: Left: $n\sigma_e$ distribution for all tracks passing quality cuts in 0-54% Cu+Cu minimum-bias collisions. The lines represent the expected mean values of $n\sigma_e$ for protons and pions. Right: example of $n\sigma_e$ distributions for minimum-bias Cu+Cu collisions, where hadron contamination was suppressed using additional cuts on information from BEMC and BSMD.

Constraints for electrons

Variable $n\sigma_X$ (X = pions, protons, kaons or electrons) are defined using Bichsel function. These

functions are good approximation for the *dE/dx* curves in a TPC and it is a standard method of predicting the *dE/d*x value for charged hadrons in all momentum ranges. However gas multiplication gains, noise of TPC electronics and pileup[2] in high luminosity environment cause deviation of *dE/dx* from the Bichsel function [101]. Consequently $n\sigma_X$ associated with a given particle type can be underestimated [101].

We observe such effect as a shift of the mean value of $n\sigma_e$ distribution towards negative values. The shift depends on the event multiplicity and it is stronger for higher multiplicity events. To quantify the effect, we selected a track sample in which hadrons were suppressed – this improved hadron and electron separation. To suppress hadrons we used BEMC together with SMD detector. BEMC were not used in J/ψ reconstruction in Cu+Cu because of its limited coverage in 2005 which leaded to significant J/ψ reconstruction efficiency loss, but we found it useful for single electron studies. Similar conclusions were drawn for SMD – due to its low efficiency it was not useful for J/ψ analysis but it helped to further suppress hadrons in auxiliary studies.

The BEMC and SMD are most effective for the high-momentum particles, therefore the cut of $p_T > 2$ GeV/c was used together with cut on p/E ratio ($p/E < 2.0$ 1/c) and the size of electromagnetic shower in SMD (number of activated strips in each of η and ϕ direction ≥ 2). SMD provides additional discrimination power for electron – hadron separation. Figure 3.8 (right panel) shows that the $n\sigma_e$ distributions for protons, pions and electrons are well isolated. We fitted this sample by $f(n\sigma_e)$ (Eq. 3.13) in a small momentum slices, and extracted μ_e as a function of track momentum. The example of μ_e distribution vs track momentum for minimum-bias Cu+Cu events is shown in Fig. 3.7.

Table 3.2: Mean value μ_e of the electron $n\sigma_e$ distribution in Cu+Cu collisions with different centrality

Centrality	μ_e
0-60%	-0.533 $\pm$ 0.006
0-20%	-0.568 $\pm$ 0.009
20-40%	-0.486 $\pm$ 0.011
40-60%	-0.456 $\pm$ 0.017

In the kinematic range of our interest i.e. $p_T > 1$ GeV/c, we do not expect a significant

[2]Pileup occurs if tracks from event from previous/later collisions are recored together with the analyzed even.

Table 3.3: Mean value μ_e of the electron $n\sigma_e$ distribution in Au+Au collisions with different centrality

Centrality	μ_e
0-80%	-0.39 $\pm$ 0.02
0-10%	-0.5 $\pm$ 0.02
10-20%	-0.35 $\pm$ 0.01
20-40%	-0.21 $\pm$ 0.01
40-80%	-0.04 $\pm$ 0.01

change of $\mu_e(p)$ with electron momentum, therefore the μ_e from fits in different momentum slices were approximated by function $\mu_e(p) = const$, and an example of such fit is shown in Fig. 3.7.

The results of such approximation for different centrality classes of Cu+Cu and Au+Au events are shownß in Tab. 3.2 and Tab. 3.3. In Cu+Cu collisions there is a slight dependence on event centrality (up to 15%). Since the available statistics is limited, for the purpose of these studies the integrated value (for minimum-bias events) was used in the final efficiency calculation in case of Cu+Cu collisions. On the other hand, the μ_e shift in Au+Au collisions is significant and increases with the event centrality.

Constraints for hadrons

To constrain μ_p and μ_π, we used pion and proton samples from the topological analysis of resonances decays ($\Lambda,\ K^0_s$):

$$\Lambda \to p + \pi^- \ (\overline{\Lambda} \to \overline{p} + \pi^+),\ K^0_S \to \pi^+ + \pi^- \tag{3.14}$$

.

This method is described in details in [101]. Pion and protons from the topological analysis of the Λ and K^0_s decays gave samples with very high purity. Then for each particle type we fitted $n\sigma_e$ distribution by Gaussian functions in narrow momentum slices and we obtained the μ_p and μ_π as a function of momentum. This was done separately for positive and negative tracks. Figure 3.8 shows these μ_p and μ_{pi} values plotted on top on $n\sigma_e$ distribution for all charged tracks in Cu+Cu minimum-bias events. The pions, proton and kaon bands are visible in the data and μ_p and μ_π curves lie on top of the proton and pion bands. Note, that the results of independent analyses for positive and negative hadrons agree very well.

The constrains for μ_e, μ_p and μ_π were obtained with a set of assumptions (Gaussian shape of the $n\sigma_e$ distribution for hadrons, $\mu_e(p) = const$) and results of the final fit may depend slightly on those restriction. Therefore, we did not fix completely μ_e, μ_p and μ_π but we used the obtained constraints as guidance in minimalization procedure. The parameters μ_e μ_p and μ_π in Eq. 3.13 were initialized by values obtained in aforementioned studies. While μ and σ of hadrons were free parameters in a fit, we allowed $\pm 10\%$ variation of μ_e. We also applied constraints to σ_e: in ideal case $\sigma_e = 1$, therefore we were varying the σ_e in a range 0.9 to 1.1. We used χ^2 method to control fit quality. The best results in terms of χ^2/ndf were obtained for $\sigma_e = 0.9$, it was also observed that fit with $\sigma_e = 1.05$ and 1.1 missed the data.

With the successful fit and obtained A_e, μ_e and σ_e, the overall electron yield in a particular momentum bin is given by the integral of the Gaussian function for electron in $f(n\sigma_e)$ (Eq. 3.13), namely:

$$N^{All_e} = \int \left(A_e \times e^{-\frac{(n\sigma_e - \mu_e)^2}{2\sigma_e^2}} \right) d(n\sigma_e) \tag{3.15}$$

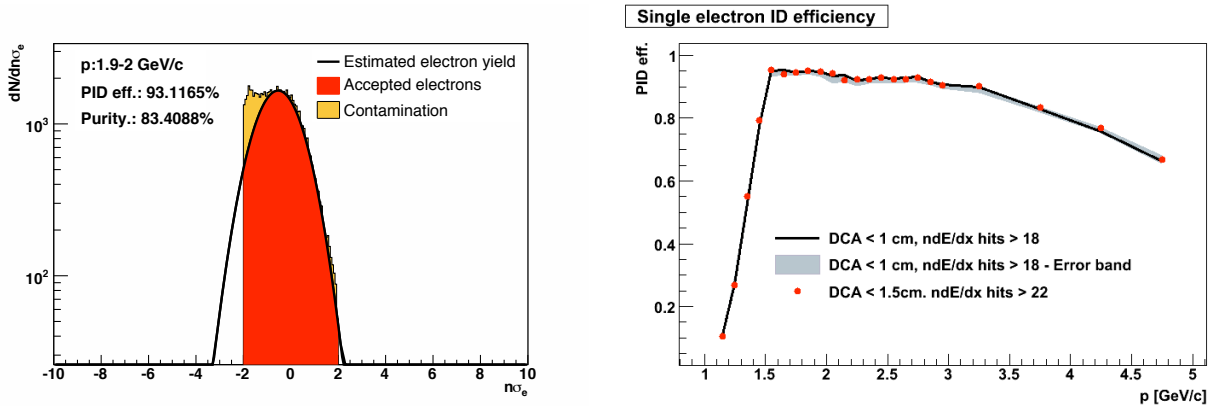

Figure 3.9: Left: $n\sigma_e$ distribution for accepted tracks compared to expected electron yield for $1.9 < p < 2$ GeV/c. Right: Single electron identification efficiency for different DCA and nDedxHits cuts.

Single electron identification efficiency and purity

The sample of tracks selected for J/ψ reconstruction includes a small hadron contamination. To estimate the real number of electrons passing particle identification cuts (N^{Sell_e}) in a given momentum range, we employed following procedure:

1. Using method described in previous paragraphs, we obtained a $n\sigma_e$ distribution for electrons passing quality and kinematic cuts (before PID):

$$N^{All_E}(n\sigma_e) = A_e \times e^{-\frac{(n\sigma_e-\mu_e)^2}{2\sigma_e^2}} \tag{3.16}$$

   This distribution is represented by the black Gaussian function in Fig. 3.9 (left panel).

2. The $n\sigma_e$ distribution for tracks passing quality, kinematic and PID cuts is taken from the data: $N^{All}(n\sigma_e)$
   This distribution is represented by the histogram in Fig. 3.9 (left panel), which has two contributions: electrons (red area) and hadron contamination (yellow area).

3. We compared $N^{All}(n\sigma_e)$ with $N^{All_e}(n\sigma_e)$ for each $n\sigma_e$ bin

4. If $N^{All}(n\sigma_e) \leq N^{All_e}(n\sigma_e)$ then $N^{Sel_e} = N^{All}(n\sigma_e)$

5. If $N^{All}(n\sigma_e) > N^{All_e}(n\sigma_e)$ then $N^{Sell_e} = N^{All_e}(n\sigma_e)$
   (100% PID efficiency is assumed in such case, everything above $N^{All_E}(n\sigma_e)$ is take as contamination. This approach is illustrated by Fig. 3.9.)

Finally the N^{Sell_e} is given by the sum of $N^{Sell_e}(n\sigma_e)$ over the overall $n\sigma_e$ range. Then the $\epsilon_{PID}(p)$ and purity are given by Eq. 3.11 and Eq. 3.12.

Figure 3.9 provides also a graphical illustration to these calculations. The single electron identification efficiency is the ratio of the number of selected electrons (the red area of the histogram in Fig. 3.9) and the integral of $N^{All_E}(n\sigma_e)$ (the black Gaussian function). Purity is given by the ratio of selected electrons (the red histogram) to all accepted tracks (the sum of red and yellow areas). Note, that purity is strongly correlated with ϵ_{PID} and purity may be overestimated in case low ϵ_{PID}.

Uncertainties estimations

There are two types of uncertainty in this method:

- statistical error on μ_e , μ_p , μ_π, μ_D, σ_e, σ_p, σ_π, σ_D, A_e, A_p, A_π, A_D parameters from the fit
- systematic errors due to constrains applied in fits

The first type of uncertainty was estimated by varying parameters in Eg. 3.16 by one standard deviations. The systematic error was estimated by varying the constraints on σ_e and μ_e. In both cases the error was defined as a maximum deviation from the results obtained with the default set of parameters. The total uncertainty is the quadratic sum of statistical and systematic error and gives the upper and lower limits on ϵ_{PID}.

Results and summary

The final results for Cu+Cu are presented on the Fig. 3.10. The PID efficiency depends strongly on momentum. The region of low $\epsilon_{PID}(p)$ around 1 – 1.5 GeV/c is caused by the cuts used to remove protons from the sample, it is followed by a plateau up to 3.5 GeV/c and then the $\epsilon_{PID}(p)$ decreases due to relativistic rise of pions. It was also found that the PID efficiency is independent of DCA and nDedxHits cuts, which is presented in Fig. 3.9

For Au+Au collision, we calculated the $\epsilon_{PID}(p)$ for minimum-bias events and also separately in each narrow centrality classes (0-10%, 10-20%, 20-40% and 40-80%) and the results are showed in Fig. 3.10). It is seen that $\epsilon_{PID}(p)$ depends on event centrality. Due to limited statistics available, it was unpractical to estimate the J/ψ signal in each narrow centrality class because the statistical fluctuations are much higher in such case. Moreover, we used a shape

of J/ψ mass spectrum from Monte Carlo simulations to extract the signal yield, and there was not enough signal counts to perform a successful fit in each of centrality classes. Therefore it was preferable to use a wider centrality bins. To assess an effect of $\epsilon_{PID}(p)$ dependence on event centrality, we calculate a signal yield in narrow centrality classes, applied all corrections and then merged the results. The results were consistent with those using average $\epsilon_{PID}(p)$ for min-bias events (0-80%). Consequently we used an average $\epsilon_{PID}(p)$ to obtain the final J/ψ p_T spectrum for min-bias events.

The results of single electron efficiency assessment were included in the calculation of J/ψ reconstruction efficiency, which is described in Sec. 4.2.

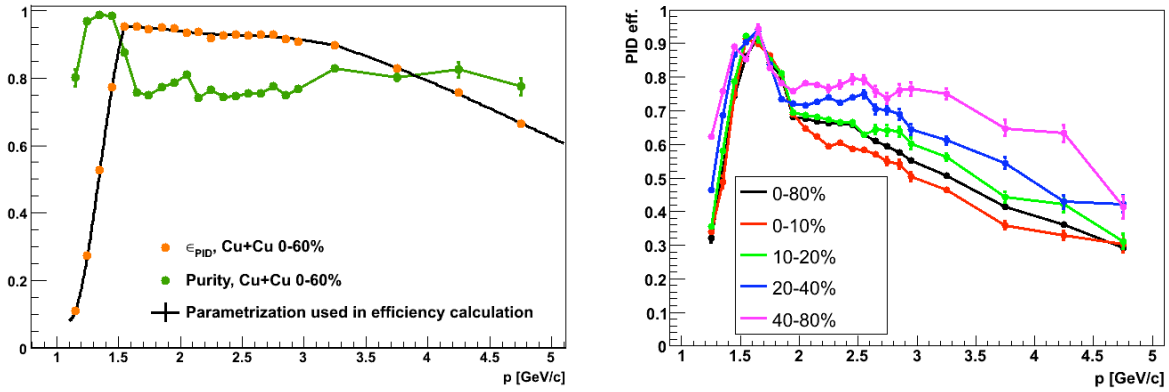

Figure 3.10: Left: Electron $\epsilon_{PID}(p)$ and purity in min-bias Cu+Cu collisions. Right: Electron $\epsilon_{PID}(p)$ in different centrality classes of Au+Au collisions.

3.6 Monte Carlo studies

3.6.1 Monte Carlo simulations and efficiency corrections

Monte Carlo simulations and technique called *embedding* were used to estimate corrections for the limited detector acceptance, efficiency losses and possible biases. This procedure is illustrated in Fig. 3.11 and consists of the following steps:

1. First, the input data have to be provided, which consist of:
   - Monte Carlo simulations of the process of interest ($J/\psi \to e^+e^-$ in our case)
   - real data events, which should have the same characteristics as the whole data set (same V_z and multiplicity distribution and same event centrality)
2. e^+e^- from J/ψ decay are propagated through the STAR detector modeled using GEANT [102] software package. The simulations are based on a detailed model of all material in interaction region, e.g. TPC gas, SVT and SSD detectors, support structure, beam pipe. GEANT simulates particle interactions with the material (multiple Coulomb scattering, energy loss and γ conversion)
3. The output of GEANT simulations is next used by the TPC Response Simulator (TRS) [103] to calculate the response of the TPC detector to the particles traversing TPC and ionizing gas in its volume. This procedure produces TPC hits.
4. The TPC response to J/ψ daughters is embedded in the real data events.
5. A standard reconstruction chain is used to reconstruct these data.
   Such mixing of Monte Carlo and real data allows to estimate the tracking efficiency in the realistic environment, i.e. with realistic TPC hits density, different background sources (e.g. cosmic ray, "pile–up" events) and electronic noises taken into account. The output of this procedure consists of reconstructed tracks.
6. The Monte Carlo tracks are associated to the reconstructed tracks based on criteria of maximum number of common TPC hits of the Monte Carlo and reconstructed track. At least 10 common points are required for the association.

After this step, the full information about simulated and reconstructed electron tracks is available, and the reconstruction efficiency and acceptance $\epsilon_{A \times R}$ for a given rapidity and p_T bin can be calculated using following formula:

$$\epsilon_{A \times R} = \frac{N^{J/\psi}_{Reconstructed}}{N^{J/\psi}_{Monte\ Carlo}} \tag{3.17}$$

where: $N^{J/\psi}_{Monte\ Carlo}$ - number of simulated J/ψ, $N^{J/\psi}_{Reconstructed}$ - number of reconstructed J/ψ with the same set of kinematic cuts as used for the analysis of the real data.

3.6.2 Reconstruction efficiency vs dE/dx

Simulations of a ionization energy loss (dE/dx) is a very complicated process. STAR TPC Response Simulator is able to reproduce only approximately the dE/dx vs track momentum for different particle species. It does not reproduce the overall magnitude of dE/dx. Therefore the magnitude is adjusted using the real data i.e. by changing the scaling factor to match the dE/dx of measurement. The reconstruction efficiency may depend on the dE/dx values because the pedestal cutoff in TPC (applied to eliminate noise) is close to the dE/dx of Minimum Ionization Particle (MIP). Therefore if the gain is low, one loses some TPC hits. To obtain the simulations of dE/dx close to the data, we use an iterative process of producing small samples of simulations and adjusting the normalization. Moreover, the process of adjusting the magnitude of dE/dx (the mean value) to match the real data results in deterioration of the agreement of width of distributions (Fig. 3.12). Therefore the dE/dx in embedding should not be used to estimate the electron identification efficiency. Additionally, there may be a systematic effect due to difference in distribution width which will be quantified.

In a process of adjusting dE/dx scaling factor in $D^0 \rightarrow K^-; +\pi^+$ in Au+Au at $\sqrt{S_{NN}} = 200$ GeV (RHIC run 7) simulations, two samples with different normalization factors were used: 1.05 and 1.3. Simulations of electrons with different dE/dx normalization were not available therefore we used the pion and kaon sample to estimate what is the effect of 25% difference in overall dE/dx scale on the reconstruction efficiency. We calculated the efficiency with $|Vz| < 3$ cm for various centrality bins. We used primary tracks within standard TPC acceptance ($|\eta| < 1$, $p_T > 0.2$ GeV/c) and with three different track quality cuts: $nFitPts > 15$, $nFitPts > 20$ and $nFitPts > 25$. The efficiency distribution vs. p_T for the normalization factor = 1.05 and 1.3 for min-bias events (0-80% most central events) and their ratio is presented in Fig. 3.13.

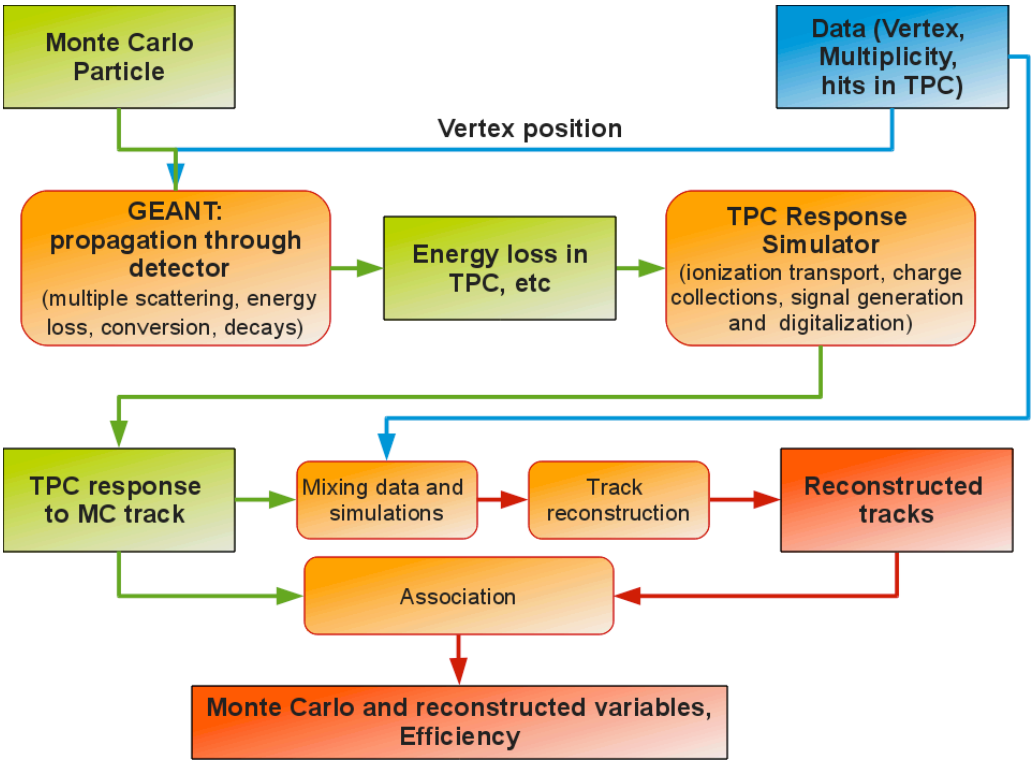

Figure 3.11: A schematic view of data processing in embedding, the details are described in the text.

The average ratio was estimated by straight line fit and the results are shown in Tab. 3.4.

It was found that within given statistics the average difference is small. It is less than 1% for π^+ with cut on $nFitPts > 15$, and $nFitPts > 20$, while there is a 2% - 3.5% difference for $nFitPts > 20$. There difference in case of K– is less than 1% for all tested nFitPts cuts. Results are similar for different centrality classes (0-10%, 10-20%, 20-40% and 40-80%). The dE/dx values for electrons with the kinematic cuts used in our studies ($p_T > 1.1$ GeV/c) are always higher than those for kaons, therefore the systematic error due to dE/dx scaling factor is smaller than in the case of kaons, and it is negligible.

Table 3.4: Ratio of the efficiency for normalization factor (NF) = 1.05 and 1.3 for selected centrality bins

	π^+	K^-
0-10%		
Track quality cut	$eff_{NF=1.3}/eff_{NF=1.05}$	$eff_{NF=1.3}/eff_{NF=1.05}$
$nFitPts > 15$	1.00 ± 0.00	1.00 ± 0.01
$nFitPts > 20$	1.01 ± 0.01	1.00 ± 0.01
$nFitPts > 25$	1.02 ± 0.01	1.00 ± 0.01
10-20%		
Track quality cut	$eff_{NF=1.3}/eff_{NF=1.05}$	$eff_{NF=1.3}/eff_{NF=1.05}$
$nFitPts > 15$	1.00 ± 0.00	1.00 ± 0.01
$nFitPts > 20$	1.01 ± 0.01	1.00 ± 0.01
$nFitPts > 25$	1.04 ± 0.01	1.01 ± 0.01
20-40%		
Track quality cut	$eff_{NF=1.3}/eff_{NF=1.05}$	$eff_{NF=1.3}/eff_{NF=1.05}$
$nFitPts > 15$	1.00 ± 0.00	0.99 ± 0.01
$nFitPts > 20$	0.99 ± 0.01	1.00 ± 0.01
$nFitPts > 25$	1.01 ± 0.01	1.00 ± 0.01
40-80%		
Track quality cut	$eff_{NF=1.3}/eff_{NF=1.05}$	$eff_{NF=1.3}/eff_{NF=1.05}$
$nFitPts > 15$	1.00 ± 0.00	0.99 ± 0.01
$nFitPts > 20$	1.01 ± 0.01	0.99 ± 0.01
$nFitPts > 25$	1.02 ± 0.01	1.00 ± 0.01

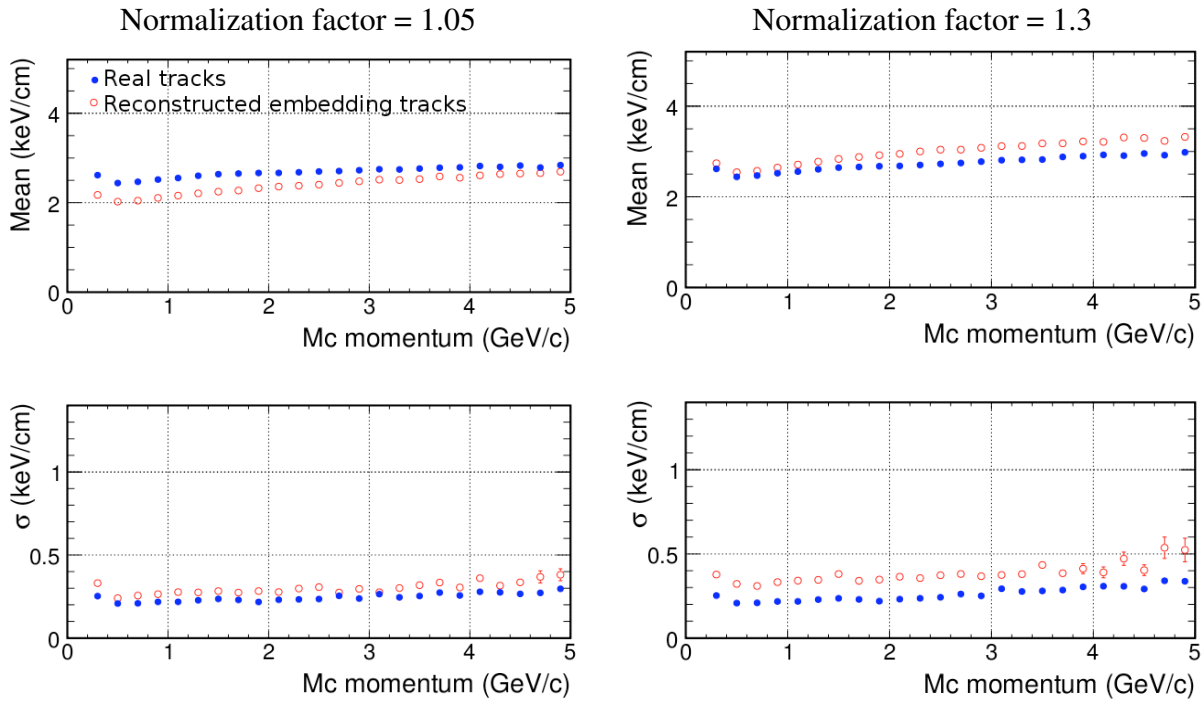

Figure 3.12: The mean and σ of dE/dx distribution for $\pi+$ in simulations and in real data for normalization factor = 1.05 (left) and 1.3 (right). The correlation between these parameters is clearly visible - the increase of the mean due to higher normalization factor causes the increase of width of the distribution. Pions in real data were selected with $|n\sigma_{\pi}| < 2$ cut.

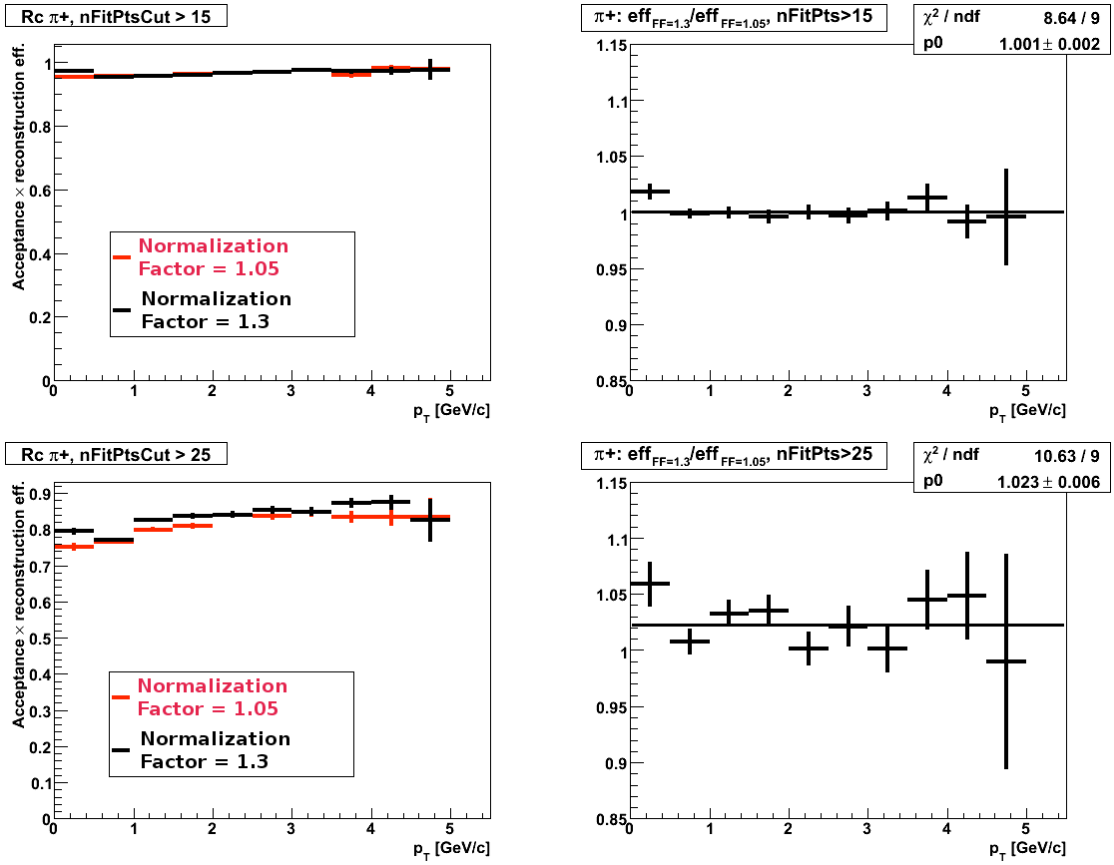

Figure 3.13: Left: Acceptance $\times$ reconstruction efficiency for $\pi+$ for normalization factor = 1.05 and 1.3 for $nFitPts > 15$ (upper panel) and $nFitPts > 25$ (lower panel) in min-bias Au+Au collisions. Right: ratio of efficiencies as a function of p_T with a straight line fit used to estimate the average.

3.7 Cut optimization

In case of small signal on top of large background, the right choice of cuts can reduce background and maximize the signal i.e. one can improve precision of the measurement. On the other hand, the small signals have the large statistical fluctuations and one should not use only real data to establish the best cuts as one might tune them to fluctuations. Therefore simulations need to be used in such analysis. In next sections I will describe our studies aimed to find optimal and unbiased electron selection criteria.

3.7.1 Strategy

We chose maximization of signal significance as an optimization criteria in cut study. The significance is given by:

$$Sig = \frac{S}{\sqrt{S+B}} \tag{3.18}$$

where: Sig - J/ψ signal significance, S - J/ψ yield and B - background yield.

Significance is directly related to the relative error $\left(\frac{\Delta S}{S} = \frac{1}{Sig}\right)$ therefore the better significance, the more precise measurement can be achieved.

Optimization of the selection criteria requires reliable background and signal model. The first one is relatively easy to construct, one can use:

- number of e^+e^- pairs in the small data sample
  J/ψ cross-section is very small in $p+p$ collisions at 200 GeV ($\simeq$ 1 J/ψ per million events) and J/ψ yield is negligible in small data sample while all other correlation in a background are preserved. Therefore one can study correlated and combinatorial background in the same time, although the statistics is limited.

- event mixing

- like-sign or rotational background

The signal model is much more difficult to build as we have to mock up most important features of the signal measured in the experiment. We used Monte Carlo simulations for this purpose with additional corrections for effects which are not well simulated (like particle identification in TPC).

The general approach in cut optimization is to maximize the background rejection for a given signal efficiency and scan the full range of the latter quantity. Signal efficiency ϵ_S is given by:

$$\epsilon_S = \frac{N^{surv}_{J/\psi}}{N^{Init}_{J/\psi}} \tag{3.19}$$

where: $N^{Init}_{J/\psi}$ is initial number of J/ψ mesons in the signal model and $N^{surv}_{J/\psi}$ is number of J/ψ surviving kinematic and PID cuts.

So far there is no reliable Monte Carlo simulations for the dE/dx in TPC, therefore the real data have to be used in particle identification assessment. We incorporated PID efficiency in $N^{surv}_{J/\psi}$ evaluation using formula:

$$N^{surv}_{J/\psi} = N^{kin.cuts}_{J/\psi} \cdot \epsilon_{PID}(p^{e+}) \cdot \epsilon_{PID}(p^{e-}) \tag{3.20}$$

where: $N^{kin.cuts}_{J/\psi}$ - number of J/ψ's surviving kinematic cuts, $\epsilon_{PID}(p^e)$ - single electron identification efficiency for a given momentum p. The electron identification efficiency was estimated using procedure described in section 3.5.

Background efficiency ϵ_B is given by:

$$\epsilon_B = \frac{N^{surv}_{B}}{N^{Init}_{B}} \tag{3.21}$$

where: N^{Init}_{B} is initial number of background pairs and N^{surv}_{B} is number of background pairs surviving kinematic and PID cuts.

An Analysis in which a significance is maximized requires knowledge of expected signal, N_S, and background,N_B, yields for a given set of cuts used as starting point in studies, i.e. absolute normalization is necessary. Then the signal significance can be calculated using:

$$Sig = \frac{N_S \epsilon_S}{\sqrt{N_S \epsilon_S + N_B \epsilon_B}} \tag{3.22}$$

The statistical uncertainty on the significance was estimated using error propagation formula:

$$\Delta Sig = |\frac{\delta Sig}{\delta S}|\Delta S + |\frac{\delta Sig}{\delta B}|\Delta B \tag{3.23}$$

Where: $\Delta S = \sqrt{N_S \epsilon_S}$ and $\Delta B = \sqrt{B_S \epsilon_B}$.

It is natural to start optimization with set of loose cuts to have as much signal as possible in the initial sample. For relaxed selection criteria the normalization for background can be easily obtained with satisfactory precision using like-sign method. However, J/ψ peak in such case sits on top of large combinational background and J/ψ yield can be extracted only with

$20 - 30\%$ precision for data analyzed here. This normalization error is the main systematic uncertainty of these studies. The second source of systematic error is PID efficiency ϵ_{PID} - it was calculated for a given initial set of kinematic and PID cuts and then used as a electron selection probability with assumption that ϵ_{PID} does not change significantly for different set of kinematic cuts. Although ϵ_{PID} may change slightly with p_T cut, the ϵ_{PID} assessment is a very complicated process and it was not feasible to calculate ϵ_{PID} for every p_T cut examined in the studies.

3.7.2 Cut optimization for Cu+Cu collisions using Pythia

The first approach to find the optimal electron selection criteria was done for Cu+Cu collisions. We used Pythia [104], a widely accepted Monte Carlo event generator, to simulate J/ψ production in *p*+*p* at $\sqrt{s} = 200$ GeV. Pythia describes experimental J/ψ p_T and rapidity spectra well, and it is a useful tool to study J/ψ decay kinematics.

The model of a background was constructed using number e^+e^- pairs in the invariant mass range ($2.8 - 3.2$ GeV/c^2) in the small sample (0.5 million) of Cu+Cu minimum-bias events. Cuts listed in Tab. 3.5 were applied to select electrons. Such approach allowed us to study correlated and combinatorial background.

The signal model was generated using Pythia and consisted of 10 thousand J/ψ decaying into e^+e^- within STAR acceptance. We used $\epsilon_{PID}(p)$ shown in Fig. 3.14 which was obtained for cuts listed in Tab. 3.5.

The first step in our studies was to establish a variable which is most the effective in a background rejection. The initial studies of p_T and momentum cuts using the Cu+Cu data showed that p_T cut has bigger impact on the signal and the background than cut on track momentum. Consequently we focused on single electron p_T cut.

J/ψ signal and background efficiencies are presented on the Fig. 3.14 (left). The blue line is $\epsilon_B(p_T)$ while black line is the $\epsilon_S(p_T)$. The green line shows the signal efficiency obtained from pure simulations, without $\epsilon_{PID}(p)$ included. There is a significant difference between $\epsilon_S(p_T)$ with and without PID incorporated. It shows how important $\epsilon_{PID}(p)$ is for final conclusions.

The obtained results, namely significance vs. electron p_T cut, are shown in Fig. 3.15. Two sets of results were used to estimate N_S and N_B in significance assessment:

- Signal = 550 J/ψ, Signal/Background (S/B) = 1/50, track cuts are summarized in the Tab. 3.5, data set consisted of 19 million minimum-bias events, background was estimated

using event mixing and it was normalized in the M_{inv} range of 1.8 – 2.5 GeV/c^2. The signal and background yields were calculated using bin-by-bin counting in the M_{inv} range 2.8 – 3.15 GeV/c^2. The Sig(p_T) is shown in Fig. 3.15(left), the best significance was noticed for cut of $p_T > 1.177$ GeV/c.

- Signal = 377 J/ψ's, Signal/Background = 1/24, track cuts similar to those summarized in the Tab. 3.5 were used but with cut of $p_T > 0.8$ GeV/c, data set consisted of 26.7 million minimum-bias events, background was estimated using event mixing and normalized to the integral of like-sign background (geometrical mean). The signal and background yields were calculated using bin-by-bin counting in the M_{inv} range 2.8 – 3.15 GeV/c^2. The Sig(p_T) is shown in Fig.3.15(right), the best significance was obtained for cut of $p_T > 1.173$ GeV/c.

The results showed a shallow maximum for p_T of 1.1 – 1.2 GeV/c which gave us a hint where the basic p_T cut should be placed. The best choice is a cut of $p_T > 1.1$ GeV/c because the significance for this cut is almost the same as for $p_T > 1.17$ GeV/c, and the signal efficiency ϵ_S is higher for the cut on $p_T > 1.1$ GeV/c.

The chosen p_T cut was a staring point for further studies aimed at to reduce the background (DCA, ndEdxHtis, PID cuts) and to improve the stability of the results vs. different background models.

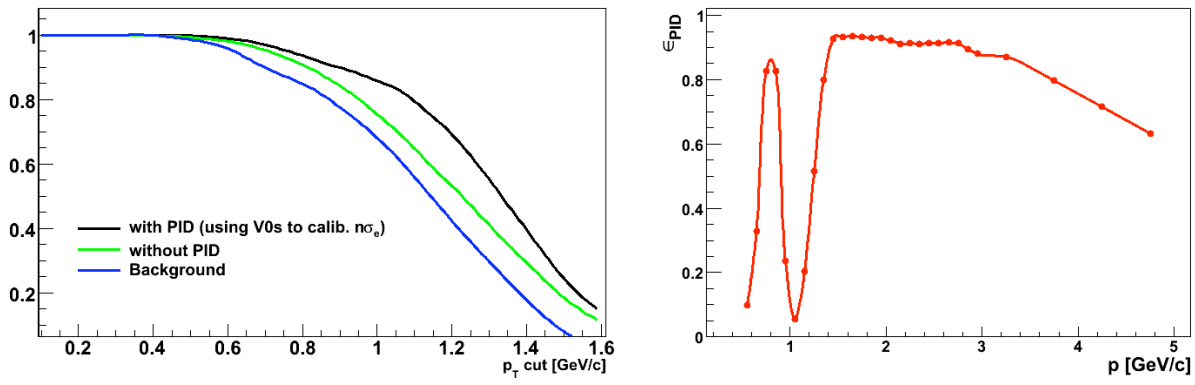

Figure 3.14: Right: Single electron identification efficiency used in the cut studies (calculated with cuts summarized in Tab.3.5). Left: Signal and background efficiencies in cut optimization for Cu+Cu data with Pythia. The blue line represents $\epsilon_B(p_T)$, black line – the $\epsilon_S(p_T)$ and the green line shows $\epsilon_S(p_T)$ without $\epsilon_{PID}(p)$ included.

Table 3.5: List of cuts used in p_T cut studies with Pythia for Cu+Cu minimum-bias collisions.

Cut	Comment
primary tracks DCA < 2 cm	Track originating in the vertex
$nHits > 25$ $nHits/nHitsMax > 0.55$ $nDedxHits > 20$ $\|\eta\| < 1$ $\|charge\| = 1$	Track quality assurance
$p_T >$ 0.1 GeV/c p$>$ 0.5 GeV/c	Basic kinematic cuts
$\|n\sigma_e\| < 2$	Electrons identification
$\|n\sigma_p\| > 2$ $\|n\sigma_K\| > 2$ ($n\sigma_\pi < -3$ or $n\sigma_\pi > 2.5$)	Rejection of tracks likely to be hadrons

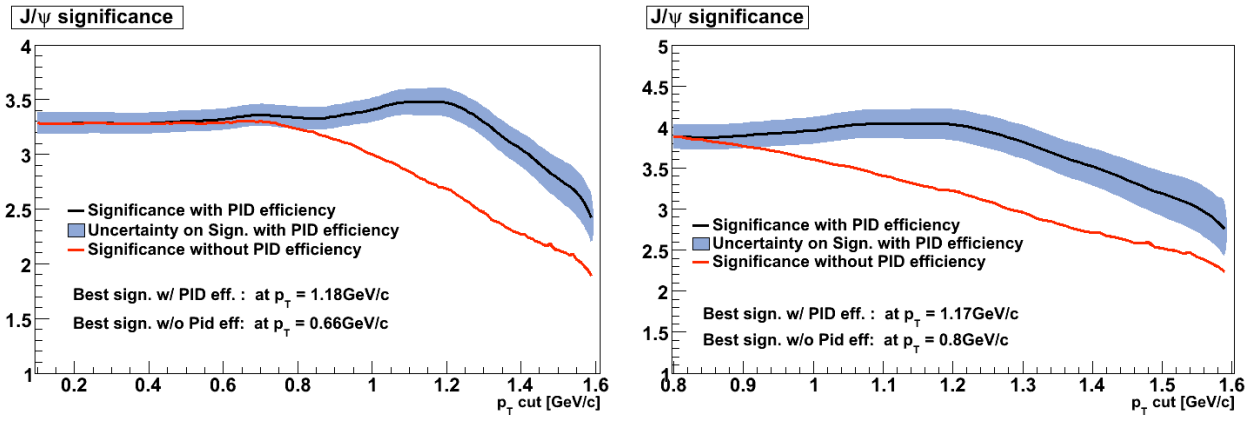

Figure 3.15: Results of cut optimization for Cu+Cu minimum-bias collisions using Pythia. The black line is a significance vs p_T cut when signal and background yields were estimated for $p_T = 0.1$ GeV/c cut (left panel) and $p_T = 0.8$ GeV/c (right panel). The bands represent the statistical error. Additionally, there is a normalization error: 30% for $p_T = 0.1$ GeV/c and 23% for p_T= 0.8 GeV/c (see text for details). The red lines represent $Sig(p_T)$ without $\epsilon_{PID}(p)$ included.

3.7.3 Multivariate cut optimization for Cu+Cu and Au+Au collision using Toolkit for Multivariate Analysis

Simulations by Pythia can provide information about kinematic variables which may be used to established the best signal significance, but do not provide the information about experimental variables, like DCA or number of hits in TPC. Those can be obtained via simulations of a detector response to particles traversing the detector and *embedding* technique, described in section 3.6.1. Embedding provides the experimental observables (number of hits in TPC, DC) as well as reconstructed kinematic variables for tracks (p_T, momentum, pseudorapidity), therefore it can be used to construct a realistic model of the signal, as it is seen by detector, for the cut optimization. Variables which can be used to optimize a selection criteria are restricted to distance of closes approach to primary vertex (DCA), momentum, transverse momentum and number of hits in TPC (or number of fit points). Unfortunately, at the moment the TPC Response Simulator does not provide reliable simulation of ionizing energy loss therefore neither the particle identification nor cut on number of dE/dx hits in TPC can't be studied using embedding. The number of hits in TPC, number of dE/dx points and number of fit points are strongly correlated. In fact cut on dE/dx points determines the distribution of TPC hits and fit points, as is shown in Fig. 3.16 for Cu+Cu collisions. We used this correlation to select nHits value corresponding to nDedxHits cut and to mock up the impact of nDedxHits criteria on J/ψ reconstruction in embedding.

The Toolkit for Multivariate Analysis

The toolkit for multivariate analysis (TMVA) [105, 106] is a ROOT[3]-integrated environment which provides a set of methods for processing, evaluation and application of multivariate signal/background classification. The software was designed specially for high-energy physics, where small signals are hidden in large data sets. TMVA includes a large set of *classifiers* (functions to classify a given event as a signal or a background), which includes:

- Rectangular cut optimisation
- Projective and multidimensional likelihood estimator
- k-Nearest Neighbor algorithm

[3]ROOT is an object-oriented program and library developed by CERN for the data analysis in high-energy physics [107]

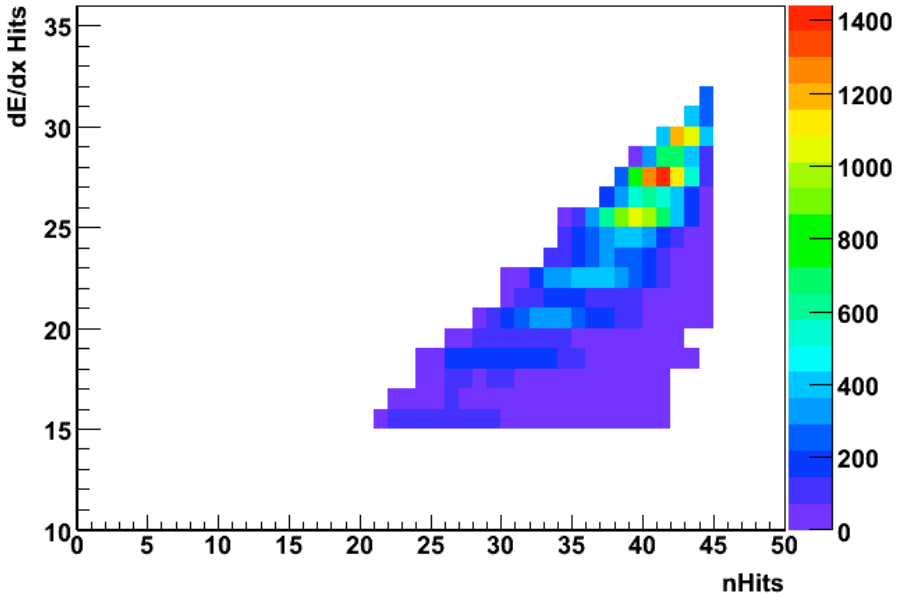

Figure 3.16: Correlation between nHits and dE/dx Hits for electrons selected to reconstruct J/ψ candidates (in a range $2.8 < M_{inv} < 3.2$ GeV/c^2), the initial cut on dE/dx Hits> 14 was applied.

- Fisher and H-Matrix discriminants
- Function discriminant
- Artificial neural networks (3 multilayer perceptron implementations)
- Boosted/bagged decision trees
- RuleFit
- Support Vector Machine

In many cases the classification benefits from preprocessing the data (like removing the corrections between analyzed variables) and TMVA also offers few stages of data preprocessing:

- Decorrelation
- Principal Components Decomposition
- Transformation to uniform and Gaussian distributions

In the study presented here, three classes of classifiers were employed:

1. Rectangular cut optimization [105] – the simplest and most common method for selecting a signal event from a mixture of signal and background events. The optimization procedure consists of application of cuts on discriminating variables and maximization of the background rejection for a given signal significance. As a results, the signal and background efficiencies ϵ_S and ϵ_B are provided and then, knowing the expected signal and background yields, one can calculate the signal significance using Eq. 3.22. The search for the best cut ensemble is provided by multivariate parameters fitters - for this task authors of TMVA recommend Monte Carlo sampling, Genetic Algorithms and Simulated Annealing[105]. The big advantage of the rectangular cuts optimization is simplicity and transparency. The best set of cuts is provided, cuts can be applied directly to the data and also the "quality control" is straightforward - one can validate provided solutions by comparing them to the experimental capabilities, like momentum resolution or DCA distribution etc. The drawback of this method is that multivariate parameters fitting is time consuming and the goodness of the solution decreases quickly with the number of discriminating input variables. Therefore optimization should be reduced to a few variables which have the largest discriminating power.

2. Projective and multidimensional likelihood estimator [105] – this method classifies the events based on maximum likelihood criteria. The likelihood $y_L(i)$ that a given event i is a signal is constructed by multiplying the signal probability densities for all input variables and normalizing by a sum of signal and background likelihoods:

$$y_L(i) = \frac{L_S(i)}{L_S(i) + L_B(i)} \tag{3.24}$$

where:

$$L_S(i) = \prod_{k=1}^{n_{Var}} p_{S,k}(x_k(i)) \tag{3.25}$$

$$L_B(i) = \prod_{k=1}^{n_{Var}} p_{B,k}(x_k(i)) \tag{3.26}$$

$p_{S,k}$ and $p_{B,k}$ are signal and background probability density functions for the k-th input variables x_k.

In this method the input variables are assumed to be independent. In absence of model inaccuracies (like non-linear correlation between discrimination variables), the likelihood $y_L(i)$ provides an optimal separation of the signal from the background. In contrast to

rectangular cuts, which provides the binary classification (event is a signal or a background), the likelihood method returns the probability that event is a signal (fuzzy logic). The training phase for these classifiers is much faster than in the case of rectangular cuts, but the application requires modification of the input data and also the PDFs approximation depends on number of accessible events (the higher the better). It requires storing the entire trees with signal and background in the memory to build the PDFs and this process can be limited by available computing resources. The method of building classification variable $y_L(i)$ is rather simple and it makes classification transparent and rather easy to inspect. The biggest disadvantage is significant performance loss in case of non-linear correlations between input variables.

3. Fisher discriminants (linear discriminant analysis) [105, 108] – in this method events are selected by distinguishing the mean values of the signal and background distributions in a transformed variable space with zero linear correlations. It projects high-dimensional data onto a line in hyperspace of the input variables and performs classification in this one-dimensional space. The projection maximizes the distance between the means of the two classes while minimizing the variance within each class. The classification of the events in signal and background classes relies only on overall sample means for each input variable, class-specific sample means, and total covariance matrix.

   In certain cases performance of Fisher discriminants can be competitive with likelihood methods (e.g. Gaussian distributed variables with linear correlations). However, if signal and background samples have the same mean values then no discrimination at all is achieved, even if the shapes of the distributions are very different.

Background model

The background model was constructed using the real data, combinatorial background was estimated by sum of like-sign pairs with $2.8 < M_{inv} < 3.2$ GeV/c^2. Such method is equivalent to geometrical mean and it was easier to implement in the TMVA environment. It is also less computationally expensive, which is especially important when the rectangular cut optimization is employed. Cuts used to select background pairs are listed in Tab. 3.6 The sample consisted of 19 thousand like-sign pairs for Cu+Cu collisions and 7 thousand pairs for Au+Au.

Table 3.6: List of cuts used in cut optimization studies using TMVA

Cu+Cu cut set 1	**Cu+Cu cut set 2**	**Au+Au**
DCA < 2 cm	DCA < 2 cm	DCA < 3 cm
$nHits > 25$ $nHits/nHitsMax > 0.55$ $nDedxHits > 20$ $\|\eta\| < 1$ $\|charge\| = 1$	$nHits > 25$ $nHits/nHitsMax > 0.55$ $nDedxHits > 18$ $\|\eta\| < 1$ $\|charge\| = 1$	$nFitPts > 20$ $nFitPts/nHitsMax > 0.51$ $\|\eta\| < 1$ $\|charge\| = 1$
$p_T > 0.1$ GeV/c $p > 0.5$ GeV/c	$p_T > 0.8$ GeV/c	$p_T > 0.8$ GeV/c
$\|n\sigma_e\| < 2$	$\|n\sigma_e\| < 2$	$\|n\sigma_e\| < 2$
$\|n\sigma_p\| > 2$ $\|n\sigma_K\| > 2$ ($n\sigma_\pi < -3$ or $n\sigma_\pi > 2.5$)	$\|n\sigma_p\| > 2.5$ $\|n\sigma_K\| > 2$ ($n\sigma_\pi < -3$ or $n\sigma_\pi > 2.5$)	$\|n\sigma_p\| > 2$ $\|n\sigma_K\| > 2$ ($n\sigma_\pi < -3$ or $n\sigma_\pi > 2.5$) $p/E < 2$
19M events	26.7M events	64M events
Signal = 550 $\pm$ 170 J/ψ's Signal: Background = 1:50	Signal = 320 $\pm$ 74 J/ψ's Signal: Background = 1:16	Signal = 1300 $\pm$ 340 J/ψ's Signal: Background = 1:77

Signal model

The signal model was built using Monte Carlo $J/\psi \to e^+e^-$ embedded in Cu+Cu and Au+Au minimum-bias data (100 thousand J/ψ in Cu+Cu and 60 thousand in Au+Au events). The initial J/ψ p_T spectrum is flat to provide sufficient statistic for efficiency calculation at the whole considered p_T range. To correct that distribution and to bring it as close as possible to the reality, p_T distribution was weighted with J/ψ p_T spectra in 0-60% Cu+Cu [74] and Au+Au minimum-bias collisions at $\sqrt{s_{NN}} = 200$ GeV [75]. To avoid the effects of the momentum resolutions, the simulated (Monte Carlo) p_T was used in the re-weighting procedure. Additionally, a single electron identification efficiency was included in the study.

Then the initial number of J/ψ in a signal sample for a given p_T is given by:

$$N^{Init}_{J/\psi}(p_T) = N^{MC}_{J/\psi}(p_T) \times w; \quad w = A \cdot p_T \cdot \left[1 + p_T^2/B^2\right]^C \tag{3.27}$$

where: $N_{J/\psi}^{MC}$ – the original number of J/ψ in embedding for a given p_T bin, $N_{J/\psi}^{Init}(p_T)$ – number of J/ψ after re-weighting i.e. with realistic p_T spectrum, w – weight defined by A, B are C parameters fitted to the measured J/ψ p_T spectrum; example of the fit for Cu+Cu collisions is shown in Fig. 3.17

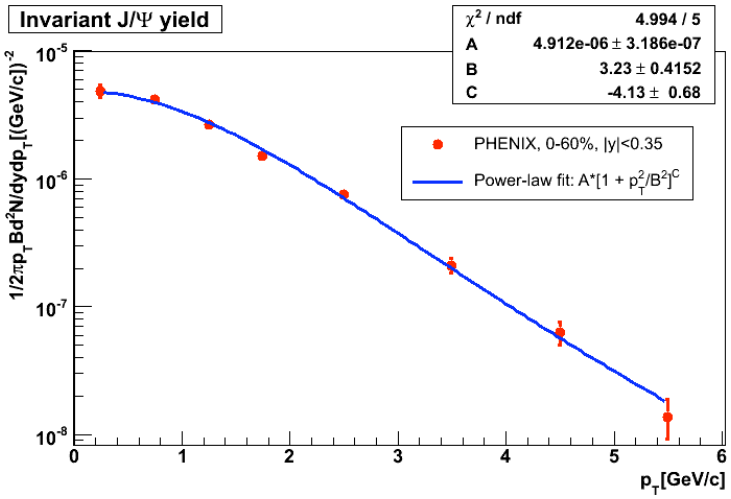

Figure 3.17: J/ψ p_T spectrum [74] with a power-law parametrization.

The number of J/ψ mesons surviving kinematic and PID cuts $N_{J/\psi}^{surv}(p_T)$ is given by:

$$N_{J/\psi}^{surv}(p_T) = N_{J/\psi}^{kin.cuts}(p_T) \times w \times \epsilon_{PID}(p^{e_1}) \times \epsilon_{PID}(p^{e_2}) \tag{3.28}$$

where: $N_{J/\psi}^{kin.cuts}$ - number of J/ψ surviving kinematic cuts, $Pid(p^e)$ - single electron identification efficiency for a given momentum p, w is weight defined in Eq. 3.27.

Transformation of the input variables

Signal (or background) pair is destroyed if one of the electrons does not pass specific cut. Therefore for each pair we assigned additional variable – a value of given cut which eliminate at least one electron in pair and therefore destroys the pair. Such implementation improves classifiers' performance because the number of conditional expressions to evaluate is smaller.

These new variables are defined by:

- $p_T\ cut = min(p_T^{e1}, p_T^{e2})$
- $p\ cut = min(p^{e1}, p^{e2})$
- $nHits\ cut = min(nHits^{e1}, nHits^{e2})$

- $DCA\ cut = max(DCA^{e1}, DCA^{e2})$

For example, if electrons in the pair have p_T of 2 GeV/c and 1.5 GeV/c then $p_T\ cut = 1.5$ GeV/c.

Results

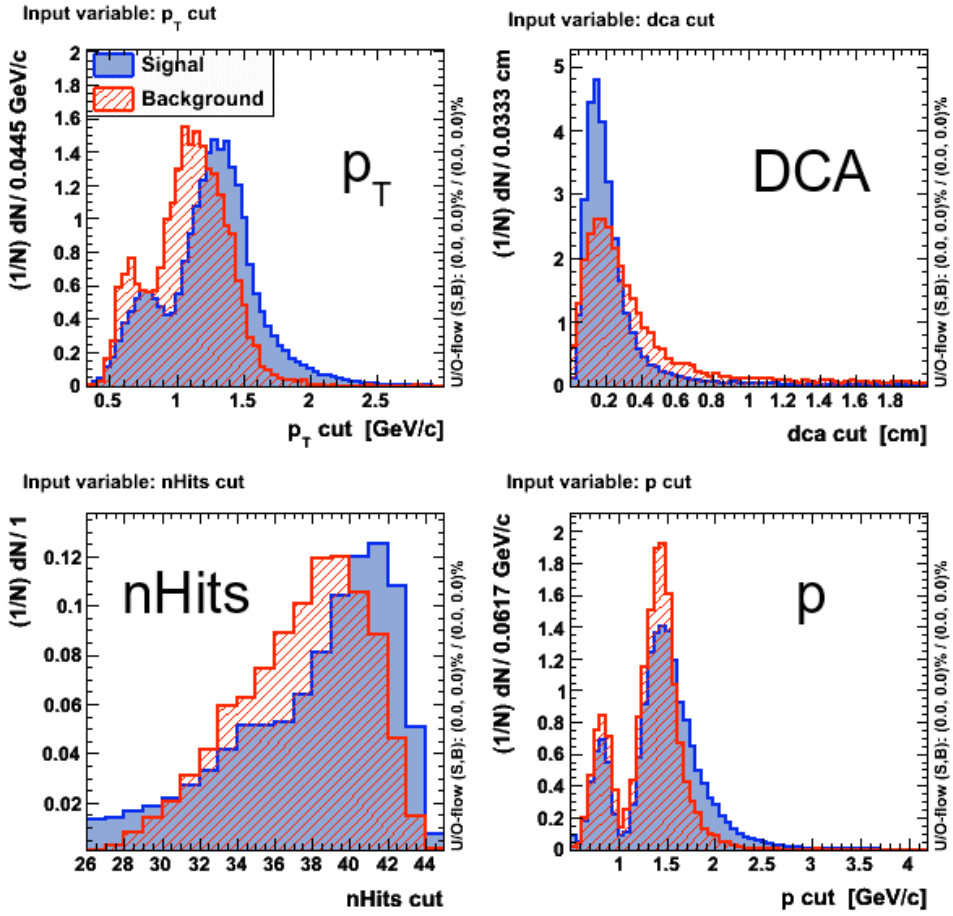

Figure 3.18: Input variables used in cut studies for min-bias Cu+Cu collisions, the distributions correspond to cut set 2 in Tab. 3.6. The blue histogram represents the signal distribution, the red one - background. The input variables are described in the text.

Cu+Cu

In the case of Cu+Cu collisions, two different set of cuts were studied and they are summarized in Tab. 3.6. The main difference between them are the condition applied to reject protons and a p_T cut. With the first set of cuts we were studying the signal significance over broad momentum

and p_T range, which is a cross-check to results obtained using Pythia. The second one gives better S/B ratio, better significance and therefore more precise estimation of the expected signal yield. It was used to validate results of cuts optimization. The model of the signal is rather complex and some features of the signal are unknown therefore it is important to check the consistency between significance predicted by TMVA and seen in the real data. If a given feature of the signal is not well reproduce in a model, then cuts tuned based on model would give significantly different results for simulations and the real data. Consequently such selection criteria should not be applied blindly in analysis. For the set 2, the cut of $p_T > 0.8$ GeV/c was chosen as it provides rather good signal-to-background ratio and it is still far away from the region when the best significance is expected ($p_T \sim 1.1-1.2$ GeV/c based on Pythia simulations - see section 3.7.2) and therefore the results are unlikely biased by initial conditions.

The distributions of analyzed variables are presented in Fig. 3.18. The blue and red histograms represent the signal and background distributions, respectively. To select variables with the largest discrimination power, we did a full 4-dimensional optimization in which the p_T, momentum, DCA and nHit cuts were used. The results have shown that the cuts on momentum and nHits do not provide discrimination power. The optimal nHits cut was always the same as the initial one. Therefore we selected tracks with $nHits > 25$ to ensure good track quality and momentum resolution, and then we used this condition in our further studies. The cut on momentum was always the same as p_T cut which can be easily explained: p_T cut is more effective in background rejection and it is strongly correlated with particle momentum. TMVA provides also a ranking of variables in respect of signal and background separation, and the highest rank was assigned to p_T. It is consistent with signal and background distributions shown of Fig. 3.18: the best separation is observed for p_T cut. Consequently we focused on p_T and DCA in our studies and the analysis was done is two stages:

- p_T cut optimization for cut set 1 presented in Tab. 3.6 (aimed as crosscheck to the results described in section 3.7.2)
- p_T vs DCA cut study for cut set 2 in Tab. 3.6

Figure 3.19 presents signal significance and signal-to-background ratio vs. p_T cut. The distribution is consistent with the results obtained with Pythia (Fig. 3.15) - in both cases there is a shallow maximum around $p_T \sim 1.1 - 1.2$ GeV/c. Similar significance as for $p_T \approx 1.1$ GeV/c is also visible for $p_T \approx 0.4$ GeV/c but in the latter case the signal-to-background ratio

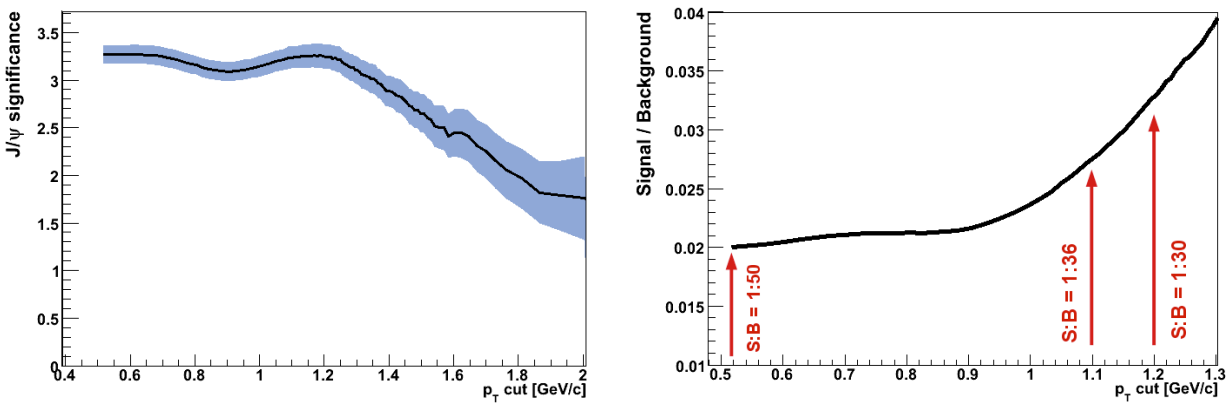

Figure 3.19: Signal significance (left) and Signal/Background ratio (right) vs. p_T cut for cut set 1. The band shows a statistical error calculated as described in Sec. 3.7.1. Additionally, there is a 30% systematic error due to initial J/ψ yield estimation.

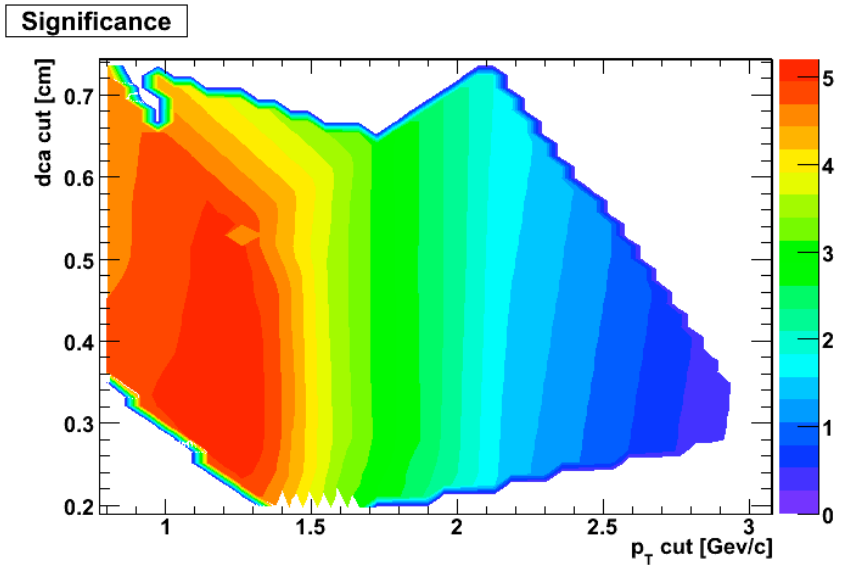

Figure 3.20: Signal significance vs. p_T and DCA cut for cut set 2. Additionally there is 23% systematic error due to initial yield estimation.

Table 3.7: Performance of TMVA classifiers used in two-dimensional p_T and DCA cut studies for cut set 2 in Tab. 3.6. Predictions for the best significance for each method are presented.

Classifier	Significance	Signal	Background	ϵ_S	ϵ_{Bg}
Cuts (Monte Carlo)	5.3	202	1240	0.6	0.24
Cuts (Genetic Algorithms)	5.3	207	1303	0.65	0.25
Likelihood	5.5	192	1031	0.6	0.2
Fisher	5.1	228	1749	0.71	0.34

is smaller (1:50) than for $p_T \approx 1.1$ GeV/c (1:36). Also the expected hadron contamination is bigger, therefore the cut on $p_T \approx 1.1$ GeV/c is a better choice. The significance obtained for two-dimensional cut studies (p_T vs DCA) using cut set 2 is presented in Fig. 3.20. The optimal results were predicted for $p_T > 1.15$ GeV/c and $DCA < 0.3$ cm. The predicted significance was $\simeq 5.3$ and expected signal yield was $\simeq 205 J/\psi's$ (Tab. 3.7). There is a sizable difference between those predictions and the real data results: for the real data we got 150 J/ψ's and the significance of 3.6. Although there is a 23% systematic error due to initial yield estimation, obtained results fall below expectations. This suggests that there are some model inaccuracies (for example, a simulated DCA distribution of the signal is not close enough to the real one). Therefore, the DCA cut was set at 1 cm - such choice still eliminates some background and it is safe in terms of signal rejections.

Table 3.7 and Fig. 3.21 present the comparison of the performance of different classifiers. For the given problem the simplest method (Cuts) gave similar results as more sophisticated, statistical classifiers (Fisher, Likelihood). The likelihood would probably deliver even better results but we are limited by model capabilities – it did not include particle identification cuts while hadron contamination is significant source of combinatorial background. With PID cuts included Likelihood can be very useful, here we tested proof of principle.

Au+Au

The basic cuts used in studies are summarized in Tab. 3.6. Based on results for Cu+Cu, $p_T > 0.8$ GeV/c cut was chosen. It provides rather good S/B ratio and more precise validation of cuts study results against real data while it still far away from the region when the best significance is expected. The initial J/ψ yield needed for normalization purpose was obtain using event-

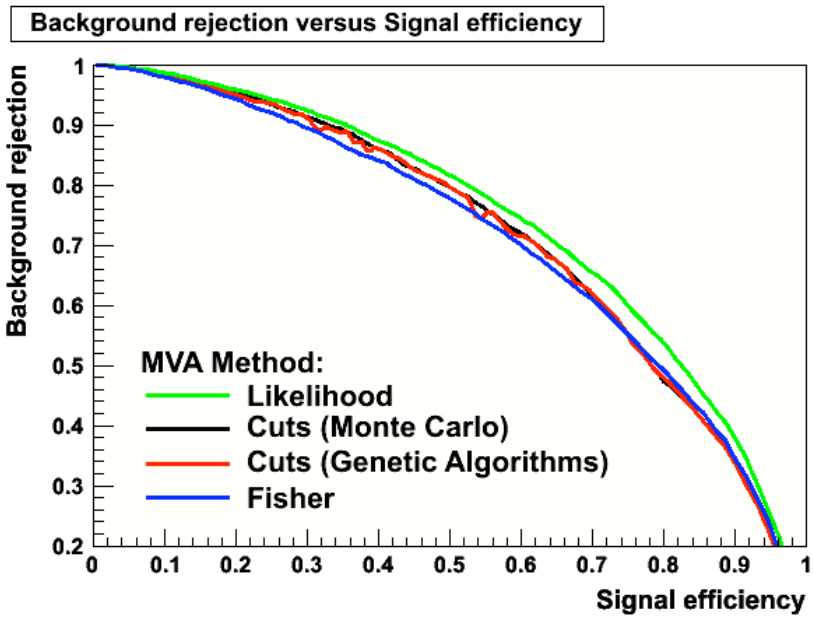

Figure 3.21: Background rejection vs. signal efficiency for selected classifiers for cut set 2 in Tab. 3.6. The best performance (highest background rejection for a given signal efficiency) was achieved for the Likelihood method.

mixing to estimate combinatorial background.

The distributions of analyzed variables is presented in Fig. 3.22. It is clear that p_T cut provides the largest discrimination power. As a crosscheck to this observation a set of 2D analysis (p_T vs DCA, p_T vs nFitPts) were done. The conclusions were similar to those for Cu+Cu: nFitPts cut does not provide discrimination power while cut on momentum is strongly correlated with p_T. As it was mentioned in section 3.4.1, good pointing resolution is require when a track is projected on BEMC, therefore we required nFitPts ≥ 25 in further studies to ensure good track quality.

We focused firstly on p_T cut. Signal significance vs. p_T cut is shown in Fig. 3.23. The plot shows a shallow maximum for $p_T \sim 1.2 - 1.4$ GeV/c. Results of two-dimensional analysis of significance vs p_T and DCA cut is presented in Fig. 3.24. The significance depends strongly on p_T and it is almost independent on DCA. The region of best significance in Fig. 3.24 falls in p_T range of 1.15 – 1.3 GeV/c and DCA limits of 0.8 – 3 cm. We selected tracks with $DCA < 1$ cm to avoid tails in DCA distribution.

The significance predicted for the optimal set of cuts is $\simeq 4.6$ (Fig. 3.24 and 3.23). The significance observed in the real data for cut on $p_T > 1.2$ GeV/c and $DCA < 1$ cm (with combinatorial background estimated using event-mixing) was 5.8. Therefore the predicted and

the obtained results are consistent within 26% normalization uncertainty.

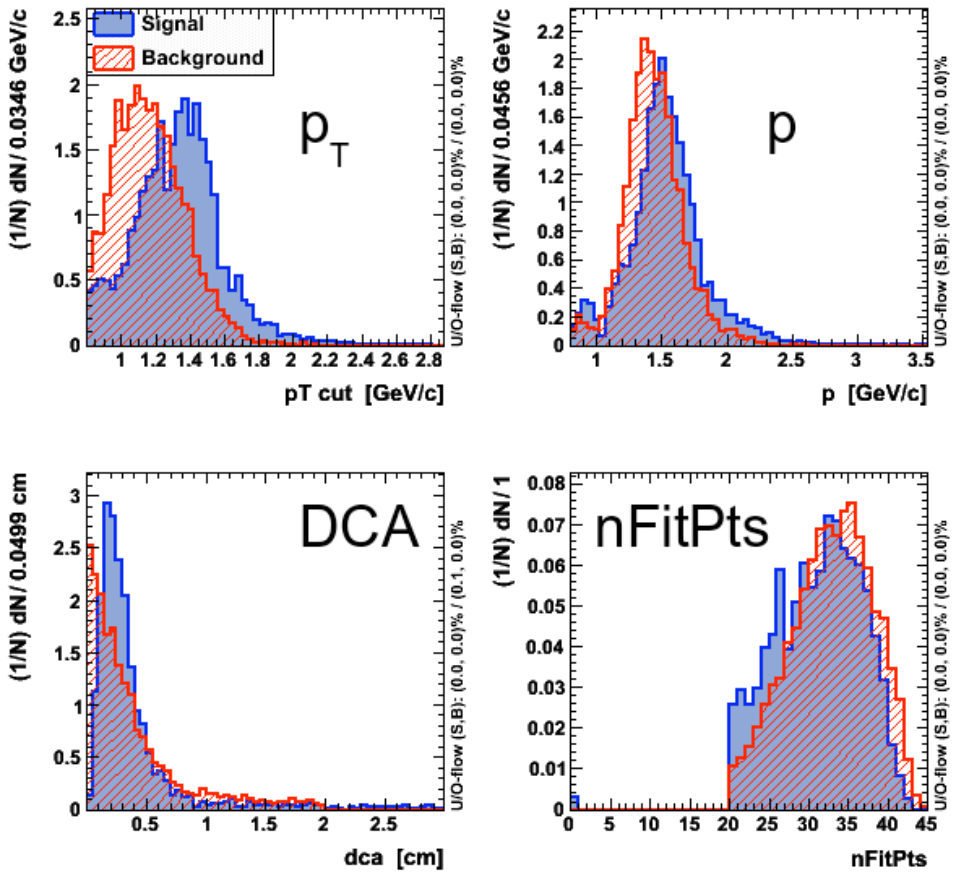

Figure 3.22: Input variables used in cut studies for Au+Au collisions, the distributions correspond to cuts listed in third column in Tab. 3.6. The blue histogram represents the signal distribution, the red one - background. The input variables are described in the text.

3.7.4 Summary

Our cut studies provided directions what are the most important variables and also what are the optimal selection criteria in the analysis. For some of quantities (like nDedxHits, nHits and nFitPts) there was no strong indication where a cut should be placed and we chose particular values based on our understanding of the detector and track reconstruction process. The stability of results were crosschecked by varying cuts.

On the other hand the obtained results are promising and at the moment they are only limited by accuracy of the signal model. With improved Monte Carlo simulations of the detector,

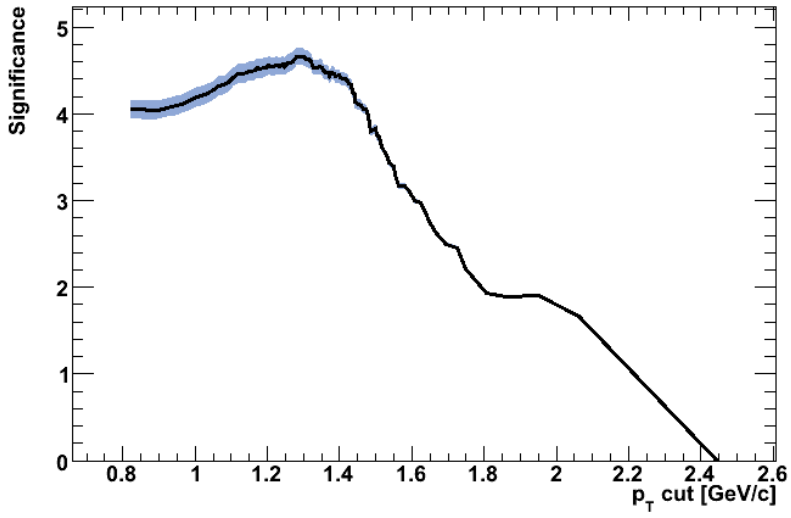

Figure 3.23: Signal significance vs. p_T cut. The band shows a statistical error calculated as described in Sec. 3.7.1. Additionally there is 26% systematic error due to initial J/ψ yield estimation.

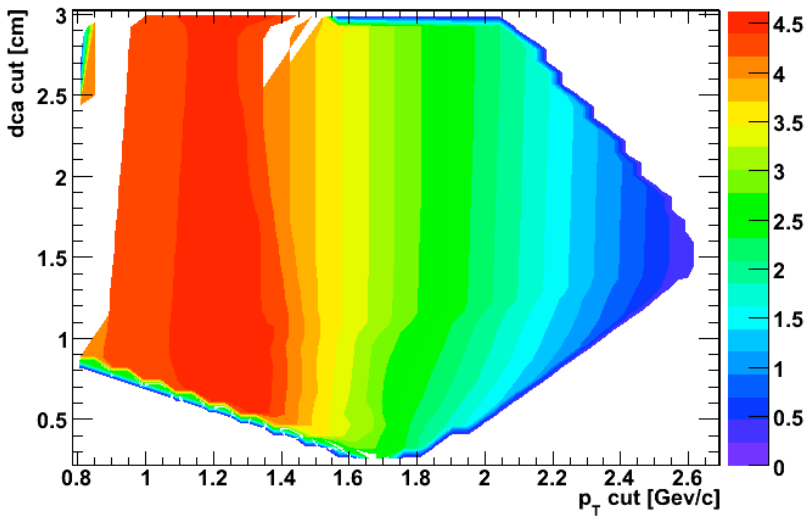

Figure 3.24: Signal significance vs. p_T and DCA cut. Additionally there is 26% systematic error due to initial yield estimation.

especially those for dE/dx, TMVA will allow to extract a maximum of the available information from the data.

Chapter 4

J/ψ Spectra

4.1 J/ψ yield extraction

As described in Sec. 3.3, we identified J/ψ on statistical basis as a peak in M_{inv} spectrum. The combinatorial background was estimated using a few different method:

1. Like-sign pairs: $N_{Bg} = 2 \cdot \sqrt{N_{++} \cdot N_{--}}$

2. Rotation: single track rotation by 180° around primary vertex

3. Event-mixing: in case of Cu+Cu events, we were mixing electrons and positrons using pool of 100 events in the same centrality class (0-10%, 10-20%, ...) with the difference $\Delta Vz < 5$ cm and with the difference in multiplicity less than 10%. We used slightly different parameters for Au+Au. The vertex distribution is narrower than in Cu+Cu data therefore we required $\Delta Vz < 0.5$ cm. Because the available statistics was higher than in the case of Cu+Cu data, we were mixing events with the difference in multiplicity less than 5%.

   Three different normalization methods were used:

   - normalization in M_{inv} range below J/ψ peak (1.8 – 2.7 GeV/c^2)
   - normalization to the total number of entries in the like-sign background. Event-mixing gives a small statistical error if enough events is mixed, although it requires a proper normalization. If the shape of event-mixing background is different from the shape of a background in the real data (for example, due to correlations in a

background) than normalization in different ranges of M_{inv} may give different results. Therefore it may provide an additional systematic error. Normalization to like-sign background allows to normalize the event mixing background in a full M_{inv} range.

- "side bands": normalization in M_{inv} range below and above J/ψ peak simultaneously ($1.8 < M_{inv} < 2.7$ GeV/c^2 and $3.5 < M_{inv} < 4.0$ GeV/c^2).

After a combinatorial background subtraction, J/ψ yield can be extracted. We used two methods for this purpose: bin counting in the mass range of J/ψ and a Monte Carlo template (see section 4.2) fitted to J/ψ peak in real data. The difference between obtained results was included in systematic uncertainty.

Bin counting

The bin counting was done in the region 2.9 – 3.15 GeV/c^2 for Cu+Cu collision and 2.9 – 3.2 GeV/c^2 in the case of Au+Au. Such M_{inv} windows were chosen based on Monte-Carlo simulations. The lower bound was set to account for Bremsstrahlung due to electron interactions with the material inside the STAR detector, particularly with the silicon inner trackers (SSD and SVT). Such energy loss leads to reconstruction of e^+e^- with lower M_{inv} than parent J/ψ and consequently a tail on the left hand side of J/ψ peak (Fig. 4.1). The upper bound for Cu+Cu is slightly lower than for Au+Au collisions to reduce signal fluctuations. The available statistic for Cu+Cu is lower and fluctuations could effect stronger results in Cu+Cu than in Au+Au data.

***J/ψ* line shape method**

In order to minimize the influence of statistical fluctuations, we used a Monte Carlo shape of the J/ψ mass peak to extract the raw yield. The Monte Carlo J/ψ peak (so called "line shape") was obtained using embedding technique described in Sec. 3.6.1 and it is presented in Fig. 4.1 for both Cu+Cu and Au+Au data. The signal shape from simulation is fitted to the data and the overall integral of the histograms on Fig. 4.1 is left as a free parameter in the fit, which allows us to obtain the J/ψ yield. The fit was done in the same M_{inv} range as bin counting, and the fit quality was assessed using χ^2 method. In the case of Cu+Cu, $\chi^2/ndf \simeq 1.4$ while $\chi^2/ndf \simeq 1.6$ for Au+Au collisions. The fit quality is satisfactory. The difference between real data and Monte Carlo are caused by fluctuations in real data or by imperfect description of the

detector material in simulations.

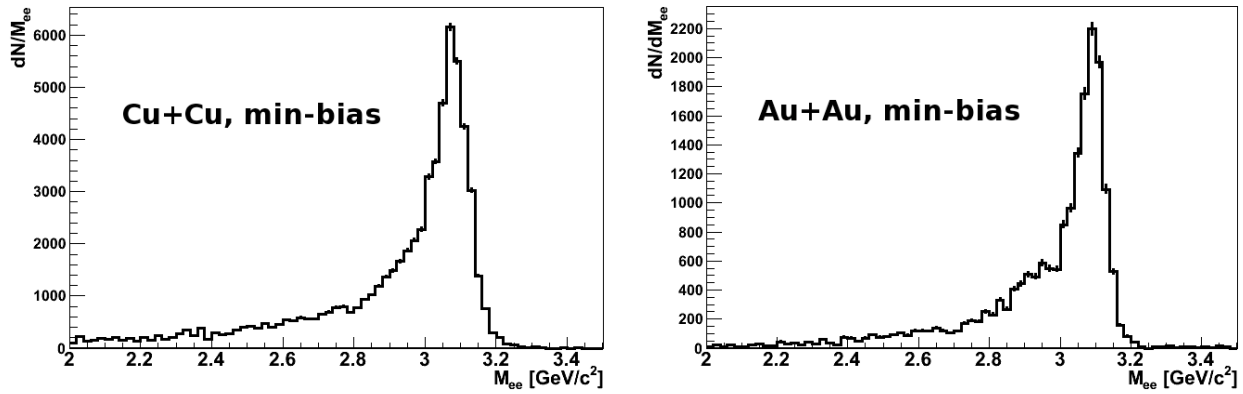

Figure 4.1: J/ψ line shape in Monte Carlo simulations. The tail due to Bremsstrahlung on the left hand side of J/ψ peak is clearly visible.

4.1.1 Trigger bias correction in Au+Au collisions

The results in Au+Au collisions were effected the trigger biases (described in Sec. 3.2.2), and therefore needed to be corrected for aforementioned biases by event-wise re-weighing. The weights depend on V_z and multiplicity (represented by gRefMult, see Sec. 3.2.2) of the event. The weights were calculated in V_z bins of 2 cm. In each V_z bin the real data and Monte Carlo gRefMult distributions were normalized in the range of gRefMult> 500. Then the weights, defined as a ratio of Monte Carlo to real data gRefMult, were calculated. Those weights were used to obtain the unbiased distribution. For each V_z bin we applied the gRefMult dependent weights to the three-dimensional histogram (gRefMult vs invariant mass of the e^+e^- pair vs p_T of the pair). Then the histograms for all V_z bins were summed into one master histogram for $|V_z| < 30$ cm. The same procedure was applied to event-mixing background.

4.1.2 J/ψ raw yield

The J/ψ signal with Monte Carlo line shape fits in Cu+Cu minimum-bias collisions and integrated p_T is shown in Fig. 4.2 and 4.3. The signal with significance of 4.5 is observed while S/B ratio is 1/13. In the case of Cu+Cu, after the combinatorial background subtraction there is no residual background observed. The comparison of different background models gave results consistent within one standard deviation. The event mixing provides the smallest statistical errors on the estimated background therefore it was used to calculate the final yields. We nor-

malized the background to the total number of entries in the like-sign background, the other methods of normalizations were tried and the differences were included in the systematic error. The J/ψ signal observed in Cu+Cu collisions in different p_T bins and centrality classes is shown in Fig. 4.4 and summarized in Tab. 4.2. In the case of events with 20-60% centrality, the limited statistics allowed us only to estimate the upper limit for J/ψ yield.

Figures 4.5 and 4.6 show M_{inv} distribution in minimum-bias Au+Au events with combinatorial background estimated by like-sign and event mixing methods. These are obtained before correction for the trigger bias described in Sec. 3.2.2. The signal has the significance of 6 and S/B ratio is 1/28. All tested models of combinatorial background gave consistent results and the J/ψ yield for each of them is reported in Tab. 4.3. The event mixing provides smallest statistical errors on the estimated background therefore this technique was used to calculate the final yield. The normalization in low mass region (1.8 – 2.7 GeV/c^2) gave almost identical results for integrated J/ψ signal as normalization to the like-sign background. Because the normalization to the like-sign background is more computational expensive (it would require trigger bias corrections to be applied also to like-sign background), therefore we chose the low mass normalization to calculate the final J/ψ yields. The results from others methods were included in the systematic error assessment.

To estimate the M_{inv} resolution and a measured value of J/ψ mass, J/ψ peak was fitted by Gaussian function:

$$f(m_{ee}) = A \times e^{-\frac{(m_{ee}-M)^2}{\sigma^2}} \tag{4.1}$$

where σ is a measure of experimental mass resolution and parameter M reflects J/ψ mass if the peak has a Gaussian shape. The Gaussian fit for both Cu+Cu and Au+Au collisions gave M slightly lower than J/ψ mass provided by Particle Data Group. The main reason of that is the electron Bremsstrahlung, which leads to reconstruction of e^+e^- pairs with lower mass than the original J/ψ, and consequently a non-Gaussian shape of the peak. Therefore the tail due to Bremsstrahlung shifts the location of the maximum in the fit.

The shape of M_{inv} distribution of combinatorial background is determined by kinematic cuts (mostly cut on p_T of electro). The shape of this distribution changes with p_T of e^+e^- pair which is shown in Fig. 4.7 (left panels). For low-p_T pairs ($p_T < 1$ GeV/c) the p_T cut removes a significant portion of low-mass e^+e^- pairs (many electrons in this range have p_T lower than p_T cut) and the distribution is peaked at about 3 GeV/c^2. In case of pairs with intermediate p_T ($1 - 2$ GeV/c^2) the average p_T of the electrons is higher and therefore less low-mass pairs

are rejected and M_{inv} distribution has the maximum at about 2.6 GeV/c^2. For pairs with p_T>2 GeV/c, almost all electrons survive cuts and there is no significant loss in low-mass region therefore a monotonic M_{inv} distribution of combinatorial background is observed.

The available statistics allowed us to extract J/ψ signal in 3 p_T bins in minimum-bias Au+Au events, and the integrated yield in two centrality classes (0-20% and 20-80%). The signal observed in Au+Au collisions, after the corrections for the trigger bias, in different p_T bins and centrality classes is shown in Fig. 4.7 and 4.8 and summarized in Tab. 4.4. The available statistics was high enough that we attempted to quantify a possible residual background using first and second order polynomials. We fitted a sum of 1^{st} (or 2^{nd}) polynomial and J/ψ line shape to M_{inv} spectrum after combinatorial background subtraction. The example of such fit is shown in Fig 4.9. The results of these studies were included in the systematic error evaluation.

Most of J/ψ's is produced in central collisions and only a small fraction is produced in peripheral events [75]. Therefore, when the data were corrected for a deficit in peripheral events, the overall number of events increased more than the number of observed J/ψ. Consequently, the yield per event decreased by $\simeq 10\%$.

Table 4.1: Integrated J/ψ signal in minimum-bias Cu+Cu collisions

Background	Bin counting in 2.9-3.15 GeV/c^2	J/ψ line shape in 2.9-3.15 GeV/c^2
Event-mixing like-sign norm.	278 $\pm$ 60	235 $\pm$ 49
Event-mixing "Side bands"	236$\pm$ 60	203 $\pm$ 49
Event-mixing	281 $\pm$ 60	237 $\pm$ 49
Rotational	248 $\pm$ 82	199 $\pm$ 68
Like-sign	263 $\pm$ 83	231 $\pm$ 68

where: "Event-mixing 'Side bands'" represents the background obtained with event-mixing method and normalized in $1.8 < M_{inv} < 2.7$ GeV/c^2 and $3.5 < M_{inv} < 4.0$ GeV/c^2, "Event-mixing" denotes the background obtained with event-mixing method and normalized in $1.8 < M_{inv} < 2.7$ GeV/c^{2}and "Event-mixing like-sign norm." represents the background obtained with event-mixing method and normalized to the total number of entries in the like-sign background.

Table 4.2: J/ψ signal in centrality classes of Cu+Cu collisions

p_T range [GeV/c]	Bin counting in 2.9-3.15 GeV/c^2	J/ψ line shape in 2.9-3.15 GeV/c^2
0-60% (min-bias events)		
integrated	278 $\pm$ 60	235 $\pm$ 49
0-1.0	107 $\pm$ 38	84 $\pm$ 31
1.0-5.0	156 $\pm$ 46	137 $\pm$ 38
0-20% (central events)		
integrated	226 $\pm$ 51	180 $\pm$ 42
20-60% (peripheral events)		
integrated	48 $\pm$ 30	47 $\pm$ 25

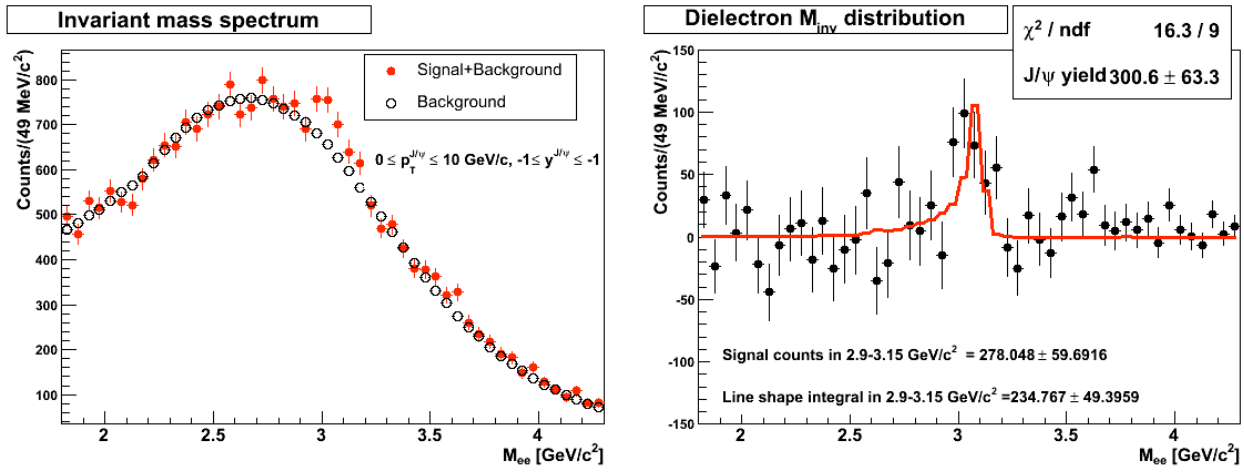

Figure 4.2: J/ψ signal and the background obtained with event-mixing method described in the text. The results for Cu+Cu minimum-bias collisions and integrated p_T are presented. Left: M_{inv} distribution before background subtraction; right: M_{inv} spectrum after background subtraction with the Monte Carlo simulated J/ψ line shape fit.

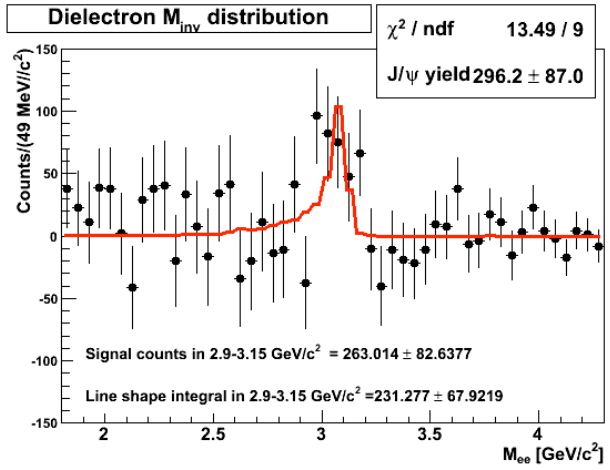

Like-sign background

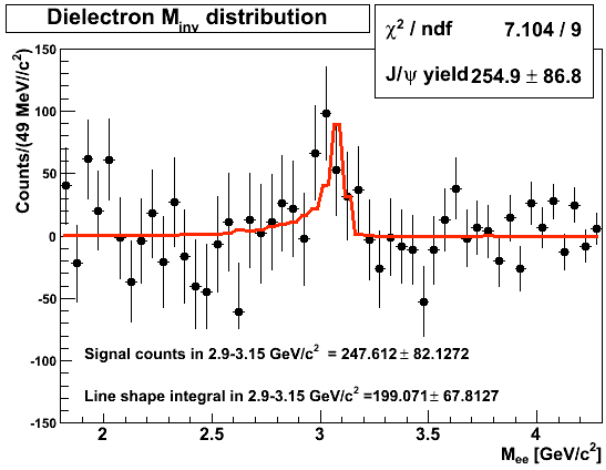

Rotational background

Figure 4.3: J/ψ signal with the combinatorial background subtracted. The background was obtained with like-sign and rotational methods described in the text. The results for Cu+Cu minimum-bias collisions and integrated p_T are presented. The red line represents the Monte Carlo simulated J/ψ line shape fit.

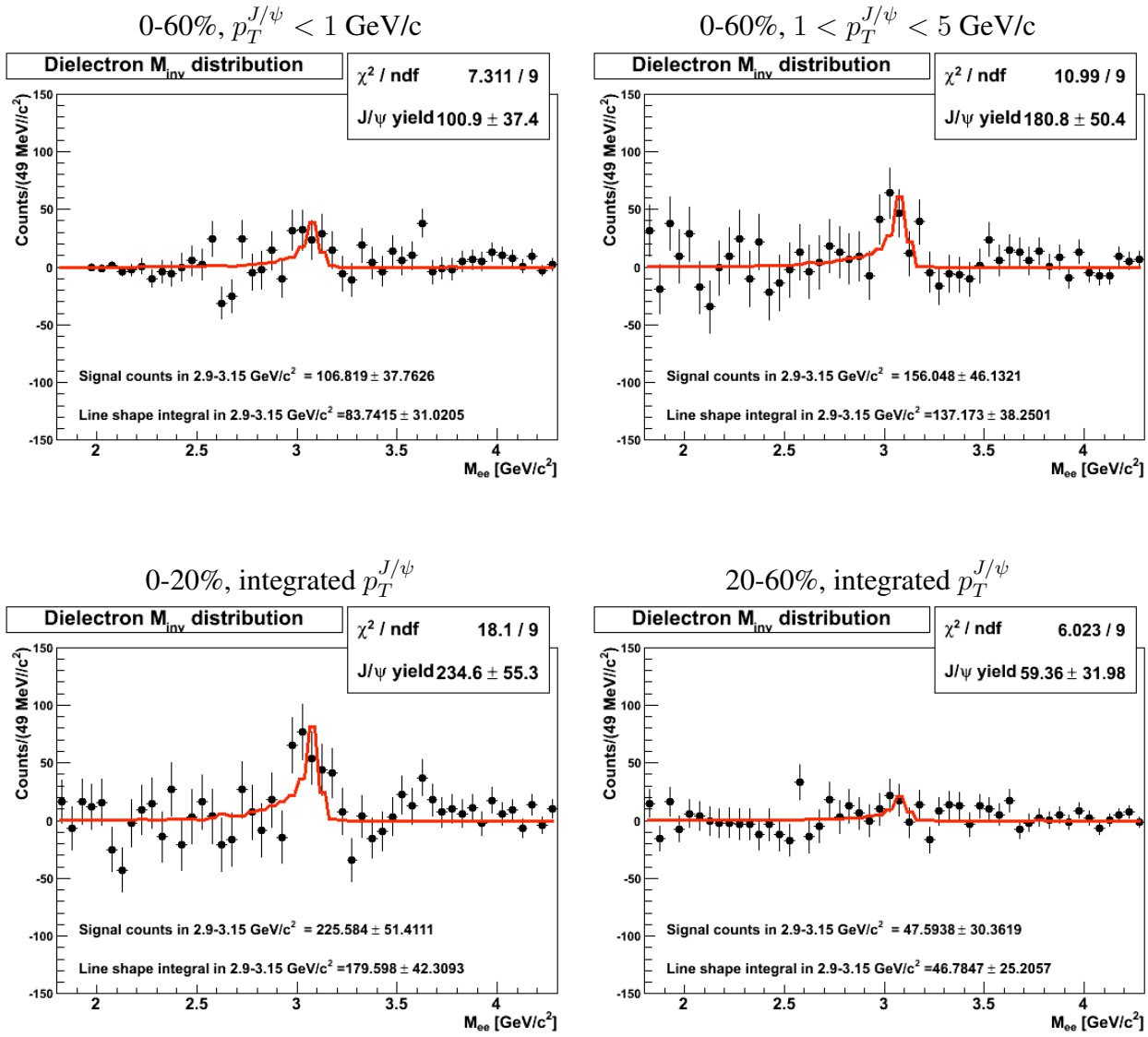

Figure 4.4: J/ψ signal in p_T (upper row) and centrality (bottom row) bins of Cu+Cu collisions with the combinatorial background subtracted. The background was obtained with event-mixing method described in the text. The red line represents the Monte Carlo simulated J/ψ line shape fit.

Table 4.3: J/ψ signal in min-bias Au+Au events (0-80%) before corrections for the trigger bias.

Background	Bin counting in 2.9-3.2 GeV/c^2
Event-mixing like-sign norm.	1080 $\pm$ 184
Like-sign	856 $\pm$ 251
Event-mixing	1094 $\pm$ 184
Rotational	804 $\pm$ 251
Event-mixing "Side bands"	984 $\pm$ 184

Table 4.4: J/ψ signal in different centrality classes of Au+Au collisions. The presented results were corrected for the trigger bias

p_T range [GeV/c]	Bin counting in 2.9-3.2 GeV/c^2	J/ψ line shape in 2.9-3.2 GeV/c^2
0-80% (min-bias events)		
integrated	1225 $\pm$ 199	1155 $\pm$ 149
0-1.0	521 $\pm$ 133	508 $\pm$ 104
1.0-2.0	227 $\pm$ 117	282 $\pm$ 92
2.0-5.0	300 $\pm$ 89	238 $\pm$ 69
0-20% (central events)		
integrated	728 $\pm$ 175	733 $\pm$ 137
20-80% (peripheral events)		
integrated	491 $\pm$ 92	416 $\pm$ 73

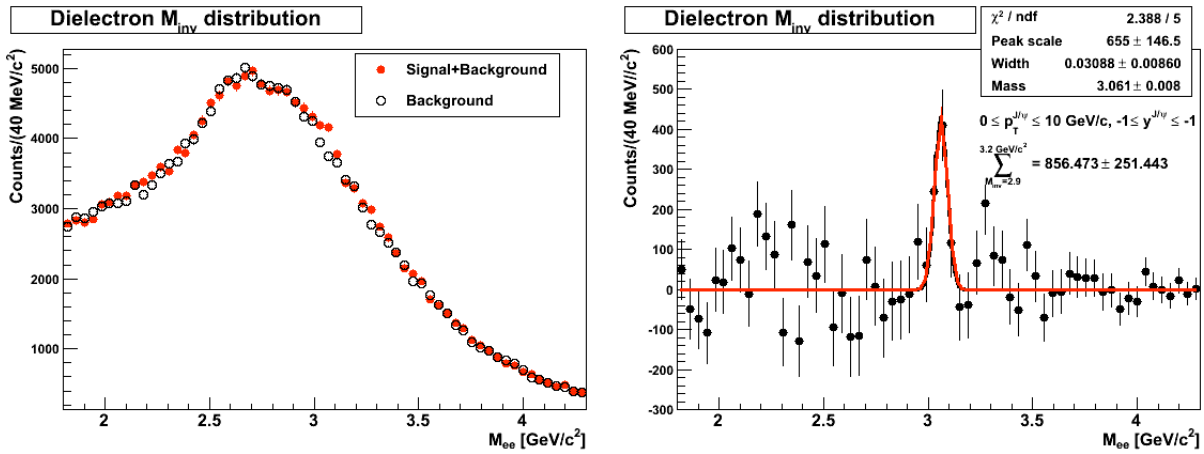

Figure 4.5: J/ψ signal and the background obtained with like-sign method described in the text. The results for Au+Au minimum-bias collisions and integrated p_T are presented. Left: M_{inv} distribution before background subtraction; right: M_{inv} spectrum after background subtraction with a Gaussian fit. The results before the corrections for the trigger bias are shown.

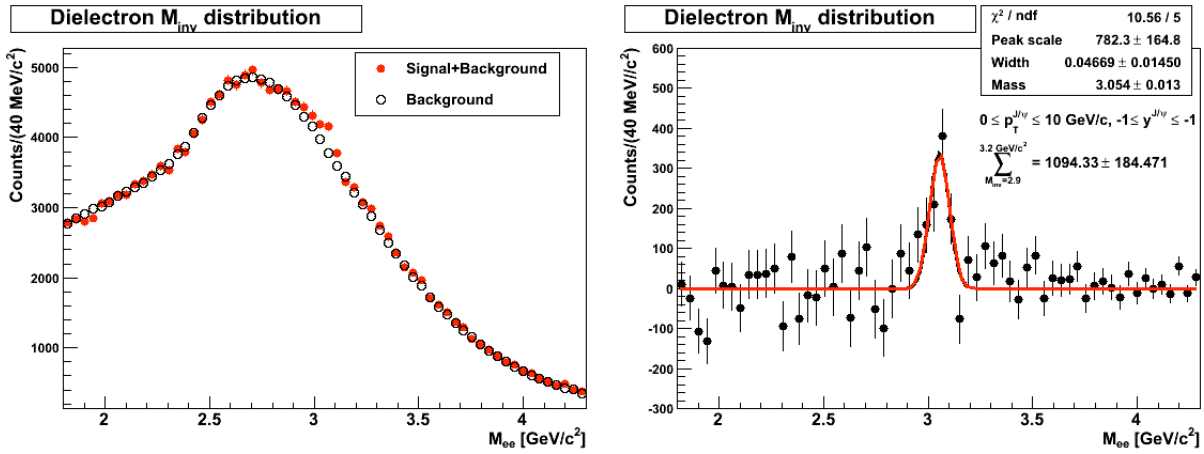

Figure 4.6: J/ψ signal and the background obtained with event-mixing method described in the text. The background was normalize in $1.8 < M_{inv} < 2.7$ GeV/c^2. The results for Au+Au minimum-bias collisions and integrated p_T are presented. Left: M_{inv} distribution before background subtraction; right: M_{inv} spectrum after background subtraction with a Gaussian fit. The results before the corrections for the trigger bias are shown.

$p_T^{J/\psi} < 1$ **GeV/c**

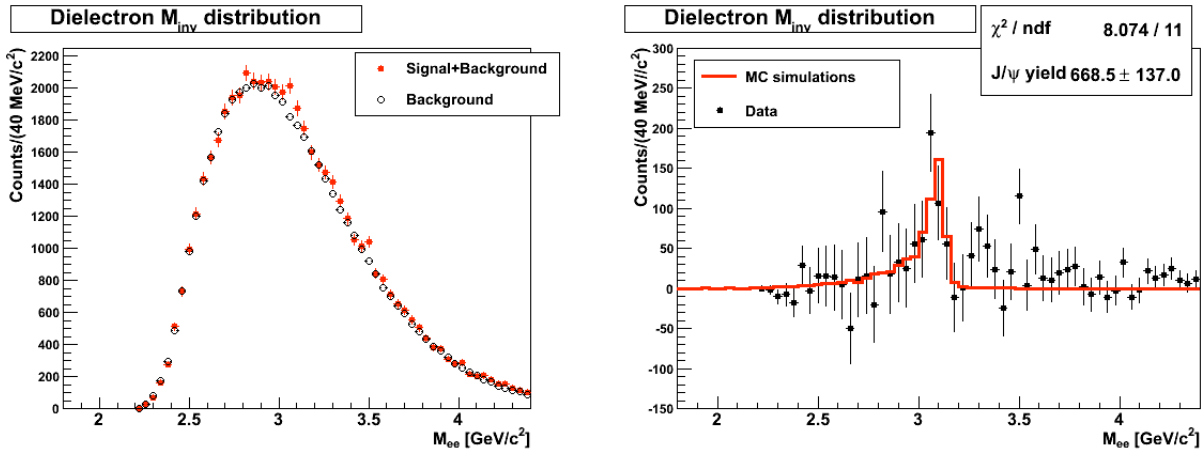

$1 < p_T^{J/\psi} < 2$ **GeV/c**

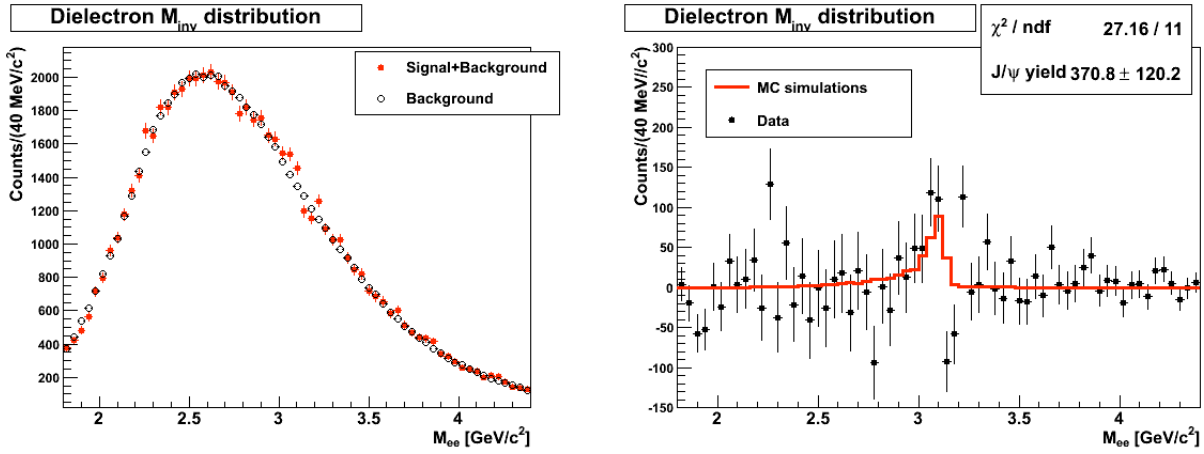

$2 < p_T^{J/\psi} < 5$ **GeV/c**

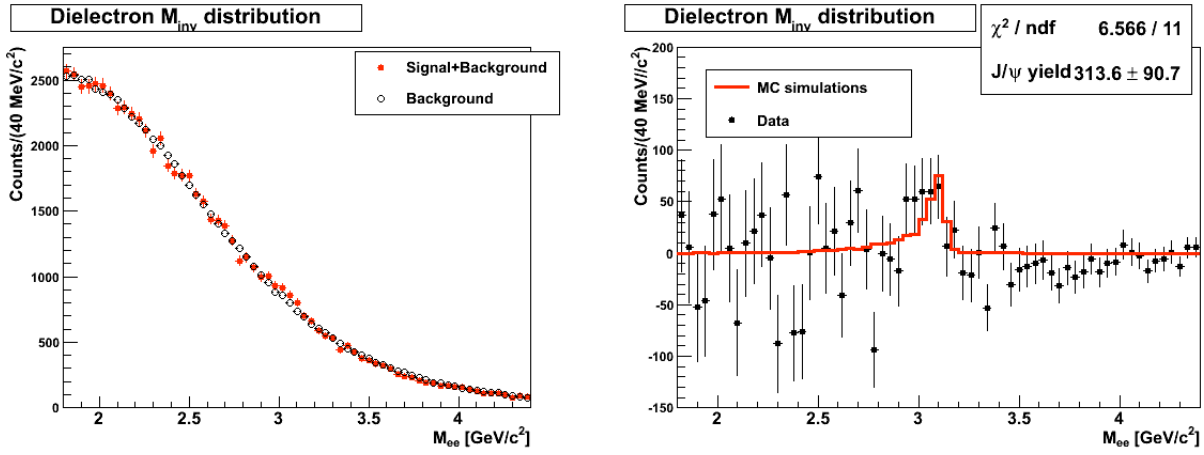

Figure 4.7: J/ψ signal and background in p_T bins in Au+Au minimum-bias collision. The background was obtained with event-mixing method described in the text and normalized in $1.8 < M_{inv} < 2.7$ GeV/c^2. Left: M_{inv} distribution before background subtraction; right: M_{inv} spectrum after background subtraction. The red line represents the Monte Carlo simulated J/ψ line shape fit. The results corrected for the trigger bias are shown.

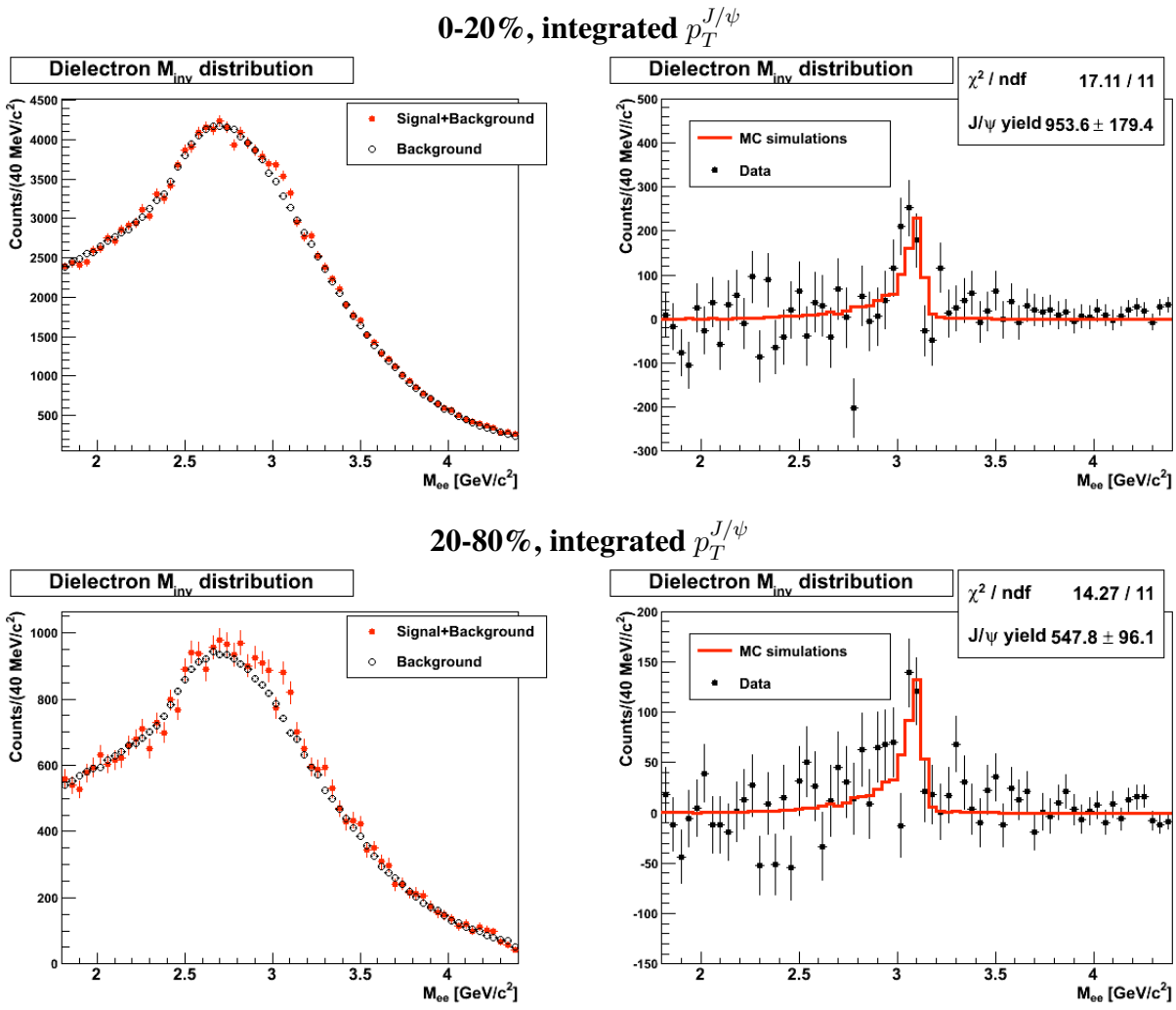

Figure 4.8: J/ψ signal and background in Au+Au collision with the centrality of 0–20% and 20–80%. The background was obtained with event-mixing method described in the text and normalized in $1.8 < M_{inv} < 2.7$ GeV/c^2. Left: M_{inv} distribution before background subtraction; right: M_{inv} spectrum after background subtraction. The red line represents the Monte Carlo simulated J/ψ line shape fit. The results corrected for the trigger bias are shown.

Residual background fitted in full M_{inv} range.

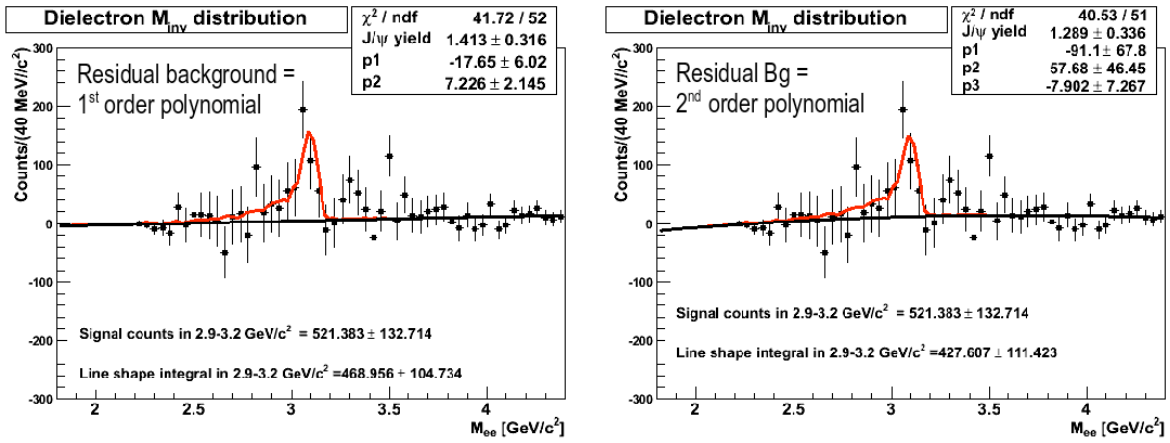

Residual background fitted in 2.4<M_{inv}< GeV/c^2.

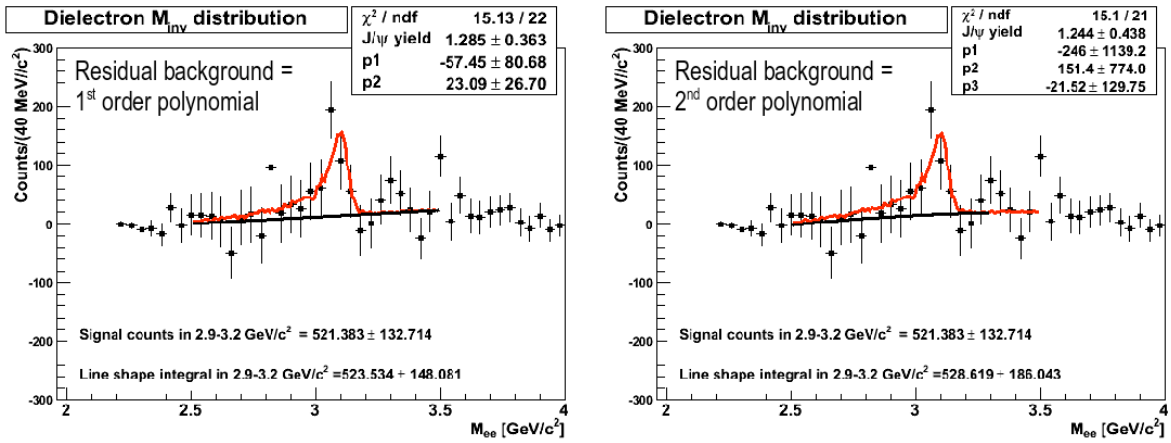

Figure 4.9: Residual background study in min-bias Au+Au collisions for $0 < p_T^{J/\psi} < 1$ GeV/c. The polynomials of 1^{st} and 2^{nd} order were used to fit the residual background. Upper raw: The results of the fit in full M_{inv} range, Lower row: results of the fit in 2.4<M_{inv}< GeV/c^2.

4.2 Efficiency correction

The reconstructed signal does not represent the total number of J/ψ produced in a given centrality, p_T and rapidity range ($|y| < 1$ in our case) and it has to be corrected for limited detector acceptance and reconstruction inefficiencies. The inefficiencies due to limited acceptance include finite phase-space covered by STAR detector (due to cuts on track p_T and pseudorapidity) and losses due to inactive space between TPC sectors (some track may travel almost parallel to these and will not be detected in TPC). The reconstruction inefficiencies includes losses due to track reconstruction, track quality cuts and electron identification. The assessment of the correction to J/ψ reconstruction and the method used to apply these corrections to the raw spectra is describe in this section.

4.2.1 Tracking efficiency and geometrical acceptance

The tracking efficiency and geometrical acceptance was estimated using embedding technique described in Sec. 3.6.1. This method provides full information about simulated and reconstructed variables, the reconstruction efficiency and acceptance $\epsilon_{A \times R}$ for a given rapidity and p_T bin can be calculated using formula:

$$\epsilon_{A \times R} = \frac{N^{J/\psi}_{Reconstructed}}{N^{J/\psi}_{Monte\ Carlo}} \tag{4.2}$$

where: $N^{J/\psi}_{Monte\ Carlo}$ - number of simulated J/ψ in a given rapidity and p_T interval, $N^{J/\psi}_{Reconstructed}$ - number of reconstructed J/ψ in the STAR TPC with applied track quality cuts, the same as used in real data analysis, which are summarized in Tab. 3.1. A J/ψ is counted as reconstructed if both daughters are reconstructed.

The input Monte Carlo p_T and rapidity distributions are flat to ensure that the statistics in all p_T and rapidity bins is similar and the statistical errors on efficiency are constant over whole p_T and y range. The uniform p_T and rapidity spectra have been used to save the computing time. The effects of different underlying distributions are assessed in Sec. 4.2.7.

Cu+Cu

Two different embedding samples were used in efficiency assessment:

- Production P05id - 101 thousand events passing a centrality and vertex position cuts (0-60%, $|V_z|$ <30 cm) with 10 J/ψ embedded per event. This is a large statistics sample

although it was produced with underestimated amount of material in the detector. Consequently the electron energy loss due to Bremsstrahlung is underestimated and the J/ψ line shape does not match the J/ψ peak in the experimental data set. The input J/ψ distributions cover $|y| < 1.5$ and p_T range of 0 - 5 GeV/c.

- Production P06id - 10 thousand events with 0-60% centrality and $|V_z|$ <30 cm. This is a low statistics sample although was produced with corrected amount of material in the detector. Consequently electron energy loss due to Bremsstrahlung was better handled and therefore J/ψ line shape in simulations matches the real data better. It is shown in Fig. 4.10 for minimum-bias Cu+Cu collisions: the fit to the real data gave $\chi^2/ndf \simeq 1.4$ for line shape in production P06id and $\chi^2/ndf \simeq 2$ for production P05id. In addition, p_T range was extended up to 10 GeV/c.

The tracking efficiency and acceptance $\epsilon_{A \times R}$ for both productions is compared in the Fig. 4.12. The results are consistent in spite of the limited statistics of P06ib sample. Because the higher statistics was available for P05id, this production was used to calculate the final $\epsilon_{A \times R}$. The difference in the amount of the material between these two samples was not significant to affect the tracking efficiency. However, the difference in J/ψ peak line shape is significant and we used the one from production P06ib to extract J/ψ yield.

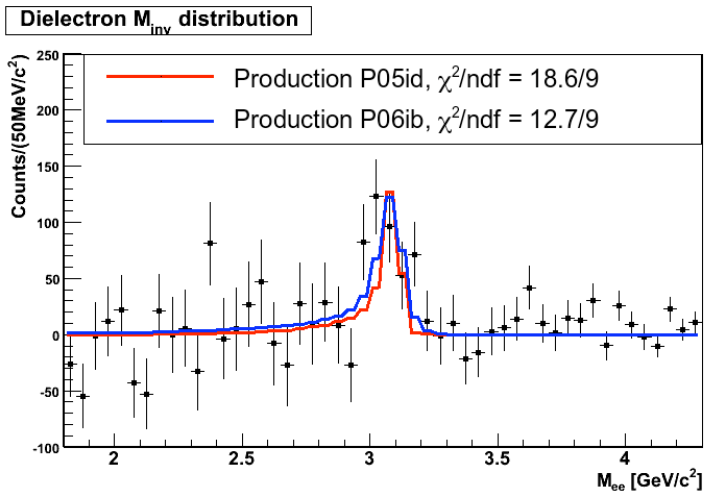

Figure 4.10: J/ψ signal in min-bias Cu+Cu collisions vs. line shape in two embedding samples: production P05id and production P06ib.

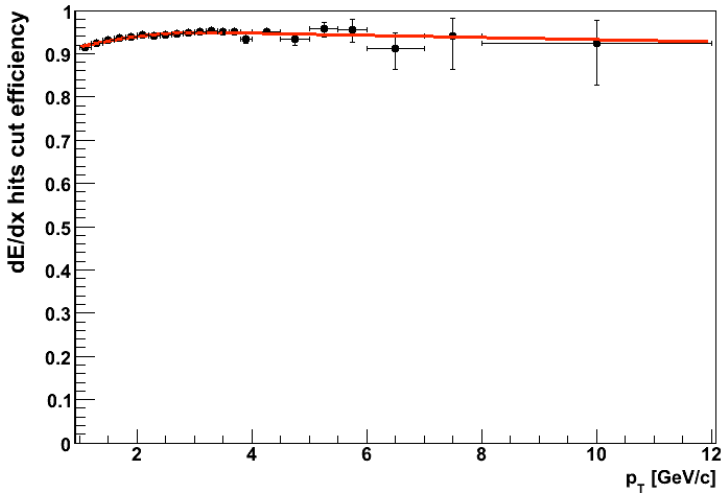

Figure 4.11: Single electron $ndE/dx\ Hits$ cut efficiency, red line denotes the Landau function and linear parametrization used to avoid fluctuation.

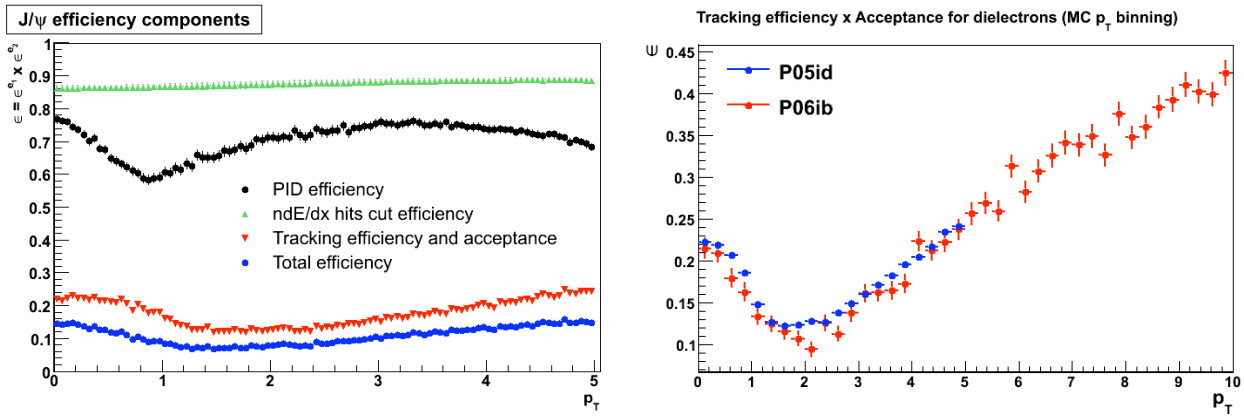

Figure 4.12: Left: summary of tracking efficiency, acceptance, PID and dE/dx hits cut contributions to overall J/ψ efficiency. Right: J/ψ tracking efficiency x acceptance efficiency for different embedding productions: P05id vs. P06ib.

Au+Au

The tracking efficiency and acceptance $\epsilon_{A\times R}$ was estimated based on sample of 22 thousand events with $|V_z| < 30$ cm and centrality of 0-80%. The total number of J/ψ was 60 thousand which were simulate within $|y| < 1.5$ and $p_T < 5$ GeV/c. The tracking efficiency depends on event multiplicity and this is clearly visible in Fig. 4.13: $\epsilon_{A\times R}$ is higher for more peripheral events, where the track density in the STAR TPC is lower.

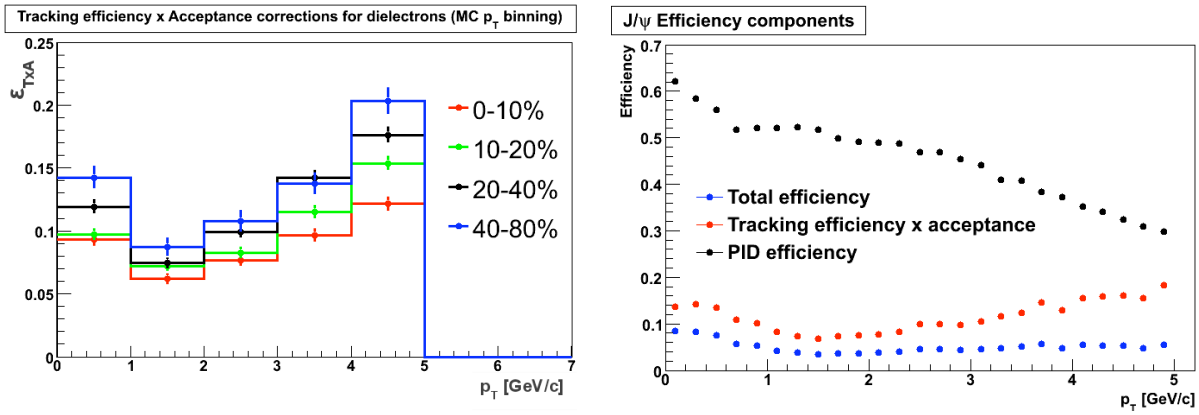

Figure 4.13: Left: tracking efficiency and acceptance for different centrality classes. Right: Overall J/ψ efficiency.

The shape of $\epsilon_{A\times R}(p_T)$ in Au+Au and Cu+Cu collisions is determined by kinematic cuts (mostly by cut on p_T of single electron). The J/ψ with $p_T^{J\psi} \simeq 0$ decays almost back-to-back (p_T vectors of daughters are anti-parallel) into two electrons with $p \simeq 1.5$ GeV/c^2. Then if the decay is in the STAR acceptance ($|\eta| < 1$) then there is high probability that the electron has p_T above the cut. For example if J/ψ's $p_T = 0$ then electrons have to have $|\eta| < 0.99$ to pass $p_T > 1.1$ GeV/c cut and $|\eta| < 0.82$ to pass $p_T > 1.2$ GeV/c cut. When the $p_T^{J\psi}$ increases, then the momentum of one of the daughter in the laboratory frame increases as well, but momentum of the second one in the laboratory frame decreases. Consequently the probability of both daughters passing p_T cut decreases and $\epsilon_{A\times R}(p_T)$ decreases as well, which is clearly visible in Fig. 4.12 (right panel) and Fig. 4.13 (left panel) for $p_T^{J\psi} < 2$ GeV/c. With further increase of $p_T^{J\psi}$, the p_T vectors of daughters in the laboratory frame become parallel and p_T of both electrons increases with increasing $p_T^{J\psi}$. This is reflected in the monotonic increases of $\epsilon_{A\times R}(p_T)$ for $p_T^{J\psi} > 2$ GeV/c.

4.2.2 J/ψ signal extraction efficiency

The Monte-Carlo simulations have shown that J/ψ peak has a long tail towards lower M_{inv} caused by electron Bremsstrahlung. In the real data analysis we had to limit M_{inv} range in which the raw yield was extracted. We estimated the efficiency of M_{inv} cut, $\epsilon_{M_{inv}}$, based on J/ψ line shape from embedding (which is presented in Fig. 4.1) and we found that $\epsilon_{M_{inv}} \approx 80\%$ for both Cu+Cu and Au+Au data.

4.2.3 dE/dx hits cut efficiency in Cu+Cu collisions

The dE/dx hits cut efficiency, $\epsilon_{nDedxHits}$, was calculated as a ratio of single track p_T spectrum with and without nDedxHits cut. This efficiency was estimated separately for each analyzed centrality class (0-60%, 0-20% and 20-60%). The example of obtained $\epsilon_{nDedxHits}(p_T^e)$ distribution for Cu+Cu minimum-bias events is presented in Fig. 4.11. To avoid statistical fluctuations, especially in high-p_T region, the efficiency was parametrized by Landau and linear function. The $\epsilon_{nDedxHits}(p_T^e)$ is high (above 90% for measured p_T range) and it depends slightly on p_T of the track: $\epsilon_{nDedxHits}(p_T^e)$ increases slowly from 92% at $p_T = 0$ to reach maximum ($\simeq 95\%$) at $p_T \simeq 3$ GeV/c and then it starts to decrease slowly above $p_T \simeq 6$ GeV/c.

4.2.4 The overall J/ψ reconstruction efficiency

The overall J/ψ reconstruction efficiency is a product of tracking efficiency and acceptance $\epsilon_{A\times R}(p_T^{J/\psi})$, single electron PID efficiency $\epsilon_{PID}(p^e)$ (described in Sec. 3.5) and, in the case of Cu+Cu collisions, also dE/dx hits cut efficiency $\epsilon_{nDedxHits}(p_T^e)$.

Then the overall J/ψ efficiency ϵ^{Total} for Au+Au collisions is given by:

$$\epsilon^{Total}(p_T^{J/\psi}) = \epsilon_{A\times R}(p_T^{J/\psi}) \times \epsilon_{PID}^{e_1}(p^{e_1}) \times \epsilon_{PID}^{e_2}(p^{e_2}) \times \epsilon_{M_{inv}} \tag{4.3}$$

For Cu+Cu collisions, ϵ^{Total} includes also $\epsilon_{nDedxHits}\,(p_T^e)$:

$$\begin{aligned} \epsilon^{Total}(p_T^{J/\psi}) &= \epsilon_{A\times R}(p_T^{J/\psi}) \times \epsilon_{PID}^{e_1}(p^{e_1}) \times \epsilon_{PID}^{e_2}(p^{e_2}) \\ &\quad \times \epsilon_{nDedxHits}(p_T^{e_1}) \times \epsilon_{nDedxHits}(p_T^{e_2}) \times \epsilon_{M_{inv}} \end{aligned} \tag{4.4}$$

J/ψ efficiency for Cu+Cu collisions together with its different components (tracking, PID and dE/dx hits cut efficiencies) is shown in Fig. 4.12 (left panel). The dE/dx hits cut efficiency for J/ψ (green points in Fig. 4.12) is almost independent on $p_T^{J/\psi}$ - it rises slightly with $p_T^{J/\psi}$.

The shape of PID efficiency for J/ψ reflects single electron $\epsilon_{PID}(p^e)$ - it decreases with $p_T^{J/\psi}$ due to cut used to reject protons to reach a minimum $p_T^{J/\psi} \sim 0.9$ Gev/c. Then the PID efficiency increases up to $p_T^{J/\psi} \simeq 3$ GeV/c and next decreases due to single electron efficiency loss at high electron momentum caused by cut on pion rejection. The average $\epsilon^{Total}(p_T^{J/\psi})$ is on the level of 10%.

The J/ψ reconstruction efficiency ϵ^{Total} together with its components (tracking and PID efficiencies) for minimum-bias Au+Au collisions is shown in Fig. 4.13 (right). The shape of the tracking efficiency $\epsilon^{Total}(p_T^{J/\psi})$ is determined by kinematic and PID cuts. The overall magnitude of $\epsilon^{Total}(p_T^{J/\psi})$ is smaller than in Cu+Cu because of much higher track densities in TPC and is on the level of 5% in minimum-bias Au+Au collisions.

4.2.5 Application of the corrections to the data

Usually to obtain the total number of J/ψ produced in a given p_T range, one has to obtain the raw signal spectra in p_T bins, then calculate the average correction factors for this p_T window and then correct the raw signal bin-by-bin for the estimated inefficiencies. However, the J/ψ reconstruction efficiency depends on $p_T^{J/\psi}$ and it changes significantly within p_T bins in which J/ψ signal was extracted. Moreover, available statistics allowed us to obtain p_T spectrum only for minimum-bias events, in narrower centrality classes only integrated signal was extracted. Therefore we decided to use a different method to apply correction factors, which was already employed in J/ψ analysis in Au+Au data recorded in 2004 [109].

This method is a version of a Monte Carlo integration algorithm. It consists of few basic steps [109]:

1. Extraction of p_T integrated raw yield $\mathrm{N}^{J/\psi}$ and associated statistical uncertainty $\Delta\mathrm{N}^{J/\psi}$ in a given invariant mass window for a selected centrality class. In the case of min-bias events, we also divided signal into p_T bins.

2. Extraction of the p_T spectrum of all e^+e^- pairs (which includes signal and background entries) in a given invariant mass window. This distribution has a fine binning (100 MeV/c per bin).

3. Yield correction

   Repeat over large number of iterations:

(a) Draw a number of J/ψ candidates, N^{Cand}, for a given round of corrections. We assumed that statistical uncertainties on the J/ψ yield ($\Delta N^{J/\psi}$) are Gaussian distributed. Then the N^{Cand} is randomly chosen from a Gaussian distribution with expected value equal $N^{J/\psi}$ and the variance equal $(\Delta N^{J/\psi})^2$. This step allows to propagate statistical uncertainty on $N^{J/\psi}$ to the next stage of the correction procedure.

(b) Randomly select N^{Cand} e^+e^- pairs from the p_T distribution obtained in step 2.

(c) For each pair find a correction factor $\epsilon^{Total}(p_T^{e^+e^-})$ corresponding to the p_T of the pair

(d) Find a corrected yield for a given iteration:

For each selected e^+e^- pair apply the correction factor to restore the number of produced J/ψ, n^{Prod}, corresponding to a measured pair with given $p_T^{e^+e^-}$:
$n^{Prod} = 1/\epsilon^{Total}(p_T^{e^+e^-})$.

Then the overall corrected yield is given by the sum of contributions from each of the selected pairs:

$$N^{J/\psi}_{corrected} = \sum_{i=1}^{N^{Cand}} n^{Prod} = \sum_{i=1}^{N^{Cand}} 1/\epsilon^{Total}(p_T^{e^+e^-}) \tag{4.5}$$

4. Extraction of the final corrected yield

$N^{J/\psi}_{corrected}$ collected in previous step has a Gaussian distribution and the example for minimum-bias Au+Au events is shown in Fig. 4.14. Then it is fitted by a Gaussian function and its mean value provides the most probable value of $N^{J/\psi}_{corrected}$ and the width of Gaussian function is a measure of uncertainty, $\Delta N^{J/\psi}_{corrected}$. $\Delta N^{J/\psi}_{corrected}$ includes the statistical error and also the systematic error due to used Monte Carlo algorithm [109]. A schematic view of the entire algorithm is shown in Fig. 4.14.

4.2.6 High-p_T contribution to integrated yield

To obtain a total number of produced J/ψ's (integrated over p_T), J/ψ yield beyond measured p_T range has to be estimated. We registered e^+e^- pairs with transverse momentum up to 5 GeV/c and we used results reported by the PHENIX experiment [74, 75] to estimate the yield of J/ψ with higher p_T. We fitted J/ψ p_T spectrum with a power-law parametrization, introduced in Sec. 3.7.3 in Eq. 3.27:

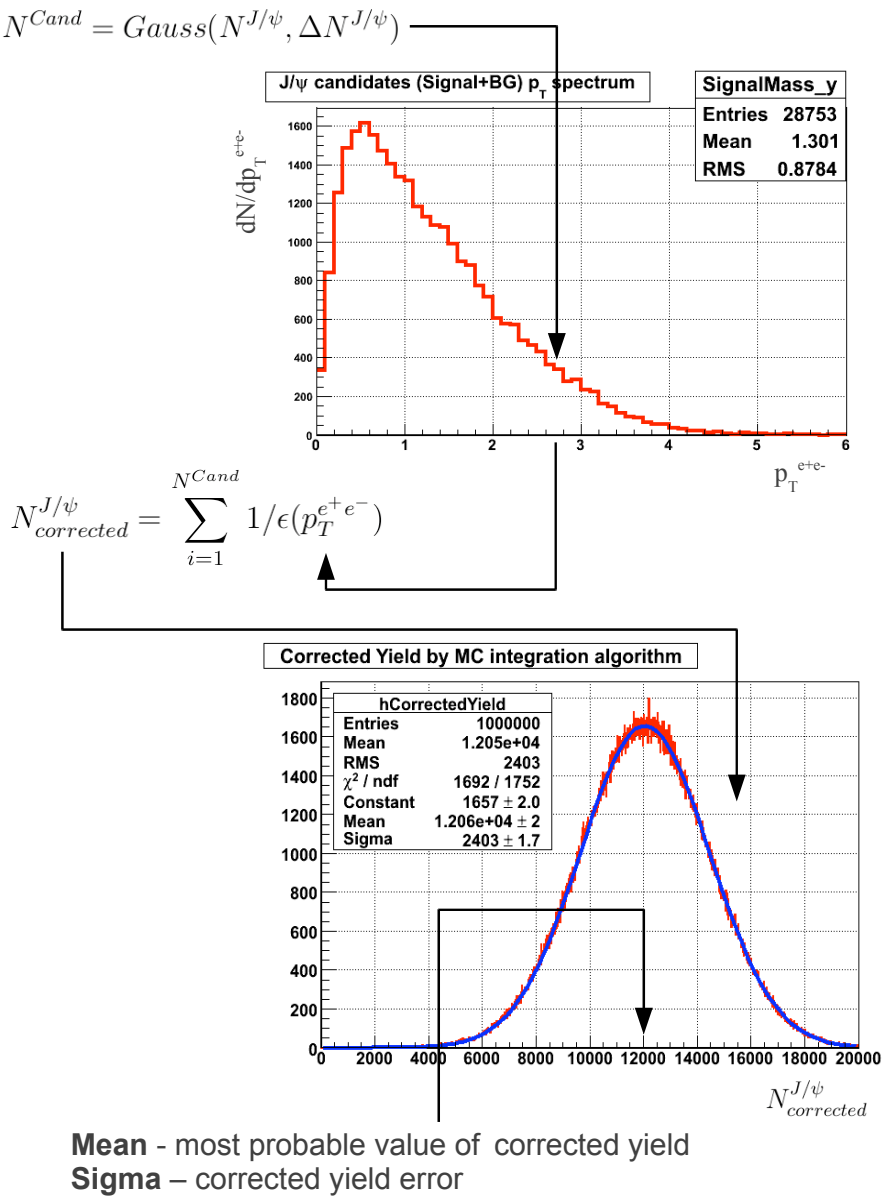

Figure 4.14: A schematic view of the Monte Carlo algorithm used in J/ψ yield correction for reconstruction inefficiencies, see Sec. 4.2.5 for details.

$$f(p_T) = A \cdot \left[1 + p_T^2/B^2\right]^C \tag{4.6}$$

The example of the fit for 0-20% most central Cu+Cu events is shown in Fig. 4.15. The fit quality in good ($\chi^2/ndf \leq 1$) and based on this fit we estimated that the contribution of high-p_T ($p_T > 5$ GeV/c) J/ψ to the total yield is small - on the level of 2%.

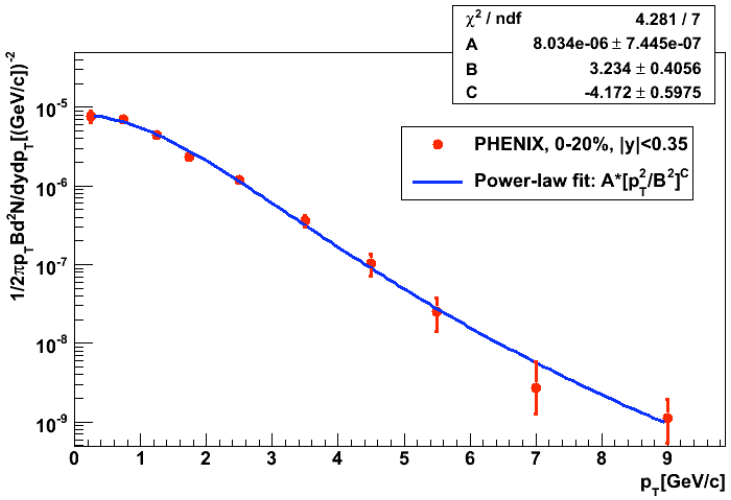

Figure 4.15: J/ψ p_T spectrum in 0-20% most central Cu+Cu collisions measured by the PHENIX experiment [74] with a power-law parametrization.

4.2.7 Reconstruction efficiency vs. shape of p_T and rapidity distribution

The shape of physical p_T and rapidity distributions can influence a correction due to reconstruction inefficiency in two ways. The first one is connected with finite p_T resolution: for a particular p_T range a number of J/ψ can be reconstructed outside given p_T bin due to resolution effects. The opposite effect is also possible - there may be J/ψ's which are reconstructed in particular p_T bin while the real transverse momentum is outside given bin.

The finite p_T and rapidity bin width introduces another problem. If a physical spectrum changes significantly within given bin, then the average efficiency can be overestimated or underestimated (depending on J/ψ yield distribution). This effect is stronger for wider bins.

To study those effects, we used *re-weighting* to quantify how the correction factors change for different underlying physical distributions. The p_T spectrum was weighted with a power-low parametrization, and the p_T weights $w^{p_T}(p_T)$ are given by:

$$w^{p_T}(p_T) = A \cdot p_T \cdot \left[1 + p_T^2/B^2\right]^{-6} \tag{4.7}$$

where A is an amplitude and B is related to $\langle p_T^2 \rangle$ of the distribution: $B^2 = 4\langle p_T^2 \rangle$ [110]. This function describes well J/ψ p_T spectrum in [110, 74, 75]. Formula 4.7 was fitted to PHENIX results in minimum-bias Cu+Cu and Au+Au collisions [74, 75].

On the other hand, the shape of rapidity distribution dN/dy is unknown in a range we used to measured J/ψ ($|y| < 1$). We assumed two extreme possibilities: flat dN/dy and one falling quickly with y. The latter was approximated by a Gaussian function:

$$w^y(y) = A \cdot e^{-\frac{y^2}{2\sigma^2}} \tag{4.8}$$

Where A is amplitude and σ^2 is a variance of the distribution.

To obtain the rapidity weights $w^y(y)$, we fitted function 4.8 to dN/dy spectrum reported by the PHENIX collaboration. We used results in 0-40% central Au+Au events [75] for our Au+Au studies. In the case of Cu+Cu, the dN/dy in $p + p$ at 200 GeV was employed [110] because the dN/dy in Cu+Cu was not available and the published results (nuclear modification factor vs. rapidity [74]) have shown that shape of dN/dy in Cu+Cu is similar to $p + p$.

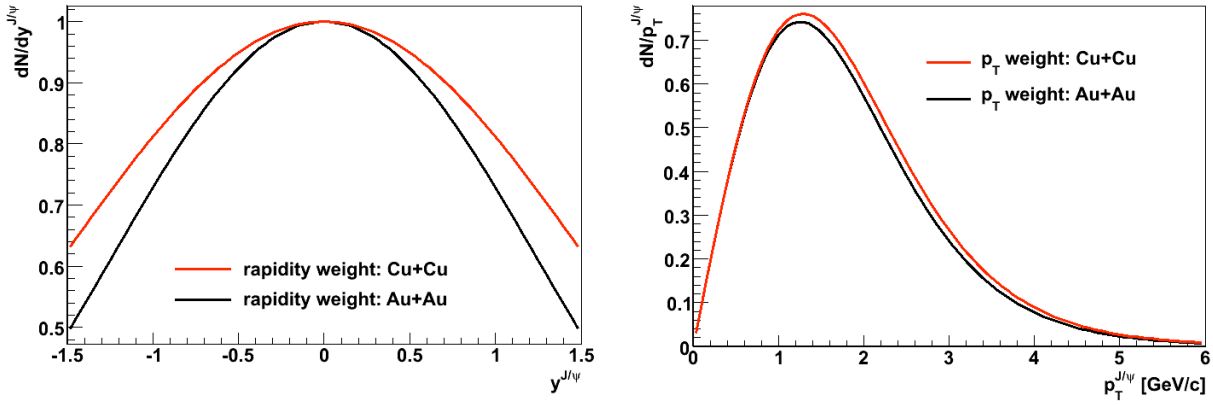

Figure 4.16: The p_T and y weights used in studies of the impact of the shape of p_T and rapidity distribution on efficiency corrections.

The distributions of p_T and rapidity weights are shown in Fig. 4.16. The dN/dy distribution is Cu+Cu is wider than this in Au+Au ($\sigma_{AuAu} = 1.26$ while $\sigma_{CuCu} = 1.55$). The p_T weight distribution for both systems look similar although the maximum is slightly shifted towards high p_T in Cu+Cu compared to Au+Au (which is reflected in value of B parameter in Eq. 4.7: $B_{AuAu} = 4.15$ while $B_{CuCu} = 4.25$).

Each Monte Carlo and reconstructed J/ψ was weighted by $w^y(y^{J/\psi})$ and $w^{p_T}(p_T^{J/\psi})$ corresponding to its rapidity and p_T respectively. Then the tracking efficiency and acceptance $\epsilon_{T\times A}$

with re-weighting for a given p_T and rapidity bin is given by

$$\epsilon_{T\times A}^{weighted} = \frac{\sum_{j=1}^{N^{Reco}} w_j^y(y^{J/\psi}) \cdot w_j^{p_T}(p_T^{J/\psi})}{\sum_{i=1}^{N^{MC}} w_i^y(y^{J/\psi}) \cdot w_i^{p_T}(p_T^{J/\psi})} \tag{4.9}$$

where w^y and w^{p_T} are p_T and rapidity weights, the denominator is a weighted sum of Monte Carlo J/ψ and the nominator denotes weighted sum of reconstructed J/ψ in a given bin.

In general, the effects of p_T resolution and the shape of underlying p_T distribution are expected to be small because the bin width in J/ψ p_T spectrum (1 GeV/c or wider) is significantly larger than p_T resolution ($\Delta p_T/p_T \simeq 1\% - 2\%$ for single electron in Cu+Cu, see Fig. 2.6), and the application of the correction to the raw spectra is carried out in small p_T bins (100 MeV/c). Therefore the efficiency changes only slightly between adjacent bins. On the other hand, the rapidity window is wide ($\Delta y = 2$) and a change of the underlying dN/dy spectrum causes significant change in the results.

This analysis shows that the shape of underlying distribution affects only slightly $\epsilon_{T\times A}$ in Cu+Cu collisions: the results obtained whit flat and re-weighted distribution differ by $\approx 2\%$. On the other hand, the effect in Au+Au collisions is slightly stronger, on the level of 3–4%, which is caused by narrower rapidity spectrum in Au+Au compared to Cu+Cu data.

The difference between results of $\epsilon_{T\times A}$ calculation with flat and re-weighted p_T and y spectra was included in the systematic error assessment discussed in section 4.3.

4.3 Systematic uncertainties assessment and consistency check

In this chapter assessment of systematic uncertainties is presented. We followed the spirit of a systematic error analysis proposed in [111] and divided out studies into two stages:

1. Consistency check: we varied cuts in the analysis to check if obtained results are not biased by choice of selection criteria.

2. Systematic uncertainties evaluation: we studied the uncertainties on estimation (or modeling) of unknown physical quantities in our analysis, such as reconstruction efficiency, combinatorial background etc.

4.3.1 Consistency check

Although the cuts used in our analysis were chosen in Monte Carlo studies and they are unlikely to be biased, it is wise to crosscheck the results against any systematic mistake. We performed a set of consistency checks, where we varied the kinematic cuts (p_T, DCA and nDedxHits or nFitPts) in the range listed in Tab. 4.5 for Cu+Cu and Tab. 4.6 for Au+Au data. For every check we applied all needed correction to a given set of cuts. In the case of Au+Au collisions, the procedure was carried on with the data before correction for the trigger bias. This correction is computationally expensive and it was not feasible to apply it for every tested set of cuts. Moreover, with the given signal yield (a few hundreds of J/ψ) the correction changes only the overall normalization but not the relative difference between results. Such approximation would not hold if the signal is very small because of possible fluctuations which could be enhanced by re-weighting described in Sec. 4.1.1.

The different cuts change the signal and background yields. Therefore, the fluctuations would be also different as well as the obtained number of J/ψ. However, if the results are consistent, the differences resulting from a change of the cuts should not be included in systematic error as they arise from the statistical fluctuations. Moreover, the shape of combinatorial background changes with kinematic cuts, analyzed p_T range and also with centrality class. Consequently, we used two methods to normalize event-mixing background in this study (in low M_{inv} range ($1.8 < M_{inv} < 2.7$ GeV/c^2) and to the integral of like-sign background) to identify if the observed discrepancy is due to choice on normalization factor i.e. is a systematic error.

For both Cu+Cu and Au+Au data the obtained results were consistent within statistical error (one standard deviation) and within the systematic uncertainty of the normalization of the event-

mixing background. The performed tests gave us a high level of confidence that our results are not bias by the choice of kinematic cuts.

Table 4.5: Kinematic cuts used in the consistency check in Cu+Cu collisions.

Dca cut [cm]	p_T cut [GeV/c]	ndEdxHits cut
<1	>1	≥ 18
<1	>1.05	≥ 18
<1	>1.1	≥ 18
<1	>1.1	≥ 20
<1	>1.2	≥ 18
<1.5	>1.1	≥ 18
<2	>1.1	≥ 18

Table 4.6: Kinematic cuts used in the consistency check in Au+Au collisions

Dca cut [cm]	p_T cut [GeV/c]	nFitPts cut
<1	>1.2	≥ 25
<1	>1.1	≥ 25
<1	>1.3	≥ 25
<1.5	>1.2	≥ 25
<1.0	>1.2	≥ 23

4.3.2 Systematic uncertainties

In general, systematic uncertainties arise due to imperfect knowledge about given physical quantity, which we have to model to obtain the final physical observable. We assessed and assigned these uncertainties to every part of our analysis in which we had to make an assumption about given physical quantity (for example, a combinatorial background). In this section we summarize the main sources of systematic uncertainties. It should be notice that scope of systematic uncertainties study and obtained precision were limited by available statistics.

Main sources of systematic errors:

1. Single electron identification efficiency estimation

   The mains source of the error is the choice of constraints in multi-Gaussian fit used in ϵ_{PID} assessment. The procedure to estimate uncertainties on ϵ_{PID} efficiency was described in Sec. 3.5.1. As a results, we obtained a central value of $\epsilon_{PID}^{cent}(p^e)$ and assigned values of upper and lower errors ($\Delta\epsilon_{PID}^{up}(p^e)$ and $\Delta\epsilon_{PID}^{down}(p^e)$). We propagated these errors to final results by using $\epsilon_{PID}(p^e) = (\epsilon_{PID}^{cent}(p^e) - \Delta\epsilon_{PID}^{down})(p^e)$ and $\epsilon_{PID}(p^e) = (\epsilon_{PID}^{cent} + \Delta\epsilon_{PID}^{up})(p^e)$ in the correction for J/ψ reconstruction inefficiencies. The systematic error is rather small: $\pm(2-3)\%$ in Cu+Cu and $\pm 1.5\%$ in Au+Au data.

2. Raw J/ψ yield extraction

   This is caused by difference in results obtained using two possibles methods of raw yield extraction: bin counting in J/ψ mass range and an integral of the Monte Carlo line shape.

3. Different methods of background normalization for event-mixing technique

   If the shapes of background obtained with the event-mixing technique and the real data background are different, then the choice of a normalization region influences the overall magnitude of the background. This causes uncertainty in the extracted yield on the level of $\sim$20% in Cu+Cu and 10-90% in Au+Au data.

4. Invariant mass range used in the yield calculation

   We extracted additionally the raw yield in the extended window of invariant mass ($2.8 < \mathrm{M_{inv}} < 3.2$ GeV/c^2). The difference in final yield, compared to the mass range used in our analysis ($2.9 < \mathrm{M_{inv}} < 3.2$ GeV/c^2), was found to be negligible (less than 1% for both data sets).

5. Shape of underling p_T and rapidity distributions used in efficiency assessment.

This systematic error was found to be rather small: 2.5% for Cu+Cu and 3–4% for Au+Au data.

6. Extraction of J/ψ yield beyond measured p_T range
   We estimate this error by changing a function used to describe p_T spectra reported by the PHENIX experiment. This error is negligible – less than 1% for both Cu+Cu and Au+Au data.

7. Track reconstruction efficiency
   The error is introduced if number of simulated hits for a track in TPC is different then the real one. We assumed that the number of real and simulated hits can differ by ± 1 point in TPC. Then we calculated the efficiency for such cases and we applied overestimated (underestimated) correction factors to the raw yield. We found that for long tracks used in our studies (nHits or nFitPts ≥ 25) the error is 2–3% in Cu+Cu and 3–5% in Au+Au events.

8. Shape of residual background used in J/ψ yield extraction in Au+Au collisions
   As it was described in Sec. 4.1.2, we quantified possible residual background using first and second order polynomials. The difference in a yield was ∼20% on p_T spectrum for min-bas events, 8% for top 20% central events and 26% for peripheral events. The uncertainty is caused by sizable statistical errors in the invariant mass spectrum which translates to errors on fitted parameters.

9. Correction for the trigger bias in Au+Au collisions
   The re-weighting procedure, described in Sec. 3.2.2, requires normalization of Monte Carlo gRefMult distributions to real data in a given range of gRefMult. We varied the normalization window and found that the difference in final corrected J/ψ yield is negligible (less than 0.5%).

We assumed that aforementioned systematic errors are not correlated and we obtained the final systematic uncertainty by adding them in quadratures.

The systematic error summary for Cu+Cu data is presented in Tab. 4.7. The biggest sources of systematic error are method of raw yield extraction and normalization of event-mixing background.

The overall systematic uncertainty for Au+Au collisions are shown in Tab. 4.8. The largest

source of error are attributed to the normalization of event-mixing background, shape of residual background and method used to of extract raw yield.

All contributions to the systematic uncertainties for Au+Au and Cu+Cu data are presented in Appendix A.

Table 4.7: Summary of systematic error on J/ψ yield in Cu+Cu collisions

Centrality	J/ψ p_T **range [GeV/c]**	**Error -**	**Error +**
0-60%	integrated	14%	19%
0-60%	0-1	26%	33%
0-60%	1-5	16%	14%
0-20%	integrated	20%	26%
20-60%	integrated	14%	5%

Table 4.8: Summary of systematic error on J/ψ yield in Au+Au collisions

Centrality	J/ψ p_T **range [GeV/c]**	**Error -**	**Error +**
0-80%	0-1	51%	5%
0-80%	1-2	20%	91%
0-80%	2-5	4%	32%
0-20%	integrated	10%	7%
20-80%	integrated	28%	21%

4.4 Results

We have studied the J/ψ momentum distribution by calculating the invariant cross section $\frac{B_{ee}}{2\pi p_T}\frac{\mathrm{d}^2 N_{J/\psi}}{\mathrm{d}y\mathrm{d}p_T}$:

$$\frac{B_{ee}}{2\pi p_T}\frac{\mathrm{d}^2 N_{J/\psi}}{\mathrm{d}y\mathrm{d}p_T} = \frac{1}{2\pi p_T \Delta p_T \Delta y}\frac{N^{Corr}_{J/\psi\to e^+e^-}}{N_{event}} \tag{4.10}$$

where B_{ee} is the $J/\psi \to e^+e^-$ branching ratio, N_{event} is the number of events in a given centrality class, $N^{Corr}_{J/\psi\to e^+e^-}$ - the measured J/ψ yield corrected for all inefficiencies listed in previous sections, Δp_T and Δy are the traverse momentum and rapidity intervals respectively ($\Delta y = 2$ in our studies). $\frac{B_{ee}}{2\pi p_T}\frac{\mathrm{d}^2 N_{J/\psi}}{\mathrm{d}y\mathrm{d}p_T}$ represents the J/ψ density per event for a given centrality class.

We reported the results of the J/ψ yield measurements over bins of finite width (1 GeV/c or wider). It was shown in [112] that neither the central value of the bin nor the weighted mean value of the yield within the bin is the appropriate place to plot the data point in order to compare with theoretical or model distributions. Instead, such data points should to appear where the value of the predicted function is equal to its mean value over the wide bin:

$$f(p_T^{\mathrm{Plot}}) = \frac{1}{\Delta p_T}\int_{p_T^{(1)}}^{p_T^{(2)}} f(p_T)\mathrm{d}p_T \tag{4.11}$$

where p_T^{Plot} is the value at which the measurement should be plotted to correctly represents a given distribution $f(p_T)$, $p_T^{(1)}$ and $p_T^{(2)}$ are the lower and upper bin edges, and Δp_T is the bin width. A disadvantage of this approach is that an assumption has to be made about $f(p_T)$. We assumed that the $f(p_T)$ has a power-law form $f(p_T) = A \cdot p_T \cdot (1 + (p_T/B)^2)^{-6}$, where the parameters were obtained by a fit to the J/ψ p_T spectrum in minimum-bias Au+Au and Cu+Cu collisions [74, 75]. The values of p_T^{Plot} were then obtained by numerically solving Eq. 4.11 for studied p_T bins.

The transverse momentum spectra of J/ψ in Cu+Cu and Au+Au minimum bias collisions are presented in Fig. 4.17. The statistical errors are indicated by the error bars and the systematic errors are represented by the brackets. The STAR results are compared to previously published data by the PHENIX experiment [74, 75]. The spectra reported here were measured in a wider rapidity interval ($|y| < 1$) compared to the PHENIX (($|y| < 0.35$). The results are consistent within errors, which provides an important independent crosscheck to the published data. The

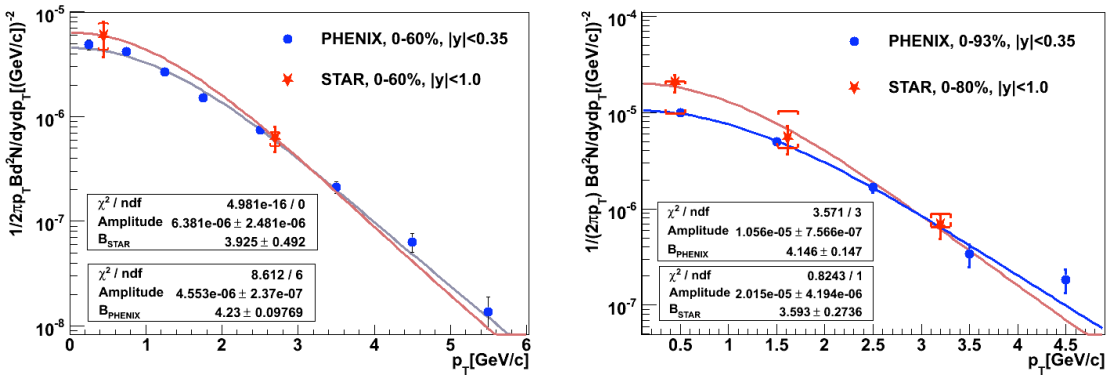

Figure 4.17: J/ψ p_T spectrum in minimum bias Cu+Cu (left) and Au+Au (right) collisions, compared to the results reported by the PHENIX experiment. The bars represent statistical error and the brackets systematic errors. The curves are power low fits to the STAR (red line) and PHENIX (blue line) results.

lines in Fig. 4.17 are power-law fits given by

$$\frac{B_{ee}}{2\pi p_T}\frac{\mathrm{d}^2 N_{J/\psi}}{\mathrm{d}y\mathrm{d}p_T} = A \cdot (1 + (p_T/B)^2)^{-6} \tag{4.12}$$

The shape of the p_T spectrum in Au+Au collisions differs slightly between STAR and PHENIX results. Since the parameter B is related to $\langle p_T \rangle$ as $B^2 = 4\langle p_T^2 \rangle$, we used this relation to extract a value for $\langle p_T^2 \rangle$. For Cu+Cu, the value for STAR and PHENIX are $\langle p_T^2 \rangle_{STAR} = 3.9 \pm 1.0$ GeV^2/c^2 and $\langle p_T^2 \rangle_{PHENIX} = 4.5 \pm 0.2$ GeV^2/c^2 respectively, while for Au+Au we obtained $\langle p_T^2 \rangle_{STAR} = 3.2 \pm 0.5$ GeV^2/c^2 and $\langle p_T^2 \rangle_{PHENIX} = 4.3 \pm 0.3$ GeV^2/c^2, respectively. Only the statistical errors were included in the fit.

In Tab. 4.9 and 4.10 we report the integrated yields $B_{ee} \cdot \mathrm{d}N_{J/\psi}/\mathrm{d}y$ for different centrality classes of Cu+Cu and Au+Au collisions. Due to limited statistics in the case of semi-peripheral Cu+Cu collisions (0-60%), we were able to estimate only an upper limit for the J/ψ yield.

We used these values to calculate the nuclear modification factor R_{AA}, reported in next chapter.

Table 4.9: Mid-rapidity ($|y| < 1$) integrated yields in Cu+Cu collisions. For semi-peripheral events (20-60%), a 95% confidence level upper limit is quoted.

Centrality	$B_{ee}\frac{\mathrm{d}N_{J/\psi}}{\mathrm{d}y}$	$\pm$ stat. error	syst. error
0-20%	1.56×10^{-4}	3.64×10^{-5}	$^{+4.95\times10^{-5}}_{-3.21\times10^{-5}}$
20-60%	3.89×10^{-5}	95 % C.L.	$^{+1.75\times10^{-6}}_{-5.55\times10^{-6}}$

Table 4.10: Mid-rapidity ($|y| < 1$) integrated yields in Au+Au collisions

Centrality	$B_{ee}\frac{\mathrm{d}N_{J/\psi}}{\mathrm{d}y}$	$\pm$ stat. error	syst. error
0-20%	5.23×10^{-4}	9.46×10^{-5}	$^{+3.70\times10^{-5}}_{-5.30\times10^{-5}}$
20-80%	7.49×10^{-5}	1.28×10^{-5}	$^{+1.58\times10^{-6}}_{-2.10\times10^{-6}}$

Chapter 5

Nuclear modification factor study

J/ψ is considered to be an excellent probe to study the properties of Quark-Gluon Plasma. To study the J/ψ interaction with a medium, charmonium production in nucleus+nucleus collisions is compared to the production in $p+p$. Then, using models or theoretical calculations, we try to deduce the properties of the medium based on the modification of the properties of the probe, J/ψ in this case.

The modification of particle production in the medium is quantified by the nuclear modification factor R_{AA}, which, as a function of p_T, is given by the ratio of particle production in nucleus-nucleus collisions $\left(\frac{\mathrm{d}^2N^{A+A}}{\mathrm{d}y\mathrm{d}p_T}\right)$ in a given centrality class, to the production rate in elementary (proton-proton) collisions $\left(\frac{\mathrm{d}^2N^{p+p}}{\mathrm{d}y\mathrm{d}p_T}\right)$, scaled by the mean number of binary collisions in the reaction N_{coll}:

$$R_{AA}(p_T) = \frac{\frac{\mathrm{d}^2N^{A+A}}{\mathrm{d}y\mathrm{d}p_T}}{\langle N_{coll}\rangle \frac{\mathrm{d}^2N^{p+p}}{\mathrm{d}y\mathrm{d}p_T}} \tag{5.1}$$

The J/ψ production in $p+p$ collisions is reported in literature as a differential cross-section $\frac{\mathrm{d}^2\sigma^{J/\psi}_{p+p}}{\mathrm{d}y\mathrm{d}p_T}$, and it allow us to obtain the invariant yield $\frac{\mathrm{d}^2N^{p+p}}{\mathrm{d}y\mathrm{d}p_T}$ as follows:

$$\frac{\mathrm{d}^2N^{p+p}}{\mathrm{d}y\mathrm{d}p_T} = \frac{\frac{\mathrm{d}^2\sigma^{J/\psi}_{p+p}}{\mathrm{d}y\mathrm{d}p_T}}{\sigma_{p+p}} \tag{5.2}$$

where $\sigma_{p+p} = 42 \pm 3$ mb is the cross-section of inelastic $p+p$ collisions.

R_{AA} is also used to quantify the in-medium modification of the production rates as a function of centrality of the collision, represented by the number of participants, N_{part}. For a given colliding system and a colliding energy, the centrality dependence reflects an evolution of R_{AA} with energy density. R_{AA} for a given centrality class, corresponding to a particular number of

binary collisions and participants, is given by:

$$R_{AA} = \frac{\frac{\mathrm{d}N^{A+A}}{\mathrm{d}y}}{\langle N_{coll} \rangle \frac{\mathrm{d}N^{p+p}}{\mathrm{d}y}} \tag{5.3}$$

The number of binary collisions and the number of participants were calculated within the framework of a Monte Carlo Glauber model and are presented in Tab 5.1 and 5.2 for Au+Au and Cu+Cu centrality classes respectively.

Table 5.1: The average number of binary collisions and participants for centrality classes of Au+Au collisions.

Centrality	$\langle N_{coll} \rangle$	$\langle N_{part} \rangle$
0-20%	765^{+64}_{-60}	280^{+7}_{-7}
20-80%	136^{+25}_{-20}	75^{+9}_{-7}
0-80%	239^{+29}_{-35}	126^{+7}_{-8}

Table 5.2: The average number of binary collisions and participants for centrality classes of Cu+Cu collisions.

Centrality	$\langle N_{coll} \rangle$	$\langle N_{part} \rangle$
0-20%	156^{+11}_{-12}	87^{+1}_{-1}
20-60%	43^{+2}_{-3}	34^{+1}_{-1}
0-60%	80^{+6}_{-6}	51^{+1}_{-1}

In our studies we used the J/ψ differential cross sections $\frac{\mathrm{d}\sigma^{J/\psi}_{p+p}}{\mathrm{d}y}$ and $\frac{\mathrm{d}^2\sigma^{J/\psi}_{p+p}}{\mathrm{d}y\mathrm{d}p_T}$ reported by the STAR experiment [89] to calculate R_{AA}. For the sake of comparison, we also used $\frac{\mathrm{d}^2\sigma^{J/\psi}_{p+p}}{\mathrm{d}y\mathrm{d}p_T}$ from PHENIX [110] to calculate $R_{AA}(p_T)$.

5.1 Results

Figure 5.1 shows the nuclear modification factor as a function of transverse momentum for minimum-bias Cu+Cu and Au+Au collisions. STAR results are compared to those reported by the PHENIX experiment. We present results calculated with STAR and PHENIX reference spectra. The boxes about unity on the right show the R_{AA} normalization uncertainty, which is

the quadrature sum of the of p+p normalization uncertainty and uncertainty in the number of binary collision. The STAR results are consistent with those reported by PHENIX, which is an important crosscheck, as they were obtained in a broader rapidity window ($|y| < 1$) compared to PHENIX ($|y| < 0.35$). The statistical errors are substantial but they are mainly caused by the uncertainties in the reference spectra: the uncertainties are smaller in the case when the PHENIX reference spectrum was used (see the difference between red and blue star symbols in Fig. 5.1).

The $R_{AA}(p_T)$ results were compared to predictions from a few theoretical models. Two of them, the Charmonium transport model [113] and the so-called Two-Component model [60, 114], describe the rising trend seen in Cu+Cu collisions. Figure 5.1 shows the comparison of STAR data with the latter. The Two-Component model is a phenomenological approach in which various aspects of the J/ψ interaction with a medium were incorporated: dissociation due to color screening, hadronic phase dissociation, statistical $c\bar{c}$ coalescence, J/ψ formation time effects and also B-hadron feeddown. The rising trend was reproduced when the formation time and the feeddown effects were introduced. The transverse momentum dependence of J/ψ production in the Charmonium transport model is studied by solving the transport equation for J/ψ motion, while the medium evolution is obtained in a framework of ideal hydrodynamic. Both the initial J/ψ production and its regeneration are taken into account. Due to limited statistics, we are currently unable to distinguish between these two models.

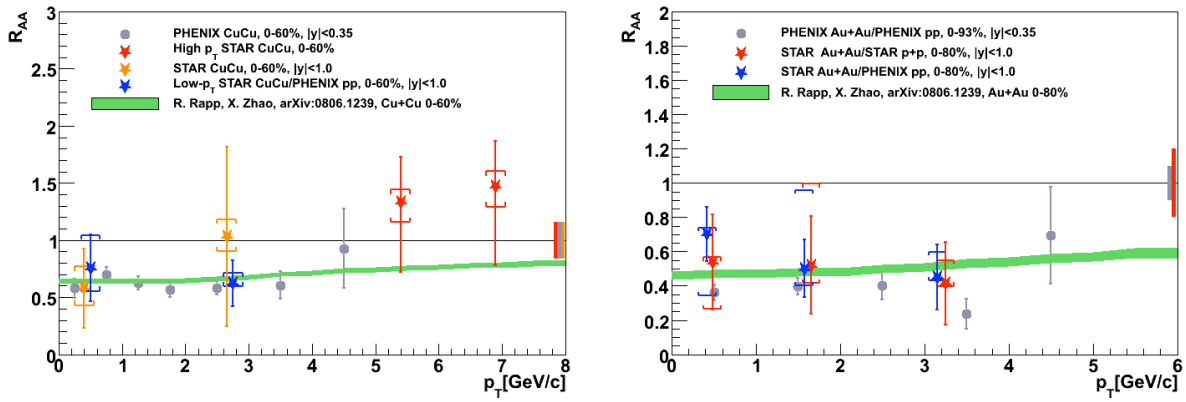

Figure 5.1: Nuclear modification factor as a function of transverse momentum in minimum-bias Cu+Cu (left) and Au+Au (right) collisions compared to results reported by PHENIX and Two-Component model [60, 114]. The bars represent statistical error, brackets - systematic error, and the boxes about unity on the right show the R_{AA} normalization uncertainty. The green band shows the uncertainties in the model.

Figures 5.2 – 5.4 show the nuclear modification factor as a function of event centrality (represented by the number of participants, N_{part}) for Cu+Cu and Au+Au collisions and its comparison with different scenarios of the J/ψ in-medium interaction. In the case of Cu+Cu, the limited statistics only allows a 95% confidence level upper limit estimate for semi-peripheral collisions. STAR and PHENIX results agree within uncertainties. Figure 5.2 shows the comparison with the aforementioned Two-Component model [60, 114]. Figure 5.3 presents results from the calculations which assumed only cold nuclear matter effects (nuclear absorption and shadowing) [115] - the curves represent different shadowing parametrizations and different values of a nuclear absorption cross section σ_{abs}. Figure 5.4 shows the predictions of the Co-mover Interaction Model (CIM) [116]. In CIM, the charmonium dissociation is caused by the interactions with the co-moving nuclear medium. This model includes the initial-state nuclear effects and secondary J/ψ production through the recombination of $c\bar{c}$ pairs.

All presented models describe the data relatively well. Due to limited statistics, at the moment we are not able to distinguish between the presented scenarios of J/ψ suppression.

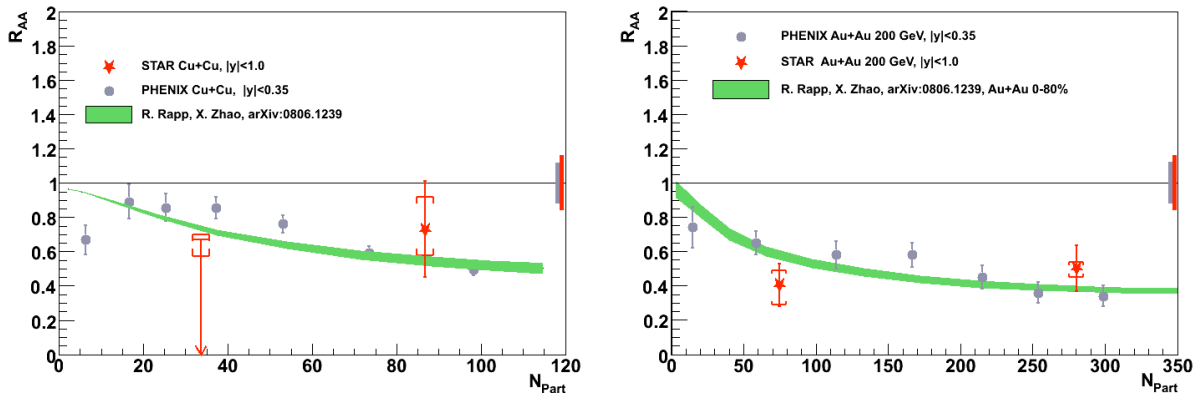

Figure 5.2: Nuclear modification factor as a function of centrality in Cu+Cu (left) and Au+Au (right) collisions compared to results reported by PHENIX and the Two-Component model. The bars represent statistical error, brackets - systematic error, and the boxes about unity on the right show the R_{AA} normalization uncertainty.

5.2 Summary

We have reported a first measurement of the nuclear modification factor for low-p_T J/ψ at STAR. The R_{AA} as a function of transverse momentum and collision centrality has been presented. Strong J/ψ suppression in Au+Au collisions is observed and a good agreement with

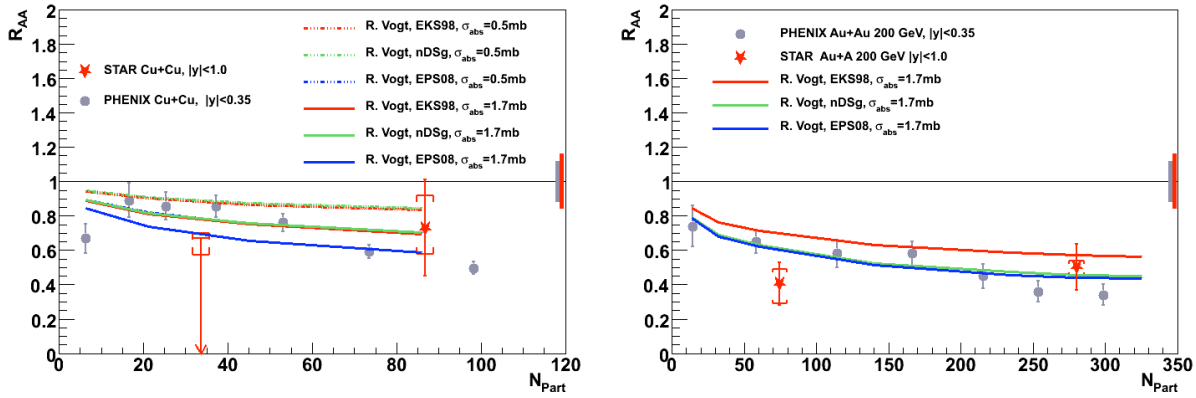

Figure 5.3: Nuclear modification factor as a function of centrality in Cu+Cu (left) and Au+Au (right) collisions compared to the results reported by PHENIX and predictions for R_{AA} from cold matter effects only (shadowing and nuclear absorption).

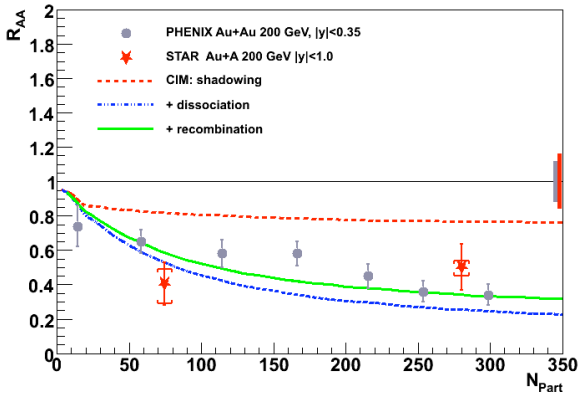

Figure 5.4: Nuclear modification factor as a function of centrality in Au+Au collisions compared to the results from the Co-mover Interaction Model (CIM) [116].

published results by the PHENIX experiment is seen in spite of limited statistics from STAR. It is an extremely important experimental cross check as these two analyses were carried out using completely different detectors, different analysis techniques, and operated in a different rapidity range.

Presently, STAR has accumulated a large sample (300 million) of Au+Au minimum-bias events at $\sqrt{s_{NN}} = 200$ GeV. Since the SSD and SVT detectors were removed from the STAR detector, it is expected that the combinatorial background due to γ conversion on SSD and SVT material will be significantly reduced. Therefore it is expected that the low-p_T J/ψ spectra will be measured with a statistical precision of 5% [117]. This work outlines the fundamental strategy for the future analysis of J/ψ production with the STAR detector. The software and the methods developed during the studies reported here, particularity the algorithms for finding optimal cuts, the efficiency assessment and systematic uncertainties studies, will provide important tools and a knowledge for charmonium study in the future.

Chapter 6

J/ψ elliptic flow

6.1 Anisotropic flow

A convenient and a model-independent way to study the flow phenomena is the Fourier analysis of a particle azimuthal distribution on event-by-event basis in narrow rapidity windows. The triple differential momentum distribution can be factorized as follows [118]:

$$E\frac{d^3N}{d^3p} = \frac{1}{2\pi}\frac{d^2N}{p_T dp_T dy}\left(1 + \sum_{i=1}^{\infty} 2v_n cos\left(n\left(\phi - \Phi^{RP}\right)\right)\right) \tag{6.1}$$

where ϕ and Φ^{RP} are the azimuthal angles of a particle and of the reaction plane respectively. The sine terms vanished due to symmetry with respect to the reaction plane. The anisotropic flow corresponding to v_1 is called *direct flow* since it corresponds to an overall shift of the distribution in the transverse plane. The flow corresponding to v_2 is called *elliptic flow* because v_2 it is used to quantify the eccentricity of the ellipse-like azimuthal distribution. In this formalism, the v_n can be also represented by average over all particles in all events:

$$v_n = \langle cos\left(n\left(\phi - \Phi^{RP}\right)\right)\rangle \tag{6.2}$$

In the real data analysis the reaction plane is unknown and it is estimated by event plane Φ_2^{EP}. Event plane is calculated on event-by-event basis using tracks in the event and it is described in the next section. Due to finite multiplicity of the event, limited number of tracks can be used to calculate the event plane – there is a limited precision (resolution) of Φ_2^{EP} calculations. Therefore in general Φ_2^{EP}differs from true reaction plane Φ^{RP} and the observed coefficients $v_n^{observed}$ differs from true Fourier coefficient v_n. Consequently it has to be corrected for

statistical dispersion and the real value of v_n is given by [118]:

$$v_n = \frac{v_n^{observed}}{\langle cos\left(n\left(\Phi^{RP} - \Phi^{EP}\right)\right)\rangle} \tag{6.3}$$

where $v_n^{observed}$ is $\langle cos\left(n\left(\Phi^{RP} - \Phi^{EP}\right)\right)\rangle$ represents the event plane resolution and correction for this statistical dispersion always increases the measured flow.

6.2 Event plane determination

The event plane was determined for each event using TPC. TPC has a full azimuthal coverage therefore provides good event plane resolution. Φ_2^{EP} was calculated with primary tracks passing basic quality cuts ($nHits > 15,\ nHits/nHitMax > 0.52$) and with $\eta < 1$, $DCA < 2$ cm, $0.1 < p_T < 2$ GeV/c. We used second order event plane Φ_2^{EP} which was calculated using following:

$$Q_2 cos\left(2\Phi_2^{EP}\right) = \sum_i w_i cos\left(2\phi_i\right) \tag{6.4}$$

$$Q_2 sin\left(2\Phi_2^{EP}\right) = \sum_i w_i sin\left(2\phi_i\right) \tag{6.5}$$

then Φ_2^{EP} can be calculated using:

$$\Phi_2^{EP} = \left(tan^{-1} \frac{\sum_i w_i cos\left(2\phi_i\right)}{\sum_i w_i sin\left(2\phi_i\right)} \right) /2 \tag{6.6}$$

where Q_2 is a flow vector for second harmonics, w_i are weights optimized to maximize the reaction plane resolution (make it as good as possible) and i goes over the particles used in event plane determination (*flow tracks*). Weights were associated with transverse momentum and ϕ where w_i is product of p_T weight $w_i^{p_T}$ and ϕ weight w_i^{ϕ}. ϕ weights were obtained by accumulation an azimuthal distribution of particles over large sample of events and then using inverse of this distribution as a weight while $w_i^{p_T}$ was a transverse momentum of given flow track. Additionally, to avoid autocorrelation of measured J/ψ with reaction plane, which would lead to strong positive v_2 signal, all tracks used in J/ψ reconstruction were removed from event plane calculation. The weighting method effectively removed TPC bias and obtained event plane distribution isotropic i.e. is flat with respect to ϕ (Fig. 6.1).

Weights w_i and event plane resolution were provided by STAR Bulk correlations physics working group [119, 120].

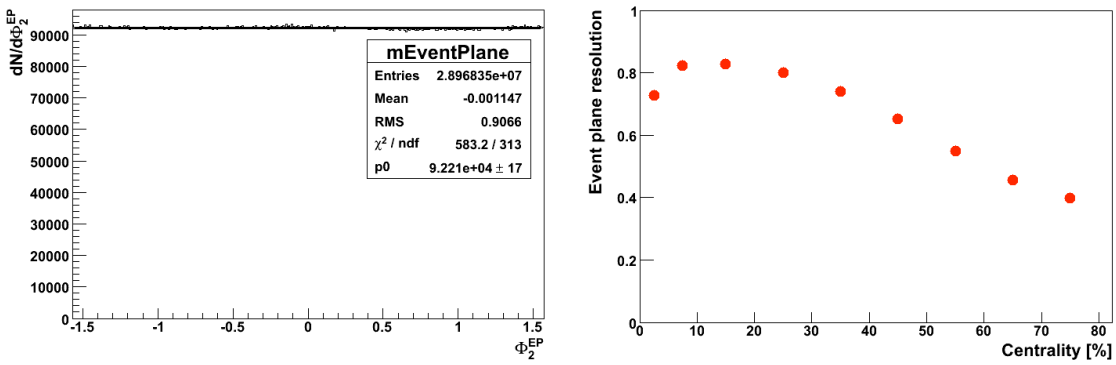

Figure 6.1: Left panel: Event plane distribution in minimum-bias Au+Au collisions with straight line fit. Right: Event plane resolution for selected centrality classes.

6.2.1 Resolution corrections

The measured elliptic flow $v_2^{obserwed}$ has to be corrected a statistical dispersion and it is done by dividing $v_2^{obserwed}$ by event plane resolution $\langle cos\left(2(\Phi_2^{EP} - \Phi^{RP})\right)\rangle$ to obtain real v_2.

It has been shown [118] that $\left\langle cos\left(2(\Phi_2^{EP} - \Phi^{RP})\right)\right\rangle$ can be expresses in terms of v_2 and previously defined weights w_i:

$$\langle \cos(2(\Phi_2^{EP} - \Phi^{RP}))\rangle = \frac{\sqrt{\pi}}{2\sqrt{2}}\chi_2 \exp(-\chi_2^2/4)\left[I_0(\chi_2^2/4) + I_1(\chi_2^2/4)\right] \tag{6.7}$$

where: $\sigma^2 = \frac{1}{2N}\frac{\langle w^2\rangle}{\langle w\rangle^2}$ and $\chi_2 \equiv v_2/\sigma$, N - number of particles used to determine event plane and I_0, I_1 are modified Bessel function of order 0 and 1.

A real value of v_2 is unknown and can not be used directly to obtain χ_2 and use in Eq. 6.7. Instead, one can estimate the resolution using event planes for two independent set of particles. Flow tracks in a given event were randomly divided into two subsets (sub-events), with approximately equal number of tracks, for which the event planes Φ_2^A and Φ_2^A were calculated separately. Then the event plane resolution for a sub-event is given by:

$$\langle cos(2(\Phi_2^A - \Phi^{RP}))\rangle = \sqrt{\langle cos(2(\Phi_2^A - \Phi_2^B))\rangle} \tag{6.8}$$

Next one can solve the Eq. 6.7 for sub-events resolution and extract χ_2^A for the sub-event. Then, as the multiplicity of full event is twice higher than sub-events, χ_2 for full event is given by $\chi_2 = \sqrt{2}\chi_2^A$. Then the resolution for full events is obtained using Eq. 6.7 for a given χ_2.

In studies presented here we made an attempt to calculate v_2 for 0-40% most central Au+Au events because most of the J/ψ are produced in central collisions and the limited statistic does

not allow for analyses in smaller centrality bins. The resolution depends on event multiplicity and magnitude of flow and it changes with event centrality (Fig. 6.1). To estimate systematic error we calculated the event plane resolution for this wide bin (0-40%) in three different ways:

1. using all flow tracks in 0-40% events: $\langle\cos(2(\Phi_2^{EP} - \Phi^{RP}))\rangle = 0.731$
2. $\langle\cos(2(\Phi_2^{EP} - \Phi^{RP}))\rangle$ was calculated for smaller centrality bins (0-5%, 5-10%, 10-20%, 20-30%, 30-40%) and then the final value was obtained by weighted average where weight was number of event in each centrality class: $\langle\cos(2(\Phi_2^{EP} - \Phi^{RP}))\rangle = 0.753$
3. $\langle\cos(2(\Phi_2^{EP} - \Phi^{RP}))\rangle$ was calculated for smaller centrality bins (0-5%,, 5-10%, 10-20%, 20-30%, 30-40%) and then the final value was obtained by weighted average where weight was number of flow tracks in each centrality class, $\langle\cos(2(\Phi_2^{EP} - \Phi^{RP}))\rangle = 0.767$

A systematic error due to choice of one of the methods is small compared to statistical error. It was included in systematic error on the final results.

6.3 Methods of elliptic flow extraction

An elliptic flow of short lived particles, like J/ψ, has to be study through their decay products. Firstly, one has to identify candidates which is done on statistical basis using invariant mass method. As the results one obtains correlated pairs (signal) and uncorrelated (combinatorial) background. To get the final results, one has to separate the flow of the signal from flow of a uncorrelated part. In the next paragraphs we briefly discuss methods that we employed in order to calculate elliptic flow of J/ψ.

6.3.1 Event and track selection

In the flow studies, we used Au+Au events with $|V_z| < 30$ cm and centrality of 0-40%. In the J/ψ reconstruction we used the same track quality cuts as in spectra studies although with different electron selection conditions: we required single electron to have $p_t > 1.3$ GeV/c, $|n\sigma_p| > 2.5$ and we did not use p/E cut. We changed the PID cuts because the significance of the observed signal with cuts listed above was similar to those with BEMC while the data used in flow studies (with estimated event plane) did not include BEMC information. Therefore we decided to make a first attempt to J/ψ v_2 studies with available data instead of re-running

analysis for the whole data set (which would take months considering amount of the data to process and limitations of computing power).

6.3.2 Event plane method

The event plane method is the simplest and most straightforward way to calculate an elliptic flow. In this approach the distribution of $dN/d(\phi - \Phi_2^{EP})$ (where ϕ is azimuthal angle of J/ψ) in p_T bins is calculated. To obtain such distribution, we select e^+e^- within $2.9 < M_{inv} < 3.2$ GeV/c^2 and then we extracted $dN/d(\phi - \Phi_2^{EP})$ for signal by subtraction of like-sign background in $dN/d(\phi - \Phi_2^{EP})$ bins. Then the observed v_2 signal can be obtained by fitting $dN/d(\phi - \Phi_2^{EP})$ by Fourier expansion of azimuthal distribution with respect to event plane:

$$dN/d(\phi - \Phi_2^{EP}) = A \times \left(1 + 2v_2^{obserwed} cos\left(2\left(\phi - \Phi_2^{EP}\right)\right)\right) \tag{6.9}$$

where A and $v_2^{obserwed}$ are free parameters. $v_2^{obserwed}$ has to be corrected for event plane resolution as is described in previous section. In equation 6.9 the full series was truncated and only v_2 was kept as higher Fourier coefficients are expected to decrease quickly with increasing order.

The event plane method for flow extraction relays on precise measurement the of signal. In case of limited statistics, which was available for studies presented here, and low signal-to-background ratio, the significance did not allow to extract meaningful results (statistical errors are substantial). We present obtained results as a proof of principle that such analysis is possible. There are sizable statistical fluctuations in the data which leads to substantial systematic error in the fitting procedure - for example change in binning size cause dramatic change in mean value of $v_2^{obserwed}$ (Fig. 6.2) although the results are consistent within statistical error. Additionally, there is a systematic error due to signal extraction which is not studied here as results are dominated by statistical uncertainties.

Due to limitations of the event plane method, we also tried another approach to extract J/ψ elliptic flow: v_2 versus invariant mass method, which is described in next section. The advantage of this method comes from the fact that an information about the shape of signal and background can be used to extract the flow and therefore the results should be less sensitive to statistical fluctuations.

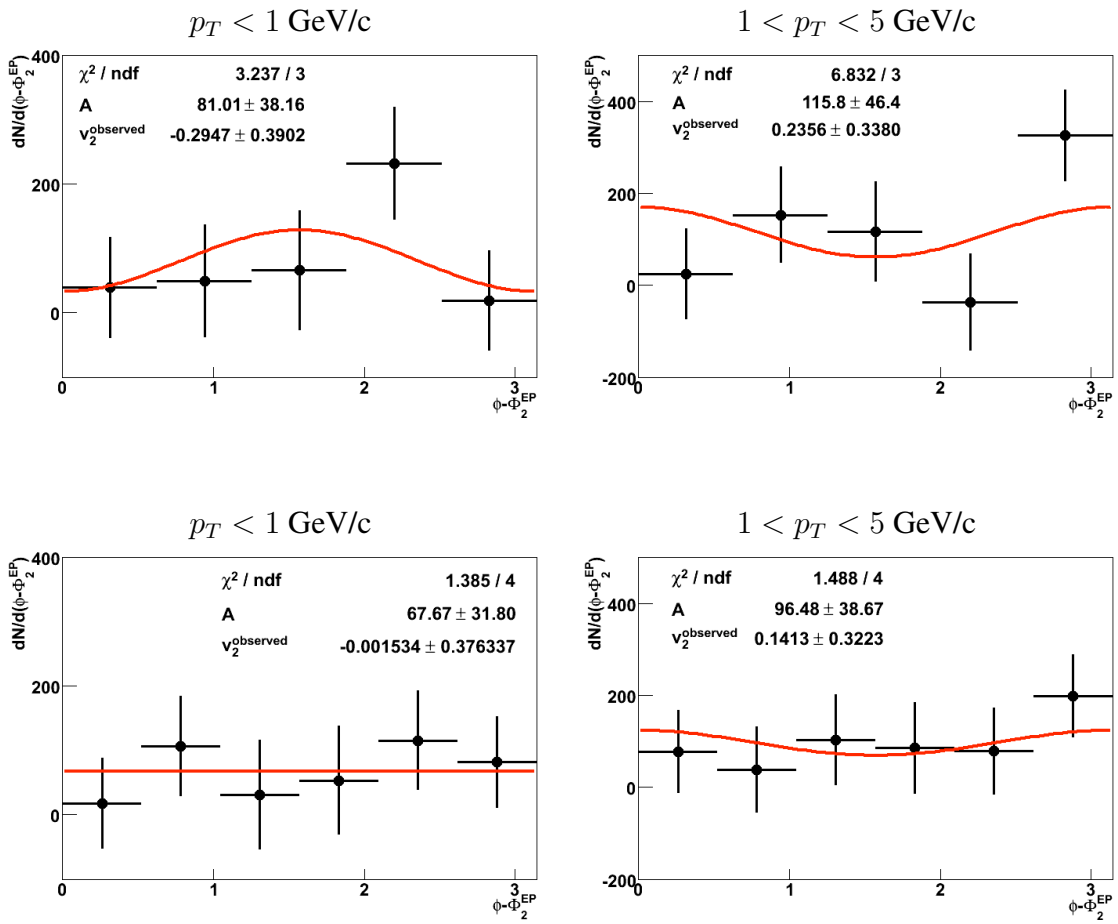

Figure 6.2: $dN/d(\phi - \Phi_2^{EP})$ for two p_T bins ($p_T < 1$ GeV/c, $1 < p_T < 5$ GeV/c) when J/ψ signal was extracted in 5 (upper row) or 6 bins of $\phi - \Phi_2^{EP}$.

6.3.3 v_2 versus invariant mass method

This method was proposed in [121]. The first assumption is that uncorrelated background $N_B(M_{inv})$ and signal $N_S(M_{inv})$ are smooth functions of invariant mass M_{inv}. Then the invariant mass distribution can be expresses by:

$$N_{S+B}(M_{inv}) = N_B(M_{inv}) + N_S(M_{inv}) \tag{6.10}$$

Then similar decomposition can be done for elliptic flow of all e^+e^- pairs:

$$N_{S+B}(M_{inv})v_2^{S+B}(M_{inv}) = N_B(M_{inv})v_2^B(M_{inv}) + N_S(M_{inv})v_2^S \tag{6.11}$$

which leads to:

$$v_2^{S+B}(M_{inv}) = \frac{N_B}{N_B + N_S}(M_{inv})v_2^B(M_{inv}) + \frac{N_S}{N_B + N_S}(M_{inv})v_2^S \tag{6.12}$$

where $N_{S+B}(M_{inv})$ - number of all e^+e^- pairs (signal and background) in a given invariant mass bin, $v_2^{S+B}(M_{inv})$ - flow of signal and background, $N_B(M_{inv})$ - number of background counts, $v_2^B(M_{inv})$ elliptic flow of background, $N_S(M_{inv})$ - signal yield and v_2^S is elliptic flow of signal.

$N_B(M_{inv})$, $N_S(M_{inv})$ and then $\frac{N_B}{N_B+N_S}(M_{inv})$ $\frac{N_S}{N_B+N_S}(M_{inv})$ can be extracted by fit to invariant mass distributions or using event-mixing method. Additional assumption has to be made about $v_2^{S+B}(M_{inv})$ - we used a second order polynomial. The method relays on good knowledge about $N_B(M_{inv})$ and $N_S(M_{inv})$, while in case of low statistic the fit to M_{inv} distribution results in uncertainty on fitted polynomial parameters which have to be taken into account. We used a Monte Carlo method together with fit covariance matrix to propagate errors from the fit to dN/dM_{inv} to the fit to $v_2^{S+B}(M_{inv})$ and the details of the procedure are described in the next section.

With known $\frac{N_B}{N_B+N_S}(M_{inv})$ $\frac{N_S}{N_B+N_S}(M_{inv})$ and functional form of $v_2^{S+B}(M_{inv})$, the v_2^S can be extracted by fitting the formula 6.12 to $v_2^{S+B}(M_{inv})$, where $v_2^{S+B}(M_{inv})$ is $\langle cos(2(\phi - \Phi_2^{EP})\rangle$ for all e^+e^- pairs.

The same decomposition like Eq. 6.12 can be done for $v_{2,sin} \equiv \langle sin(2(\phi - \Phi_2^{EP})\rangle$. Due to symmetry of J/ψ with respect to reaction plane, the coefficient $v_{2,sin}^S$ is equal zero when no experimental biases or fluctuations are present [121]. We used this property to cross check our calculation for bias due to event plane calculations and the obtained results are consistent with zero (Fig. 6.5).

We assumed that the background can be described by polynomial $f^B(M_{inv})$ while the signal could be represented by Gaussian function $f^S(M_{inv})$. $N_B(M_{inv})$ was obtained by fitting polynomial $f^B(M_{inv})$ to like-sign background in invariant mass range $2.2 < M_{inv} < 4.0$ GeV/c^2. Then the invariant mass distribution of all e^+e^- pairs (signal and background) was fitted by $f^{S+B}(M_{inv}) = f^S(M_{inv}) + f^B(M_{inv})$. The parameters of $f^B(M_{inv})$ were fixed in the previous fit to the like-sigh background. It was necessary because, due to low signal-to-background ratio, the simultaneous fit of $f^B(M_{inv})$ and $f^S(M_{inv})$ did not converge. The example of the signal and background distributions for lower p_T bin are shown in Fig. 6.3 while the ratio of signal and background as a function of M_{inv} is presented in Fig.6.4.

Due to limited statistics and low signal-to-background ratio, the significance of the extracted

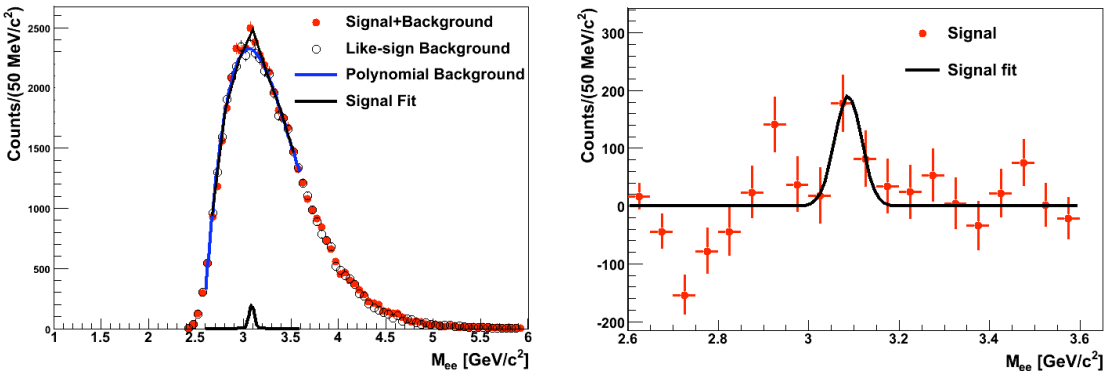

Figure 6.3: Left: Invariant mass distribution with signal and background fits used $v_2(M_{inv})$ calculation. Right: M_{inv} with polynomial background subtracted.

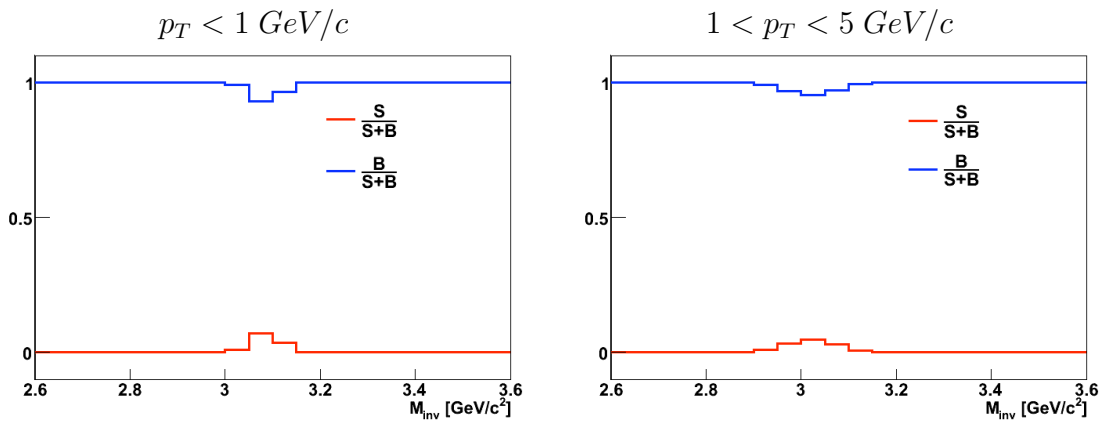

Figure 6.4: Normalized Signal-to-Background rations.

signal, calculated as $S/\sqrt{S+B}$ in $2.9 < M_{inv} < 3.15$ GeV/c^2, is rather low: on the level of 3. This leads to sizable uncertainty in the fit results for v_2^S although the precision is better than in the case of the event plane method.

6.4 Results and discussion

The limited statistics and the method chosen to estimate background (polynomial fit) introduce two problems:

- systematic error due to choice of function used to estimate background
- propagation of the errors from fits of signal and background to v_2 fits

The former was studied by changing fit function used in the procedure. In the latter case, we used Monte Carlo technique [1] to propagate errors from $S(M_{inv})$ and $B(M_{inv})$ fits to

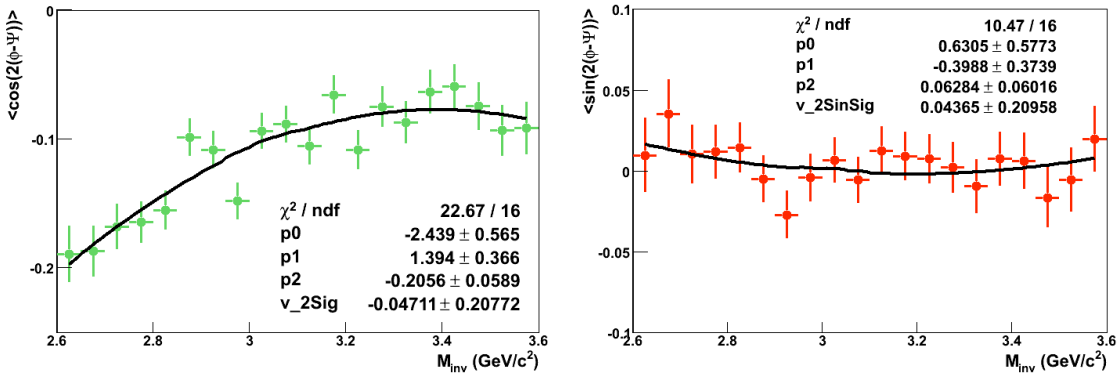

Figure 6.5: $v_2^{S+B}(M_{inv}) = \langle cos(2(\phi - \Phi_2^{EP})\rangle$ (left) and $\langle sin(2(\phi - \Phi_2^{EP})\rangle$ with fits for $0 < p_T^{J/\psi} < 1$ GeV/c. Due to limited statistics there is sizable error in the fit. Both v_2^S and $v_{2,sin}^S$ are consistent with zero although within substantial statistical uncertainty.

v_2 calculations. For each function $f(M_{inv})$ with n free parameters p_i, we have a vector of parameters μ_i corresponding to best fit and vector of associated errors $\delta\mu_i$. Then we extracted $n \times n$ covariance matrix V which provides information about relations between p_i. Next we applied Cholesky decomposition to find a matrix L – unique lower triangular matrix that fulfills $V = LL^T$. Next we generated a vector $Z = (z_1, z_2, \ldots z_n)$ whose components are n independent uniform variates. Then the new set of parameters p_i can be obtain by:

$$p_i = \mu_i + \sum_{j=1} NL_{ij} z_j \delta\mu_i \tag{6.13}$$

We can use $f(M_{inv})$ with those new parameters in v_2 studies. Repeating this procedure many times we generate a distribution of p_i with variance $\delta\mu_i$ and mean values μ_i preserving correlation between parameters p_i. To propagate the errors of $f(M_{inv})$ to v_2 results, we create distribution of dN/dv_2 and $dN/d(\Delta v_2)$ which example is shown on Fig. 6.6. The mean value of dN/dv_2 and $dN/d(\Delta v_2)$ were chose as a best representation of v_2 and Δv_2 respectively while the RMS of dN/dv_2 was included in systemic error.

The obtained results are presented in Fig. 6.7 and compared to those reported by PHENIX collaboration [72]. The available statistic does not allow to distinguish between different scenarios of J/ψ production, which were discussed in section 1.4.4. At the moment this measurements is rather proof of principle of such calculations at STAR although it will become an important tool for investigation of QGP thermalization and J/ψ production mechanism when the high statistic data are available.

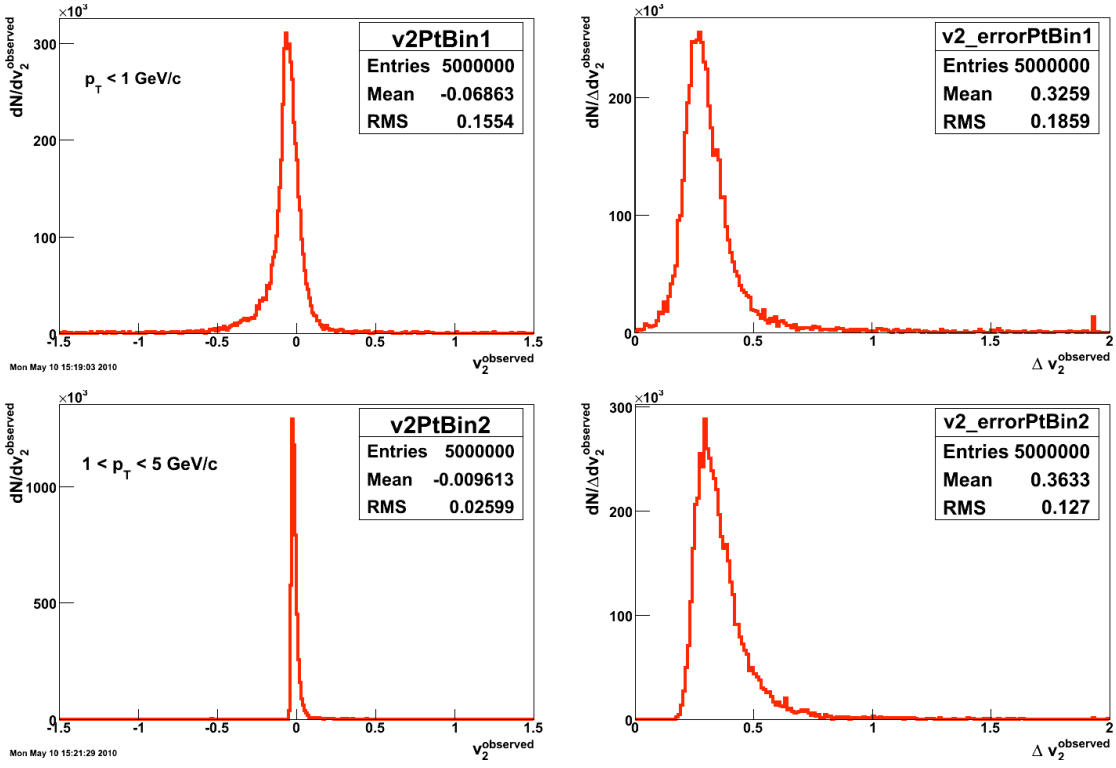

Figure 6.6: Distribution of fit results $v_n^{observed}$ (left) and its error (right) obtained by error propagation from fit to dN/dM_{inv} to fit to $v_2(M_{inv})$.

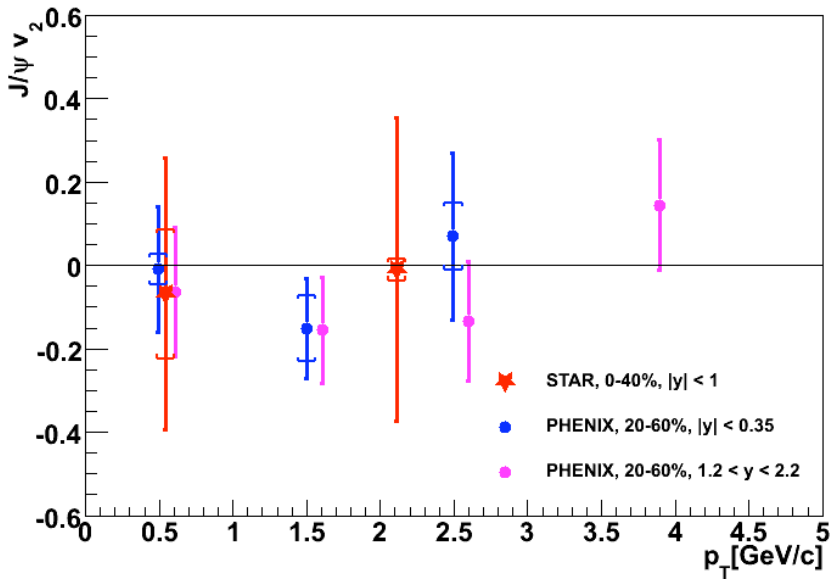

Figure 6.7: J/ψ elliptic flow (obtained using v_2 versus invariant mass method) compared to preliminary PHENIX results [72]. The bars represent statistical and the brackets systematic errors.

Chapter 7

Prospects for J/ψ trigger in Au+Au collisions

J/ψ production is a rear process and therefore the large statistics is require to obtain accurate results. In the case of minimum-bias events, the precision of the measurement is limited by amount of collected data. Consequently, in order to obtained results with a satisfactory statistical precision, an effective trigger has to be deploy.

The heavy quarkonia trigger in STAR was already developed [122] and was successfully employed in $p + p$ 200 GeV collisions recorded in 2006 [89, 123]. The low-p_T J/ψ trigger definition consisted of information from BEMC, used to select electron candidates, and CTB which was used to suppress the background from photons (CTB was sensitive only to charged particles). On the other hand, the simulations showed that in the Au+Au collisions the trigger with such setup did not provide sufficient background rejection because the granularity of CTB was too coarse [122]. Since 2009 the new Time-of-Flight detector is installed in STAR [124, 125] and we investigated the feasibility of low-p_T J/ψ trigger in Au+Au collisions with the ToF used to reject the background from photons.

7.1 Low-p_T J/ψ topology trigger

In 2006, the low-$\boldsymbol{p_T}$ J/ψ trigger setup was divided into two levels. The first one, level-0 (L0), was a topology trigger defined by the hardware. In L0 setup, the BEMC towers were combined into 12 patches with size: $\phi \times \eta = 1 \times 1$. Each half of BEMC was divided in ϕ into 6 section.

The low-p_T J/ψ's likely decay into electron-positron pairs with large opening angle, there-

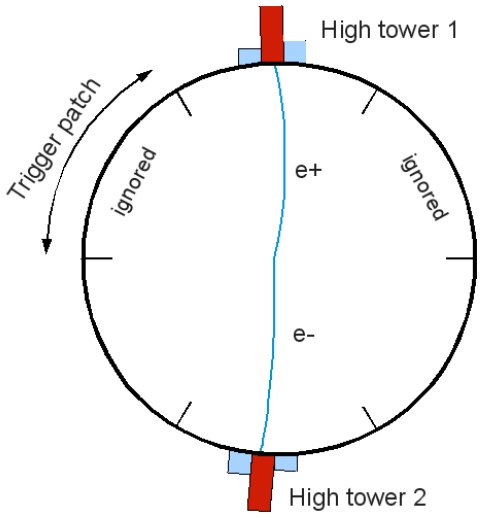

Figure 7.1: Schematic diagram of the L0 setup used in low-p_T J/ψ trigger.

fore L0 trigger required at least two towers above a given threshold ($E_T > 1.2$ GeV in that case) which are topologically separated by at least $60°$. This led to the requirement that the towers passing E_T cut could not be in the adjacent sections in ϕ, which is illustrated in Fig. 7.1. The parameters of the trigger, namely the energy threshold and the opening angle cut, were chosen based on simulations [122].

The next level of the trigger, L2, is a software algorithm that takes the input from the L0 to make the final decision. The CTB information was used to veto towers that received their energy from incident photons. This was done by requiring a signal in the CTB slat that corresponds geometrically to the chosen tower (the signal could be only from a charged particle as the CTB is not sensitive to photons). The non vetoed L0 towers were then used as seeds to create clusters of 3 towers: the seed tower plus the two adjacent towers with the highest energy values. The cluster position was computed as the weighed average of position of the three towers, using their energies as weights. The clustering allowed to collect most of the energy which had leaked to the neighboring towers, and therefore improved the mass resolution. After the complete iteration to find electron clusters, all possible clusters pairs are made and the invariant mass of the pair was calculated with approximation:

$$M = \sqrt{2E_iE_j\left(1 - \cos\theta_{ij}\right)} \tag{7.1}$$

where $E_{i(j)}$ is the energy of the cluster $i(j)$ and θ_{ij} is the opening angle between them. The formula 7.1 was derived assuming that electron mass is negligible [122], which is justified for this energy. The opening angle of the pair was calculated assuming interaction vertex at (0,0,0)

and straight tracks approximation. If 2.2$<M<$5.0 GeV/c^2 for at least one of the possible pairs of clusters, then the event was recorded. The L0 decision time was $\leq$1 μs and the decision at the L2 was taken up to 500 μs.

7.2 J/ψ topology trigger with ToF in Au+Au 200 GeV

The ToF detector is sensitive only to charged tracks only and it has much finer granularity compared to CTB (ToF - 23040 cells, CTB - 240 slats). The recent test of performance of Υ L2 trigger with ToF for p+p 200 GeV data taken in 2009 showed the increase of background rejection by factor 6 [126]. A set of tests was performed to examine if background rejection of J/ψ topology trigger with ToF is adequate to make an effective trigger in Au+Au collisions. The study was done using 23 thousand Au+Au minimum-bias background events (without additional J/ψ signal included) at $\sqrt{s_{NN}} = 200$ GeV obtained using HIJING [127]+GEANT [102] simulation of the STAR detector setup for year 2010. The matching of ToF cells to BEMC towers was studied in [126] using Monte Carlo simulations to account for detector effects and the results (ToF-to-BEMC lookup tables) were used in our trigger evaluation study. We also compared the performance of the topology trigger to a single tower (so-called "High Tower") trigger.

In this study, the High Tower and the low-p_T topology trigger were defined as follows:

- Low-p_T topology trigger
  - L0 trigger:
    1. There are at least two towers with the energy above $E_0 > 1.2$ GeV
    2. The opening angle θ between candidate towers is at lease 60° ($cost(\theta) < 0.5$), where θ is calculated assuming interaction vertex at (0,0,0) and straight tracks approximation.
  - L2 trigger:
    1. A cluster of 3 towers used: L0 seed + 2 neighboring towers with highest energy
    2. The cluster energy is greater then given energy threshold E_2
    3. ToF filter - a cluster accepted if there is at least one ToF hit matched to any tower in the cluster

4. The opening angle θ between clusters in candidate pair is at lease 60° ($cost(\theta) < 0.5$), where θ is calculated assuming interaction vertex at (0,0,0) and straight tracks approximation.
5. 2.2< M <5.0 GeV/c^2, where $M = \sqrt{2E_1E_2\,(1-\cos\theta)}$

- High Tower trigger - single tower energy above a given energy threshold E_0

The trigger capacity is determined by two factors: background rejection and signal efficiency. The background rejection is important because of limited time devoted to a given trigger by the overall trigger system (the bandwidth in the trigger hardware is limited and it is shared by other competitive triggers). In addition, the available storage space is also limited and if a given trigger accepts too many background events, then the trigger rate has to be limited (pre-scalled) to match those limitation. If the trigger is pre-scalled, then the luminosity which can be sampled is also limited. On the other hand, the trigger should have a high efficiency i.e. it should accept as many J/ψ as possible because if the efficiency is low, then the overall signal yield in triggered sample could be smaller then in minimum-bias sample, and then there is no benefit of using the trigger at all. Therefore, the trigger parameters have to meet opposite requirements: they should be strict enough to increase background rejection and relaxed enough to provide sufficient signal efficiency. In practice, the choice of these parameters is a trade-off between those two goals.

To quantify the background rejection, we used a rejection factor (also called a rejection power) *RP*:

$$RP = \frac{N_{input}}{N_{accepted}} \tag{7.2}$$

where N_{input} is number of input background events for a given trigger and $N_{accepted}$ is a number of accpted background events. For example, if the $RP = 10$ than the background was reduced by factor 10.

For J/ψ topology trigger, we studied the rejection power for L0 and L2 levels and we defined the rejection factors for each one as follows:

- L0 background rejection:
  $RP_{L0} = (\text{All background events})/(\text{Background events accepted by L0})$

- L0+L2 background rejection:
  $RP_{L0+L2} = (\text{All background events})/(\text{Background events accepted by L2})$

To estimate the efficiency of triggers and the impact of the trigger conditions on measured J/ψ p_T spectrum, we used Pythia simulation of J/ψ production in p+p at $\sqrt{s} = 200$ GeV, and we applied following cuts:

- HT0: $p_T^{e_1} > 2.6$ GeV/c or $p_T^{e_2} > 2.6$ GeV/c
- L0 + L2 topology trigger: $p_T^{e_1} > E_0$ and $p_T^{e_2} > E_0$ and $cos(\theta) < 0.5$; θ - opening angle of e^+e^- pair

Table 7.1: Rejection power for High Tower trigger (HT) and J/ψ topology trigger with different energy thresholds.

Trigger	Background rejection power
L0+L2, E_0 = 1.2 GeV, E_2 = 1.5 GeV	4.5
L0+L2, E_0 = 1.5 GeV, E_2 = 1.5 GeV	4.6
L0+L2, E_0 = 1.75 GeV, E_2 = 1.75 GeV	7.4
L0+L2, E_0 = 2 GeV, E_2 = 2 GeV	14
L0+L2, E_0 = 2.3 GeV, E_2 = 2.3 GeV	43
L0+L2, E_0 = 2.6 GeV, E_2 = 2.6 GeV	164
L0+L2, E_0 = 3.0 GeV, E_2 = 3.0 GeV	1561
HT0 (E_0 = 2.6 GeV)	7.7
HT1 (E_0 = 3.5 GeV)	53
HT2 (E_0 = 4.3 GeV)	294

The results of background rejection studies are presented in Tab. 7.1 and Fig. 7.2 while Fig. 7.3 shows a comparison of J/ψ efficiency for different energy thresholds in topology and high-tower trigger. We found that the ToF filter increases the rejection power by factor 2 for L0+L2 compared to L0 trigger level (Fig. 7.2). The overall L0+L2 rejection power for $E_0 = 1.2$ and $E_2 = 1.5$ GeV is on the level of 4.5 for min-bias collisions. With these parameters, it would have to be pre-scaled to meet disc space availability. The trigger efficiency is $\sim 10\%$ therefore there is no gain when the J/ψ topology trigger is used. The increase of energy threshold increases the rejection power significantly, although it also significantly reduces the trigger efficiency.

Such a low rejection power is caused by high charged track multiplicity in Au+Au collisions and course granularity of BEMC towers. Even though the ToF granularity is much finer than

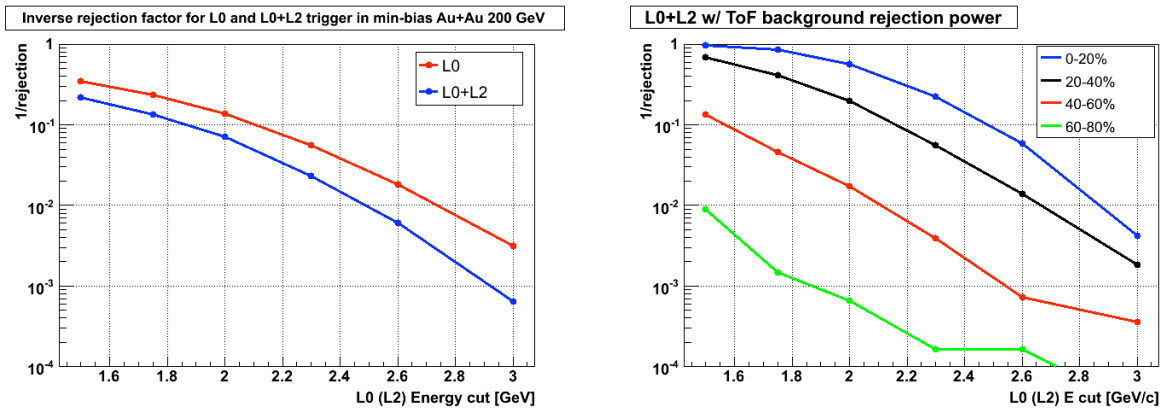

Figure 7.2: The inverse background rejection power of J/ψ topology trigger as a function of energy threshold for min-bias collisions (left) and in centrality classes (right). L2+ToF improves rejection power by factor 2 compared to L0 although the rejection power is only sufficient for peripheral events.

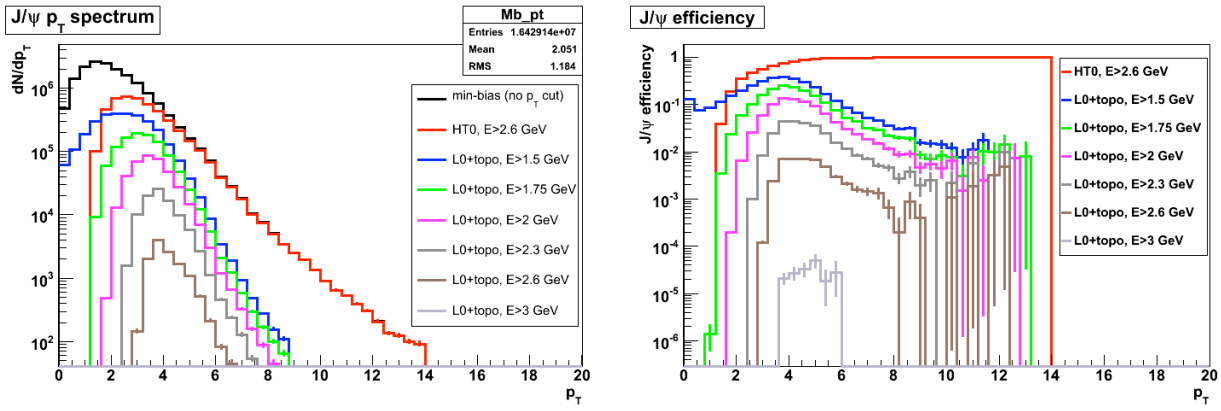

Figure 7.3: Impact of J/ψ topology trigger on p_T spectrum: p_T spectrum (left) and trigger efficiency (right) for different L2 energy thresholds.

CTB, there is on average 9-10 ToF cells matched to a single tower for events with $|V_z| < 30$ cm[1]. Therefore the rejection of photon signal is limited because there is a hight probability to have a charged track signal in one of the ToF cells matched to a given cluster.

In addition, L0 and L2 thresholds of $E_0 = 1.75$ and $E_2 = 1.75$ GeV are required to obtain similar background rejection as HT0 trigger while the HT0 efficiency is much higher and it does not deteriorate with p_T (see right panel of Fig. 7.3). Therefore it is more effective to use the high tower trigger than the topological one with high energy thresholds.

In summary, we found that a sufficiently effective low-p_T J/ψ trigger can not be implemented with the currently available detector setup, and therefore the analyses can be only carried out with minimum-bias data. On the other hand, STAR has presently accumulated a large sample (300 million) of Au+Au minimum-bias events at $\sqrt{s_{NN}} = 200$ GeV. Since the SSD and SVT detectors were removed from the STAR detector, it is expected that the combinatorial background due to γ conversion on SSD and SVT material will be significantly reduced. Therefore the statistic collected in 2010, together with the improved particle identification with the ToF detector, should allow to measure J/ψ p_T spectrum and J/ψ elliptic flow with a statistical precision of 5% [117].

[1]The number of ToF cells matched to single BEMC tower depends on event vertex z position: for $|V_z| < 10$ cm there is on average 9 ToF cells per single tower while for $|V_z| < 60$ cm the number is higher: 11-12 cells

Chapter 8

Summary

Relativistic heavy ion physics addresses possibly the most compelling and challenging area of our field. If successful, it will allow to understand the dynamics of the Quark-Gluon Plasma phase. Charmonium production and suppression is considered to be an important tool in studying the properties of the hot and dense nuclear matter, possibly QGP, created in relativistic heavy ion collisions. The low-p_T J/ψ production is of a particular interest as it allows us to study the thermodynamical properties of the medium. We have reported the first measurements of the J/ψ nuclear modification factor in Au+Au collisions at STAR as well as the first study of low-p_T J/ψ in Cu+Cu collisions at STAR. The J/ψ meson invariant yields, both integrated and p_T spectra, have been measured in Au+Au and Cu+Cu collisions at $\sqrt{s_{NN}} = 200$ GeV. The nuclear modification factor R_{AA} as a function of transverse momentum and event centrality was extracted. The R_{AA} shows that the J/ψ production, both in central (0–20%) and semi-peripheral (20–80%) Au+Au collision, scaled by the corresponding number of binary collisions, is strongly suppressed compared to $p + p$. This suggest that a very high energy density is created in these collisions. Moreover, models which assume that the energy density is above the threshold for the QGP formation, describe the data well. On the other hand, in some models the suppression can be explained by shadowing and nuclear absorption alone.

The good agreement with the results published by the PHENIX experiment is seen in spite of limited statistics from STAR. It is an extremely important experimental cross check as these two analysis were carried out using completely different detectors, different analysis techniques, and operated in a different rapidity range.

We also studied the J/ψ elliptic flow in Au+Au collisions. Due to limited statistics, the results are inconclusive, although it is a proof-of-principle of such a analysis in STAR. It is

a very important measurement because it can demonstrate a degree of thermalization of the hypothetically formed partonic matter.

Finally, we examined the experimental prospects for low-p_T J/ψ measurements via di-electron channel in Au+Au collisions at STAR. The sufficiently effective low-p_T J/ψ trigger could not be implemented with the currently available detector setup, and therefore the analyses can be only carried out with minimum-bias data. With the number of minimum-bias Au+Au events collected in 2010, the J/ψ production and elliptic flow are expected to be measured with a statistical precision better than 5%. It will allow to test the hypothesis of J/ψ production in QGP via a statistical coalescence of c and $\overline{c}$ quarks.

This work outlines the fundamental strategy for the future analysis of J/ψ production with the STAR detector. The software and methods developed during the studies reported here, particularity the algorithms for finding the optimal electron selection criteria, efficiency assessment and systematic uncertainties studies, will provide important tools and a knowledge for charmonium studies in the future.

Appendix A

Systematic uncertainties

A.1 Main sources of systematic uncertainties in the case of Cu+Cu collisions

Table A.1: Summary of systematic error on J/ψ yield in Cu+Cu collisions

Centrality	J/ψ p_T **range [GeV/c]**	**Error -**	**Error +**
0-60%	integrated	14%	19%
0-60%	0-1	26%	33%
0-60%	1-5	17%	14%
0-20%	integrated	21%	26%
20-60%	integrated	14%	5%

Table A.2: Systematic error due to estimation of single electron identification efficiency

Centrality	J/ψ p_T **range [GeV/c]**	**Error -**	**Error +**
0-60%	integrated	2%	2%
0-60%	0-1	3%	3%
0-60%	1-5	2%	2%
0-20%	integrated	2%	2%
20-60%	integrated	2%	2%

Table A.3: Systematic error due to different methods of yield extraction: bin counting vs. simulated line shape.

Centrality	J/ψ p_T **range [GeV/c]**	**Error -**	**Error +**
0-60%	integrated	0.0%	18%
0-60%	0-1	0.0%	28%
0-60%	1-5	0.0%	14%
0-20%	integrated	0.0%	26%
20-60%	integrated	0.0%	2%

Table A.4: Systematic error due to yield extraction using different invariant mass range in which the yield was calculated

Centrality	J/ψ p_T **range [GeV/c]**	**Error -**	**Error +**
0-60%	integrated	0.0%	0.3%
0-60%	0-1	0.6%	0.0%
0-60%	1-5	0.0%	0.2%
0-20%	integrated	0.0%	0.0%
20-60%	integrated	0.0%	0.0%

Table A.5: Systematic error due to shape of J/ψ p_T and rapidity spectrum used in efficiency calculation in Cu+Cu

Centrality	J/ψ p_T **range [GeV/c]**	**Error -**	**Error +**
0-60%	integrated	2%	0.0%
0-60%	0-1	2%	0.0%
0-60%	1-5	3%	0.0%
0-20%	integrated	3%	0.0%
20-60%	integrated	2%	0.0%

Table A.6: Systematic error due to reconstruction efficiency using embedding

Centrality	J/ψ p_T **range [GeV/c]**	**Error -**	**Error +**
0-60%	integrated	2%	3%
0-60%	0-1	2%	2%
0-60%	1-5	3%	2%
0-20%	integrated	2%	4%
20-60%	integrated	2%	3%

Table A.7: Systematic error due to yield extraction using different normalization of a background

Centrality	J/ψ p_T **range [GeV/c]**	**Error -**	**Error +**
0-60%	integrated	14%	1%
0-60%	0-1	26%	18%
0-60%	1-5	16%	0%
0-20%	integrated	20%	0%
20-60%	integrated	14%	1%

A.2 Main sources of systematic uncertainties in the case of Au+Au collisions

Table A.8: Summary of systematic error on J/ψ yield in Au+Au collisions

Centrality	J/ψ p_T **range [GeV/c]**	**Error -**	**Error +**
0-80%	0-1	51%	5%
0-80%	1-2	20%	91%
0-80%	2-5	4%	32%
0-20%	integrated	10%	7%
20-80%	integrated	28%	21%

Table A.9: Systematic error due to possible residual background.

Centrality	J/ψ p_T **range [GeV/c]**	**Error -**	**Error +**
0-80%	0-1	19%	0%
0-80%	1-2	0%	19%
0-80%	2-5	0%	17%
0-20%	integrated	8%	0%
20-80%	integrated	26%	0%

Table A.10: Systematic error due to shape of J/ψ p_T and rapidity spectrum used in efficiency calculation.

Centrality	J/ψ p_T**range [GeV/c]**	**Error -**	**Error +**
0-80%	0-1	4%	0%
0-80%	1-2	3%	0%
0-80%	2-5	3%	0%
0-20%	integrated	4%	0%
20-80%	integrated	3%	0%

Table A.11: Systematic error due to reconstruction efficiency using embedding.

Centrality	J/ψ p_T **range [GeV/c]**	**Error -**	**Error +**
0-80%	0-1	4%	4%
0-80%	1-2	3%	3%
0-80%	2-5	2%	4%
0-20%	integrated	4%	5%
20-80%	integrated	2%	2%

Table A.12: Systematic error due to estimation of single electron identification efficiency.

Centrality	J/ψ p_T **range [GeV/c]**	**Error -**	**Error +**
0-80%	0-1	0.3%	0%
0-80%	1-2	0%	0.8%
0-80%	2-5	0%	1.4%
0-20%	integrated	0%	0.7%
20-80%	integrated	0%	0.6%

Table A.13: Systematic error due to different normalization of a background.

Centrality	J/ψ p_T **range [GeV/c]**	**Error -**	**Error +**
0-80%	0-1	47%	0%
0-80%	1-2	2%	89%
0-80%	2-5	0%	6%
0-20%	integrated	0%	4%
20-80%	integrated	10%	10%

Table A.14: Systematic error due to method of raw yield extraction: bin counting vs. simulated line shape.

Centrality	J/ψ p_T **range [GeV/c]**	**Error -**	**Error +**
0-80%	0-1	0%	3%
0-80%	1-2	20%	0%
0-80%	2-5	0%	26%
0-20%	integrated	1%	0%
20-80%	integrated	0%	18%

Bibliography

[1] K Nakamura and Particle Data Group. Review of particle physics. *J. Phys. G: Nucl. Part. Phys.*, 37(075021), 2010.

[2] Donald H. Perkins. *Introduction to High Energy Physics*. Cambridge University Press, April 2000.

[3] Siegfried Bethke. The 2009 Wolrd Average of $\alpha_s(M_Z)$. *Eur. Phys. J.*, C64:689–703, 2009.

[4] George Sterman et al. Handbook of perturbative qcd. *Rev. Mod. Phys.*, 67(1):157–248, Jan 1995.

[5] Ellis R. K.; Stirling W. J.; Webber B. R. Cambridge University Press, 1996.

[6] A. Abulencia et al. Measurement of the inclusive jet cross section in $p\bar{p}$ interactions at $\sqrt{s} = 1.96$-TeV using a cone-based jet algorithm. *Phys. Rev.*, D74:071103, 2006.

[7] T. Aaltonen et al. Measurement of the Inclusive Jet Cross Section at the Fermilab Tevatron p-pbar Collider Using a Cone-Based Jet Algorithm. *Phys. Rev.*, D78:052006, 2008.

[8] Z. Fodor and S. D. Katz. The phase diagram of quantum chromodynamics. 2009.

[9] Z. Fodor and S. D. Katz. A new method to study lattice QCD at finite temperature and chemical potential. *Phys. Lett.*, B534:87–92, 2002.

[10] C. R. Allton et al. The QCD thermal phase transition in the presence of a small chemical potential. *Phys. Rev.*, D66:074507, 2002.

[11] Philippe de Forcrand and Owe Philipsen. The QCD phase diagram for small densities from imaginary chemical potential. *Nucl. Phys.*, B642:290–306, 2002.

[12] Berndt Muller. *The physics of the quark-gluon plasma*. Springer-Verlag, Berlin ; New York :, 1985.

[13] Yasuo Miake Kohsuke Yagi, Tetsuo Hatsuda. *Quark-Gluon Plasma: From Big Bang to Little Bang*. Cambridge University Press, 2006.

[14] John Ellis. From little bangs to the big bang. *Journal of Physics: Conference Series*, 50(1):8, 2006.

[15] Reinhard Stock. The QCD Phase Diagram: Expectations and Challenges. *PoS*, CPOD2009:001, 2009.

[16] A. Bazavov et al. Equation of state and QCD transition at finite temperature. *Phys. Rev.*, D80:014504, 2009.

[17] Z. Fodor, S. D. Katz, and K. K. Szabo. The QCD equation of state at nonzero densities: Lattice result. *Phys. Lett.*, B568:73–77, 2003.

[18] Z. Fodor and S. D. Katz. Critical point of QCD at finite T and mu, lattice results for physical quark masses. *JHEP*, 04:050, 2004.

[19] R. V. Gavai and Sourendu Gupta. The critical end point of QCD. *Phys. Rev.*, D71:114014, 2005.

[20] Aggarwal M. M. et al. An Experimental Exploration of the QCD Phase Diagram: The Search for the Critical Point and the Onset of De- confinement. 2010.

[21] RHIC web page: `http://www.bnl.gov/rhic`.

[22] M. Gazdzicki. Ion Program of Na61/Shine at the CERN SPS. *J. Phys.*, G36:064039, 2009.

[23] B. I. Abelev et al. J/psi production at high transverse momentum in p+p and Cu+Cu collisions at sqrt(sNN)=200GeV. *Phys. Rev.*, C80:041902, 2009.

[24] Stephen Scott Adler et al. High transverse momentum η meson production in p^+p, d^+ Au and Au+Au collisions at $S(NN)^{(1/2)}$ = 200-GeV. *Phys. Rev.*, C75:024909, 2007.

[25] David d'Enterria. Jet quenching in QCD matter: from RHIC to LHC. *Nucl. Phys.*, A827:356c–364c, 2009.

[26] Ivan Vitev. Testing the theory of QGP-induced energy loss at RHIC and the LHC. *Phys. Lett.*, B639:38–45, 2006.

[27] C. Adler et al. Disappearance of back-to-back high p_T hadron correlations in central Au+Au collisions at $\sqrt{s_{NN}}$ = 200-GeV. *Phys. Rev. Lett.*, 90:082302, 2003.

[28] John Adams et al. Experimental and theoretical challenges in the search for the quark gluon plasma: The STAR collaboration's critical assessment of the evidence from RHIC collisions. *Nucl. Phys.*, A757:102–183, 2005.

[29] S. Voloshin and Y. Zhang. Flow study in relativistic nuclear collisions by Fourier expansion of Azimuthal particle distributions. *Z. Phys.*, C70:665–672, 1996.

[30] STAR Collaboration. Azimuthal anisotropy in au+au collisions at sqrtsnn = 200 gev. *Physical Review C*, 72:014904, 2005.

[31] S. A. Voloshin. Anisotropic flow. *Nucl. Phys.*, A715:379–388, 2003.

[32] R. J. Fries, Berndt Muller, C. Nonaka, and S. A. Bass. Hadron production in heavy ion collisions: Fragmentation and recombination from a dense parton phase. *Phys. Rev.*, C68:044902, 2003.

[33] Denes Molnar and Sergei A. Voloshin. Elliptic flow at large transverse momenta from quark coalescence. *Phys. Rev. Lett.*, 91:092301, 2003.

[34] V. Greco, C. M. Ko, and P. Levai. Parton coalescence at RHIC. *Phys. Rev.*, C68:034904, 2003.

[35] Roy A. Lacey and Arkadij Taranenko. What do elliptic flow measurements tell us about the matter created in the little bang at RHIC? *PoS*, CFRNC2006:021, 2006.

[36] B. I. Abelev et al. Partonic flow and Phi-meson production in Au + Au collisions at s(NN)**(1/2) = 200-GeV. *Phys. Rev. Lett.*, 99:112301, 2007.

[37] A. Adare et al. Energy Loss and Flow of Heavy Quarks in Au+Au Collisions at $\sqrt{s_{NN}}$ = 200 GeV. *Phys. Rev. Lett.*, 98:172301, 2007.

[38] Matteo Cacciari, Paolo Nason, and Ramona Vogt. Qcd predictions for charm and bottom quark production at rhic. *Phys. Rev. Lett.*, 95(12):122001, Sep 2005.

[39] T. Matsui and H. Satz. J/[psi] suppression by quark-gluon plasma formation. *Physics Letters B*, 178(4):416 – 422, 1986.

[40] Louis Kluberg and Helmut Satz. Color Deconfinement and Charmonium Production. 2009.

[41] R. Rapp, D. Blaschke, and P. Crochet. Charmonium and bottomonium in heavy-ion collisions. *Progress in Particle and Nuclear Physics*, In Press, Accepted Manuscript:–, 2010.

[42] Ágnes Mócsy and Péter Petreczky. Color screening melts quarkonium. *Phys. Rev. Lett.*, 99(21):211602, Nov 2007.

[43] Helmut Satz. Colour deconfinement and quarkonium binding. *Journal of Physics G: Nuclear and Particle Physics*, 32(3):R25, 2006.

[44] A. Jakovác, P. Petreczky, K. Petrov, and A. Velytsky. Quarkonium correlators and spectral functions at zero and finite temperature. *Phys. Rev. D*, 75(1):014506, Jan 2007.

[45] P. Braun-Munzinger and J. Stachel. Charmonium from Statistical Hadronization of Heavy Quarks – a Probe for Deconfinement in the Quark-Gluon Plasma. 2009.

[46] Robert L. Thews, Martin Schroedter, and Johann Rafelski. Enhanced j/ψ production in deconfined quark matter. *Phys. Rev. C*, 63(5):054905, Apr 2001.

[47] Loïc Grandchamp, Ralf Rapp, and Gerald E. Brown. In-medium effects on charmonium production in heavy-ion collisions. *Phys. Rev. Lett.*, 92(21):212301, May 2004.

[48] Voica A. Radescu. Extraction of the Proton Parton Density Functions from the Combined HERA I Data using NLO QCD Fit. *Proc. of XVII Int. Workshop on Deep-Inelastic Scattering and Related Topics, Madrid, Spain, April 2009*.

[49] J. P. Lansberg. J/ψ, ψ ' and υ production at hadron colliders: A Review. *Int. J. Mod. Phys.*, A21:3857–3916, 2006.

[50] R. Baier and R. Ruckl. Hadronic Production of J/psi and Upsilon: Transverse Momentum Distributions. *Phys. Lett.*, B102:364, 1981.

[51] R. Baier and R. Ruckl. Hadronic Collisions: A Quarkonium Factory. *Z. Phys.*, C19:251, 1983.

[52] H. Haberzettl and J. P. Lansberg. Possible solution of the J/ψ production puzzle. *Phys. Rev. Lett.*, 100:032006, 2008.

[53] Stanley J. Brodsky and Jean-Philippe Lansberg. Heavy-Quarkonium Production in High Energy Proton-Proton Collisions at RHIC. *Phys. Rev.*, D81:051502, 2010.

[54] A. Adare et al. Transverse momentum dependence of J/psi polarization at midrapidity in p+p collisions at sqrt(s)=200 GeV. 2009.

[55] Eric Braaten and Sean Fleming. Color octet fragmentation and the psi-prime surplus at the Tevatron. *Phys. Rev. Lett.*, 74:3327–3330, 1995.

[56] A. D. Frawley, T. Ullrich, and R. Vogt. Heavy flavor in heavy-ion collisions at RHIC and RHIC II. *Phys. Rept.*, 462:125–175, 2008.

[57] Peter L. Cho and Adam K. Leibovich. Color octet quarkonia production. *Phys. Rev.*, D53:150–162, 1996.

[58] Peter L. Cho and Adam K. Leibovich. Color-octet quarkonia production II. *Phys. Rev.*, D53:6203–6217, 1996.

[59] Kari J. Eskola, Hannu Paukkunen, and Carlos A. Salgado. EPS09 - Nuclear PDFs and Their Uncertainties at NLO. *Nucl. Phys.*, A830:599c–602c, 2009.

[60] Xingbo Zhao and Ralf Rapp. Transverse momentum spectra of j/[psi] in heavy-ion collisions. *Physics Letters B*, 664(4-5):253–257, 2008.

[61] R. Vogt. The x(F) dependence of ψ and Drell-Yan production. *Phys. Rev.*, C61:035203, 2000.

[62] E. G. Ferreiro, F. Fleuret, J. P. Lansberg, and A. Rakotozafindrabe. Centrality, Rapidity and Transverse-Momentum Dependence of Cold Nuclear Matter Effects on J/Psi Production in d+Au, Cu+Cu and Au+Au Collisions at $sqrt(s_N N) = 200GeV$. *Phys. Rev.*, C81:064911, 2010.

[63] Cesar Luiz da Silva. Quarkonia measurement in p+p and d+Au collisions at sqrt(s)=200 GeV by PHENIX Detector. *Nucl. Phys.*, A830:227c–230c, 2009.

[64] NA38: `http://na38.web.cern.ch/NA38/`.

[65] NA50: `http://na50.web.cern.ch/NA50/`.

[66] NA51: `http://greybook.cern.ch/programmes/experiments/NA51.html`.

[67] NA60: `chttp://node6.ist.utl.pt/www`.

[68] Roberta Arnaldi. J/psi suppression in p-A and In In collisions. *J. Phys.*, G35:104133, 2008.

[69] Enrico Scomparin. J/psi production in p-A collisions at 158 and 400 GeV: recent results from the NA60 experiment. *Nucl. Phys.*, A830:239c–242c, 2009.

[70] A. Adare et al. Cold nuclear matter effects on j/psi as constrained by deuteron-gold measurements at sqrt(s) = 200 gev. *Phys. Rev.*, C77:024912, 2008.

[71] V. N. Tram. Measurements of J/psi yields at forward and mid-rapidity in d + Au, Cu + Cu and Au + Au collisions at s(NN)**(1/2) = 200-GeV by PHENIX at RHIC. 2006.

[72] Ermias T. Atomssa. J/psi Elliptic Flow, High pT Suppression and Upsilon Measurements in A+A Collisions by the PHENIX Experiment. *Nucl. Phys.*, A830:331c–334c, 2009.

[73] F. Prino and for the NA50 collaboration. J/psi azimuthal anisotropy relative to the reaction plane in Pb-Pb collisions at 158 GeV per nucleon. *Eur. Phys. J.*, C61:853, 2009.

[74] A. Adare et al. J/psi production in $\sqrt{s_{NN}}$= 200 gev cu+cu collisions. *Phys. Rev. Lett.*, 101:122301, 2008.

[75] A. Adare et al. J/psi production vs centrality, transverse momentum, and rapidity in Au + Au collisions at s(NN)**(1/2) = 200- GeV. *Phys. Rev. Lett.*, 98:232301, 2007.

[76] J. G. Alessi et al. The brookhaven national laboratory electron beam ion source for rhic. volume 81, page 02A509. AIP, 2010.

[77] M. Harrison, T. Ludlam, and S. Ozaki. Rhic project overview. *Nuclear Instruments and Methods in Physics Research Section A: Accelerators, Spectrometers, Detectors and Associated Equipment*, 499(2-3):235 – 244, 2003. The Relativistic Heavy Ion Collider Project: RHIC and its Detectors.

[78] K. H. Ackermann et al. Star detector overview. *Nuclear Instruments and Methods in Physics Research Section A: Accelerators, Spectrometers, Detectors and Associated Equipment*, 499(2-3):624 – 632, 2003. The Relativistic Heavy Ion Collider Project: RHIC and its Detectors.

[79] M. Anderson et al. The star time projection chamber: a unique tool for studying high multiplicity events at rhic. *Nuclear Instruments and Methods in Physics Research Section A: Accelerators, Spectrometers, Detectors and Associated Equipment*, 499(2-3):659 – 678, 2003. The Relativistic Heavy Ion Collider Project: RHIC and its Detectors.

[80] A. Rose. STAR integrated tracker. 2003.

[81] Pierre Billoir. Progressive track recognition with a kalman-like fitting procedure. *Computer Physics Communications*, 57(1-3):390 – 394, 1989.

[82] H. Bichsel. Energy loss in thin layers of argon, star note sn0418. Technical report, Mar. 20, 2000.

[83] H. Bichsel. Comparison of bethe-bloch and bichsel functions, star note sn0439. Technical report, Dec. 20, 2001.

[84] M. Beddo et al. The star barrel electromagnetic calorimeter. *Nuclear Instruments and Methods in Physics Research Section A: Accelerators, Spectrometers, Detectors and Associated Equipment*, 499(2-3):725 – 739, 2003. The Relativistic Heavy Ion Collider Project: RHIC and its Detectors.

[85] L. Arnold et al. The star silicon strip detector (ssd). *Nuclear Instruments and Methods in Physics Research Section A: Accelerators, Spectrometers, Detectors and Associated Equipment*, 499(2-3):652 – 658, 2003. The Relativistic Heavy Ion Collider Project: RHIC and its Detectors.

[86] L. Arnold et al. The star silicon strip detector (ssd). *Nuclear Instruments and Methods in Physics Research Section A: Accelerators, Spectrometers, Detectors and Associated Equipment*, 499(2-3):652 – 658, 2003. The Relativistic Heavy Ion Collider Project: RHIC and its Detectors.

[87] Jianhang Zhou. *Construction of a new detector, and calibration strategies, for start timing in the STAR experiment at RHIC*. PhD thesis, Rice University, 2007.

[88] F. S. Bieser et al. The star trigger. *Nuclear Instruments and Methods in Physics Research Section A: Accelerators, Spectrometers, Detectors and Associated Equipment*, 499(2-3):766 – 777, 2003. The Relativistic Heavy Ion Collider Project: RHIC and its Detectors.

[89] Mauro R. Cosentino. J/ψ production in pp collisions at $\sqrt{\mathrm{s}}$=200GeV in the STAR experiment. 2008.

[90] Anthony Timmins. *Neutral Strange Particle Production in Relativistic Cu+Cu Collisions at $\sqrt{s_{NN}}$ = 200 GeV*. PhD thesis, University of Birmingham, 2008.

[91] J. Adams et al (STAR Collaboration). Production of charged pions and hadrons in au+au collisions at $\sqrt{s_{NN}} = 130$ gev. *arXiv :nucl-ex/0311017v1*.

[92] B. I. Abelev et al. Systematic Measurements of Identified Particle Spectra in pp, d^+ Au and Au+Au Collisions from STAR. *Phys. Rev.*, C79:034909, 2009.

[93] Thomas A. Trainor and Duncan J. Prindle. A power-law description of collision centrality applied to Hijing-1.37-simulated Au - Au collisions at s(NN)**(1/2) = 200-GeV. 2004.

[94] R. L. Ray and M. Daugherity. Applicability of monte carlo glauber models to relativistic heavy ion collision data. *J. Phys.*, G35:125106, 2008.

[95] D. Kikola. `http://www.star.bnl.gov/protected/heavy/kikola/AuAuRun7_CentralitySelection/StabilityTest/StabilityCheck_ListOfHistFiles.html`.

[96] H. Masui. private communication and `http://www.star.bnl.gov/protected/lfspectra/hmasui/2008/centrality_AuAu_Run7`.

[97] P. Crochet and P. Braun-Munzinger. Investigation of background subtraction techniques for high mass dilepton physics. *Nucl. Instrum. Meth.*, A484:564–572, 2002.

[98] D. L'Hôte. About resonance signal extraction from multiparticle data: combinatorics and event mixing methods. *Nuclear Instruments and Methods in Physics Research Section A: Accelerators, Spectrometers, Detectors and Associated Equipment*, 337(2-3):544 – 556, 1994.

[99] Stephen Baumgart. *A Study of Open Charm Production in Heavy-Ion Collisions of Center of Mass Energy 200 GeV per Nucleon*. PhD thesis, Yale University, 2009.

[100] Xin Dong, Private communication.

[101] Yichun Xu et al. Calibration of ionization energy loss at relativistic rise with star time projection chamber, 2008.

[102] *GEANT - Detector Description and Simulation Tool, CERN Program Library Long Write-up W5013*, 1994.

[103] Hui Long. *Mid-rapidity Lambda and Lambda-bar Production in Au+Au Collisions at the Relativistic Heavy Ion Collider*. PhD thesis, University of California - Los Angeles, 2002.

[104] Torbjorn Sjostrand, Stephen Mrenna, and Peter Z. Skands. PYTHIA 6.4 Physics and Manual. *JHEP*, 05:026, 2006.

[105] A. Hoecker et al. *POSACAT*, 040, 2007.

[106] TMVA web page. `http://tmva.sourceforge.net`.

[107] ROOT web page: `http://root.cern.ch`.

[108] Michael P.S. Brown et al. Support vector machine classification of microarray gene expression data, 1999.

[109] Johan Gonzalez. *J/psi Production in Au+Au Collisions at sqrt(sNN) = 200 GeV*. PhD thesis, University of California - Los Angeles, 2006.

[110] A. Adare et al. J/ψ production versus transverse momentum and rapidity in p^+p collisions at $\sqrt{s}$ = 200-GeV. *Phys. Rev. Lett.*, 98:232002, 2007.

[111] Roger Barlow. Systematic errors: Facts and fictions. 2002.

[112] G. Lafferty. Where to stick your data points: The treatment of measurements within wide bins. *Nuclear Instruments and Methods in Physics Research Section A: Accelerators, Spectrometers, Detectors and Associated Equipment*, 355(2-3):541–547, February 1995.

[113] Yun-peng Liu, Zhen Qu, Nu Xu, and Peng-fei Zhuang. J/psi Transverse Momentum Distribution in High Energy Nuclear Collisions at RHIC. *Phys. Lett.*, B678:72–76, 2009.

[114] Xingbo Zhao and Ralf Rapp. Charmonium Production at High p_t at RHIC. 2008.

[115] Ramona Vogt, Private communication.

[116] A. Capella, L. Bravina, E. G. Ferreiro, A. B. Kaidalov, K. Tywoniuk, and E. Zabrodin. Charmonium dissociation and recombination at RHIC and LHC. *The European Physical Journal C*, 58(3):437–444, October 2008.

[117] Hao Qiu. Presentation at STAR Collaboration Meeting, LBNL, 2009.

[118] A. Poskanzer and S. Voloshin. Methods for analyzing anisotropic flow in relativistic nuclear collisions. *Physical Review C*, 58(3):1671–1678, September 1998.

[119] Shi Shusu. Private communication, 2009.

[120] STAR Bulk correlations working group mailing list: `http://www.star.bnl.gov/central/lists`.

[121] N. Borghini and J.-Y. Ollitrault. Azimuthally sensitive correlations in nucleus-nucleus collisions. *Phys. Rev. C*, 70(6):064905, Dec 2004.

[122] M. Calderon and others. Extending the physics reach of star: Prospects for the measurement of quarkonia. Technical report, 2003.

[123] B. I. Abelev et al. Upsilon cross section in p+p collisions at sqrt(s) = 200 GeV. 2010.

[124] STAR Time of Flight detector web page: `www.star.bnl.gov/public/tof/`.

[125] J Wu, M Xu, and STAR Collaboration. A barrel tof for star at rhic. *Journal of Physics G: Nuclear and Particle Physics*, 34(8):S729, 2007.

[126] L. Lima T. Ullrich. Presentation durion STAR Heavy Flavor working group meeting: `http://www.star.bnl.gov/HyperNews-star/protected/get/heavy/2471/1.html`.

[127] Xin-Nian Wang and Miklos Gyulassy. Hijing: A monte carlo model for multiple jet production in pp, pa, and aa collisions. *Phys. Rev. D*, 44(11):3501–3516, Dec 1991.